ABSTRACT

Title of Dissertation: CYLINDER-AIRFOIL INTERACTIONS AND THE EFFECT ON AIRFOIL PERFORMANCE

Jonathan Nathaniel Lefebvre
Doctor of Philosophy, 2021

Dissertation Directed by: Associate Professor Anya R. Jones
Department of Aerospace Engineering

From micro air vehicles flying in the wake of buildings to aircraft operating in ship airwakes, turbulent flows generate unsteady aerodynamic loads on airfoils that may promote structural failure, loss of flight control, and produce noise radiation. In order to develop engineering solutions capable of mitigating these effects, accurate force prediction of airfoils encountering turbulent wakes is necessary. A barrier to such force prediction techniques is the lack of a fundamental understanding of the aerodynamics of wake-airfoil interactions. The goal of this work is to investigate the cylinder-airfoil configuration by quantifying the effect of cylinder wake turbulence on airfoil force production and identifying the underlying flow physics. Results were obtained from both wind tunnel experiments and numerical simulations using a NASA OVERFLOW solver. Four cylinder-airfoil configuration parameters were evaluated: the gap (G/D) and offset (z/D) distances between the cylinder and airfoil, the cylinder-diameter-to-airfoil-chord ratio (D/c), and the cylinder cross-sectional geometry. During the investigation of each parameter, the airfoil angle of

attack varied from $\alpha = -5^\circ$ to 40° while the Reynolds number based on the airfoil chord c was fixed at $\mathrm{Re}_c = 1 \times 10^5$. Flow characterization of the region between the cylinder and airfoil revealed that the airfoil encounters a highly unsteady inflow. Turbulence intensity reaches 55 % of the freestream velocity upstream of the airfoil's leading edge while the flow oscillates at the cylinder vortex shedding frequency. The influence of the upstream cylinder wake on airfoil performance was quantified by time-averaged force measurements and showed three modifications compared to a clean inflow: (1) lift augmentation, (2) negative drag or thrust, and (3) delay in stall. The unsteady airfoil behavior was also investigated, showing that the amplitude of unsteady airloads increases for small gap and offset distances, while the airfoil frequency response matches the cylinder vortex shedding frequency. Flowfield measurements show that the cylinder-airfoil interaction induces flow separation at the leading edge of the airfoil, generating a leading edge vortex (LEV). The LEV is identified as the main flow structure responsible for modifying airfoil performance as it provides lift enhancement and delays stall at large angles of attack, while at low angles of attack the LEV promotes reverse flow at the surface, contributing to negative drag. The results and analysis from this work advance the fundamental flow physics of the cylinder-airfoil interactions by revealing key flow structures responsible for the unsteady force production on an airfoil in the wake of a cylinder.

CYLINDER-AIRFOIL INTERACTIONS AND THE EFFECT ON AIRFOIL PERFORMANCE

by

Jonathan Nathaniel Lefebvre

Dissertation submitted to the Faculty of the Graduate School of the
University of Maryland, College Park in partial fulfillment
of the requirements for the degree of
Doctor of Philosophy
2021

Advisory Committee:
Professor Anya Jones, Chair/Advisor
Professor James Baeder
Professor Pino Martin
Professor Norman Wereley
Professor James Duncan, Dean's Representative

Dedication

To Mom and Dad, your constant love and support made this thesis possible.

Acknowledgments

First and foremost, I would like to thank my advisor Dr. Anya Jones for her continuous support, encouragement, and patience during these past few years. It has been a wonderful experience to work besides Dr. Jones, everyday she pushed me to new heights while believing in my ability to succeed. Under her guidance, I learned the qualities necessary for a successful researcher, but I will never forget the respect and friendship she provides to each of her students.

I also want to thank my lab mates Hülya Biler, Luke Smith, Girguis Sedky, Oliver Wild, and Antonios Gementzopoulos for making my time at the University of Maryland both fun and memorable. This thesis was a blast to complete with such amazing friends. Thank you to Assaf Krupnik who helped me set up the wind tunnel for my experiments. A special thanks to Dr. Andrew Lind, who was my mentor when I first started in the lab as an undergrad. His passion for research, kindness, and friendship motivated me to pursue this degree.

This thesis would not be possible without my parents and their sacrifices for my education, and for that I am eternally grateful. Thank you to Dr. Marilyn Smith and Amanda Grubb for providing the CFD data for this thesis. Finally, thank you to the Office of Naval Research for funding my research. This work was supported under ONR award No. N00014-16-1-2731.

Table of Contents

List of Tables

List of Figures

Nomenclature

c	Airfoil chord
c_r	Vortex core radius
C_l	Lift coefficient
C_d	Drag coefficient
C_m	Pitching moment coefficient
D	Cylinder diameter
E	Enstrophy
f	Frequency
G/D	Gap distance
k	Reduced frequency, $k = \frac{\pi f c}{U_\infty}$
k_0	wavenumber
Re_c	Reynolds number based on the airfoil chord, $\mathrm{Re}_c = \frac{\rho U_\infty c}{\mu}$
Re_D	Reynolds number based on the cylinder diameter, $\mathrm{Re}_D = \frac{\rho U_\infty D}{\mu}$
St_D	Strouhal number based on the cylinder diameter, $\mathrm{St}_D = \frac{fD}{U_\infty}$
u	Instantaneous velocity
U_∞	Freestream velocity
$\overline{u}$	Time-averaged velocity
$\tilde{u}$	Phased-averaged velocity
u'	Fluctuating velocity
$\mathcal{W}$	Kinematic vorticity number
z/D	Offset distance

Greek Symbols

α	Angle of attack
α_{eff}	Effective angle of attack
α_{wake}	Wake flow angle of attack
Γ	Vortex circulation
ϵ	Turbulence kinetic energy dissipation rate
η	Kolmogorov length scale
Λ	Integral length scale
μ	Fluid dynamic viscosity

ρ Fluid density
ω Vorticity

List of Abbreviations

CTA Constant temperature anemometer
FOV Field of view
LEV Leading edge vortex
PIV Particle image velocimetry

Chapter 1: Introduction

1.1 Motivation

Historically, aircraft design required the study of airfoil performance in low freestream turbulence [1] and there exists an abundance of data summarizing the aerodynamic forces on airfoils [2]. It is a misconception to suppose that airfoils do not operate in moderate to high turbulent flows, yet a noticeable lack of research is present [3]. Only more recently has the fluid dynamics community focused on airfoils operating in turbulent wakes since engineering applications frequently encounter turbulence. Some examples of these applications include the operation of micro air vehicles in an urban environment where wakes are created by buildings [4, 5], tandem wings for the wing-tail configuration of an aircraft [6, 7], wake interaction during formation flight [8,9], aircraft maneuvering in ship airwakes generated by the ship body and superstructure [10–13], rotorcraft blade-vortex interactions [14–16], and wake effects on downstream turbines in wind turbine farms [17–19]. In all of these instances, the upstream body creates an unsteady wake that interacts with a downstream aerodynamic surface, affecting the aerodynamic behavior [4–19].

Although wake-airfoil interactions occur in vastly different applications, the unsteady wake encountering the airfoil shares common flow features regardless of

the configuration. An unsteady wake produces strong velocity perturbations characterized by sudden spatial and temporal changes in the velocity magnitude and direction. These flow characteristics appear in velocity shears, coherent structures such as vortices, large regions of separated flow, and turbulence. Therefore, the interaction between an upstream turbulent wake and a downstream body produces unsteady aerodynamics. If left unchecked, unsteady loads that arise from this interaction can have nefarious consequences such as compromised structural integrity due to fatigue [10, 14], loss of flight control during critical maneuvers [20, 21], or increased noise radiation [22, 23]. Accurate knowledge of the transient loads on a lifting body, such as an airfoil, is necessary to develop engineering solutions able to contend with the effects of wake interactions.

Theoretical models developed using classical unsteady aerodynamics provide analytical functions for calculating transient airloads during wake-airfoil interactions. For example, Küssner's function provides an airfoil's response when encountering a sharp-edged transverse gust [24], while models developed by Sears and Atassi consider harmonic gusts [25–28]. Despite the elegance of these classical models, in many cases the assumptions made by these models do not remain valid during strong wake interactions. Predicting unsteady forces in relatively strong wakes is non-trivial, and wake flow features are not easily modeled. Therefore, this study is concerned with understanding the underlying flow physics associated with wake-airfoil interactions to advance our current knowledge of this complex flow in order to improve force prediction techniques.

1.2 Problem Statement

In most engineering applications, the interaction of a lifting surface with incoming wake turbulence is a highly unsteady, three-dimensional flow dependent on numerous parameters. An excellent example of this flow interaction occurs when naval aircraft operate in a ship airwake as illustrated in figure 1.1. The wake flow relates to the ship geometry with the superstructure producing a large region of flow separation, characterized by large vortices, while auxiliary structures (e.g. smokestack, antennae, etc.) populate the airwake with smaller vortices. In addition, the dynamic nature of the wind-sea interface and ship motions [29] contribute to the unsteady behavior of the ship airwake. Since critical aircraft flight maneuvers (e.g. takeoff, landing, approach, and hover) occur over the flight deck located downstream of the superstructure, wake flow features generated by this bluff body dominate during the wake-airfoil interaction.

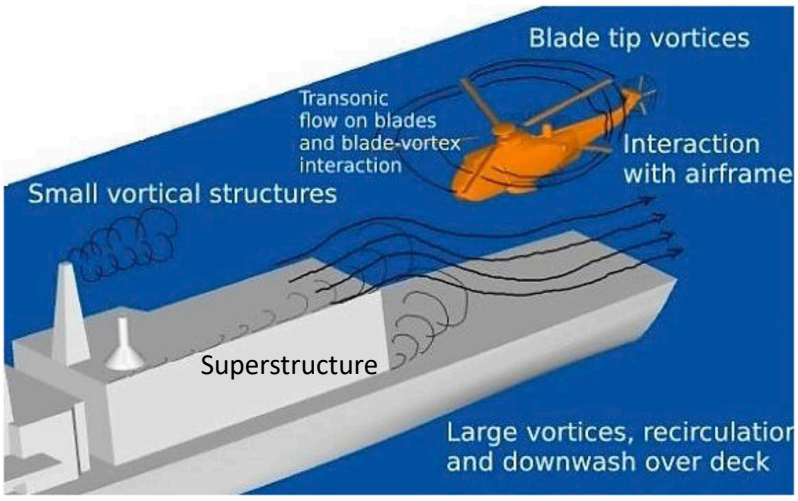

Figure 1.1: Illustration of key flow features from a ship airwake-helicopter interaction. Adapted from Shukla et al. [10].

The geometric arrangement between the superstructure and flight deck forms a backward-facing step, resulting in a turbulent wake due to flow separation. Wang et al. [30] identified key flow features arising from a backward-facing step using time-resolved particle image velocimetry (PIV) shown in figure 1.2, illustrating the ship airwake over a flight deck. Flow separates from the superstructure forming a free shear layer that delineates the freestream outer flow and the low momentum wake flow. Downstream of the superstructure, a Kelvin-Helmholtz instability in the free shear layer leads to the formation and shedding of large coherent structures, represented by the spiraling streamlines. Thus during critical flight maneuvers over the flight deck, naval aircraft are subjected to parallel vortex interactions due to the superstructure's bluff body wake.

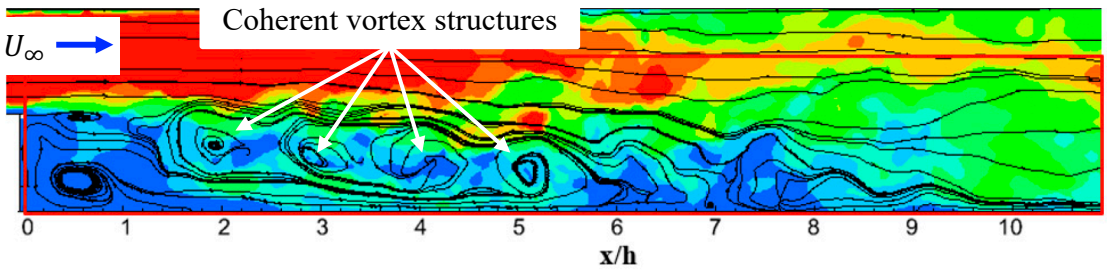

Figure 1.2: Instantaneous velocity countours and streamlines for a backward-facing step flow. Adapted from Wang et al. [30].

Since the current work aims to elucidate the underlying flow physics of wake-airfoil interactions and the effect on airfoil force production, a simplified configuration is employed using two test models: a periodic, turbulent wake generator and an airfoil. An additional simplification is to restrict the study to two-dimensional flow and this is justified as the two-dimensional wake-airfoil interaction is not yet

fully understood. Finally, the geometries in this study will be limited to canonical shapes making the cylinder-airfoil configuration ideal for this study.

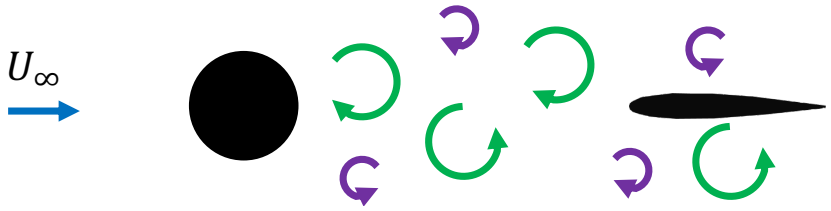

Figure 1.3: Sketch of the cylinder-airfoil configuration.

Figure 1.3 displays a sketch of the cylinder-airfoil configuration with a circular cylinder acting as the wake turbulence generator upstream of a NACA 0012 airfoil. The cylinder is an ideal wake generator as it produces both large and small vortical flow structures. The NACA 0012 airfoil is ubiquitous in the fluid dynamics community, thus provides a reliable benchmark to compare airfoil performance. With this configuration, the present work aims to address gaps in the literature about wake-airfoil interactions by answering the following questions:

1. How do wake-airfoil interactions alter airfoil force production?

2. Which flow features arising from the cylinder-airfoil wake flow are responsible for these changes?

With these questions answered, this thesis will have advanced the current understanding of wake-airfoil interactions at a fundamental level.

1.3 Dissertation Outline

A review of previous work and research objectives for this thesis are introduced in chapter 2. Chapter 3 describes the experimental and numerical methods used in the present work. A complete flow characterization of the unsteady flow found in the wake of the cylinder and upstream of the airfoil is given in chapter 4. Chapter 5 details the parametric study conducted to determine the influence of a turbulent wake on the aerodynamic airfoil response for four cylinder-airfoil parameters. The time-averaged lift, drag, and pitching moment coefficients are presented along with the amplitude and frequency of airload fluctuations. Chapter 6 relates the airfoil performance to flow structures formed from the cylinder-airfoil interaction, and investigates the accuracy of existing low order models at predicting the unsteady loads. Chapter 7 summarizes the present work, lists the main contributions and key conclusions before providing suggestions for future work.

Chapter 2: Background and Research Objectives

The following sections will provide an overview of the existing literature pertaining to the effect of unsteady inflow conditions on airfoil performance.

2.1 Cylinder Wakes

As the present work is concerned with a cylinder's turbulent wake interacting with a downstream airfoil, it is crucial to first understand wake flow features of an isolated cylinder. Although the circular cylinder is a simple geometry, the resulting wake is complex, motivating numerous recent studies [31–33]. This section will summarize key wake flow features that are relevant for understanding the cylinder-airfoil configuration. The Reynolds number describes the ratio of inertial-to-viscous effects. Here it is defined based on the cylinder diameter by $\mathrm{Re}_D = \rho U_\infty D/\mu$, where ρ, U_∞, D, and μ correspond to the fluid density, the freestream velocity, the cylinder diameter, and the fluid dynamic viscosity, respectively.

For $\mathrm{Re}_D > 40$, the cylinder wake is characterized by periodic shedding of vortices forming the well-known von Kármán vortex street [34]. The formation of this wake structure arises as flow separates from the cylinder's surface, creating two shear layers that roll-up into the coherent vortex structures [34]. This periodic

phenomenon has a well characterized frequency f, often reported as the normalized frequency defined by the Strouhal number $\mathrm{St} = fD/U_\infty$. For sufficiently large Reynolds number ($\mathrm{Re}_D > 300$), the Strouhal number is nearly constant with values ranging from $\mathrm{St} = 0.18$ to 0.21 [34–36]. This produces a wake that oscillates at this vortex shedding frequency and results in large flow angles up to approximately 45° [37].

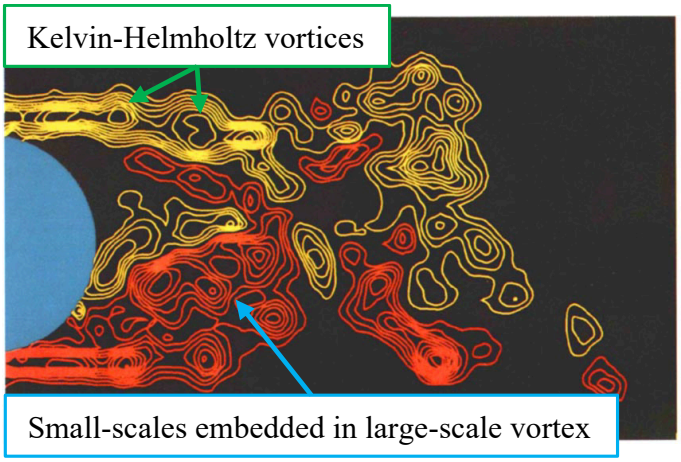

Figure 2.1: Instantaneous vorticity contours of a cylinder near wake at $\mathrm{Re}_D = 1 \times 10^4$. Adapted from Lin et al. [38].

The unsteadiness of the cylinder wake is also characterized by various turbulence scales. For Reynolds number $\mathrm{Re}_D > 1 \times 10^3$, flow in the cylinder's shear layers undergo a Kelvin-Helmholtz instability creating smaller coherent structures in the wake [39]. In addition, flow transitions from a laminar to turbulent state in these shear layers [34]. Instantaneous vorticity contours from Lin et al. [38] in figure 2.1 show small-scale vortices in the cylinder shear layer due to the Kelvin-Helmholtz instability as these small structures amalgamate into a large vortex before shedding. From this process, the cylinder wake contains a wide range of turbulence scales. In

the near wake, less than five cylinder diameters downstream, large velocity fluctuations accompany these turbulence scales in both streamwise and transverse directions as the turbulence intensity can exceed 40 % of the freestream velocity [37, 40]. Finally, the cylinder wake is also characterized by a velocity deficit dependent on the streamwise and transverse distance from the cylinder. This decrease in velocity is maximum along the centerline, and at two cylinder diameters downstream the velocity deficit is greater than 50 % of the freestream value [37, 40]. Increasing the downstream distance and moving away from the centerline, Ong and Wallace [40] and Cantwell and Coles [37] showed that the velocity quickly relaxes to freestream conditions.

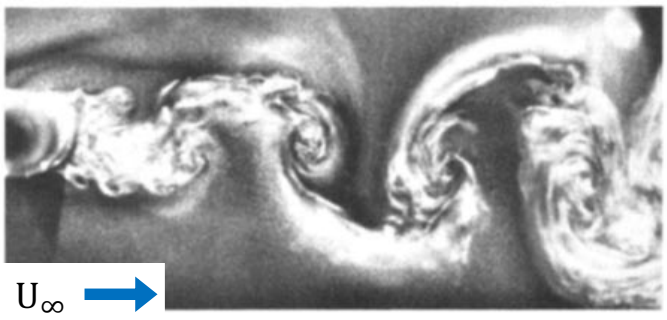

Figure 2.2: Flow visualization of a turbulent von Kármán vortex street at $\mathrm{Re}_D = 4 \times 10^4$. Adapted from Williamson [32].

The studies mentioned above reveal that the cylinder's wake is highly unsteady and turbulent. Large coherent vortex structures superimposed with small turbulence scales define the periodic velocity perturbations found in the near wake of a cylinder. Figure 2.2 illustrates this superposition of flow scales as the turbulent von Kármán vortex street exhibits large coherent vortices affected by small-scale turbulence. Therefore, the cylinder generates a turbulent wake which is ideal for

studying wake-airfoil interactions.

2.2 Influence of Freestream Turbulence on Airfoil Performance

Since the cylinder's wake is characterized by a combination of different turbulence scales, this section will first provide an overview of the influence of freestream turbulence on airfoil performance. Most studies on airfoil performance were conducted in low turbulence flows, and as a consequence less is known about the effects of a turbulent flow [3, 41, 42]. Generally, wind tunnel facilities guarantee low turbulence freestream in the test section and turbulence is commonly introduced by means of passive grids [43]. The turbulence intensity and integral length scale are two parameters describing the state of freestream turbulence. The former quantifies the level of velocity fluctuations with respect to the freestream velocity, while the second indicates the scale of energy containing eddies. Variations in turbulence intensity are prevalent and can range from 1 % to 16 % [3, 41, 42, 44–46], but changes in the integral length scale are less common and most authors simply report this value [41, 42, 44].

The influence of freestream turbulence on airfoil performance has been reported for Reynolds number, based on the airfoil chord c, ranging from $\mathrm{Re}_c = 5 \times 10^4$ to 1×10^6 and various airfoil geometries (e.g. NACA 0012, NACA 4412) [3, 41, 42, 44–46], although changes in airfoil performance share common trends. In the presence of a turbulent inflow, the airfoil's maximum lift coefficient is increased and stall is delayed to higher angles of attack [3, 41, 42, 44–46]. Depending on the

Reynolds number, turbulence intensity, and airfoil, this increase can be significant as Hoffmann [3] noted a 30 % rise in the maximum lift coefficient for a turbulence intensity of 9 %. Stall angle can be delayed by more than 10° [41, 45]. These modifications in airfoil performance are further enhanced as the level of turbulence intensity increases [3, 41, 42, 44–46].

For an inflow with low turbulence, airfoil performance at low angles of attack is defined by a linear region for the lift coefficient with a slope of approximately 2π. However, freestream turbulence greater than 4 % reduces the lift curve slope and this reduction amplifies with increasing turbulence levels [41, 44]. Typically, this effect is notable at low Reynolds number ($\mathrm{Re}_c < 2.5 \times 10^5$), yet Devinant et al. [45] observed this trend at $\mathrm{Re}_c = 4 \times 10^5$ with a turbulence intensity of 16 %. Kay et al. [44] showed that a large turbulence intensity of 16 % reduces the lift curve slope more for a cambered airfoil. The implications of a decline in the lift curve slope at low angles of attack are significant for airfoil performance. At low angles of attack, an airfoil operating in freestream turbulence produces less lift compared to an identical airfoil in a smooth flow. However, as the angle of attack increases, freestream turbulence delays stall and increases the maximum lift coefficient, improving airfoil performance. Depending on the angle of attack, airfoil performance can either be degraded or enhanced due to the influence of freestream turbulence.

In addition to changes in the maximum lift coefficient, Swalwell [42] and Devinant et al. [45] observed a modification in the airfoil stall behavior for turbulence intensity as low as 4 %. Instead of lift decreasing abruptly after stall, the effect of flow turbulence provides a gradual decrease in the lift coefficient. This change

in stall behavior relates to the location of the separation point on the airfoil's surface. Results from references [45, 46] show that increasing the turbulence intensity moves the separation point closer to the trailing edge compared to low turbulence conditions. Increasing the angle of attack moves this separation point smoothly towards the leading edge of the airfoil, unlike the sudden jump for low turbulence flows [45, 46]. The separation point moves aft in the presence of freestream turbulence, decreasing the size of the airfoil's wake. This results in a reduction of the drag coefficient [42, 45].

The effects of freestream turbulence on airfoil performance are considerable when the turbulence intensity is greater than 4 %, but few studies reveal the underlying flow physics. Flow visualization from Hoffmann [3] and Ravi et al. [41] show that a laminar separation bubble (LSB) manifests near the airfoil leading edge for low turbulence cases. Increasing the freestream turbulence modifies the flowfield as the shear layer can roll-up into a leading edge vortex (LEV) replacing the LSB [41]. The change in airfoil performance is therefore related to the change in the flowfield surrounding the airfoil. In order to delay stall, the adverse pressure gradient on the airfoil must be mitigated, yet few studies provide a detailed explanation of how freestream turbulence achieves this.

Devinant et al. [45] explains that since a turbulent flow enhances mixing, the freestream turbulence interacts with the airfoil's boundary layer. This transfers turbulent kinetic energy to the boundary layer while the flow over the airfoil transitions from a laminar to a turbulent state [45]. It is well known that a turbulent boundary layer better resists the adverse pressure gradient and hence provides resistance to

stall. As a consequence, airfoil stall is delayed and lift can increase to larger maximum values. A turbulent boundary layer is also thicker, causing a displacement effect around the airfoil which is responsible for decreasing the lift curve slope at low angles of attack [45].

Previous studies show that sufficiently large freestream turbulence ($\geq 4\,\%$) influences airfoil performance. At low angles of attack lift is reduced, but at larger incidence angles the freestream turbulence promotes lift enhancement, drag reduction, and stall delay. These changes are due to modifications in the flowfield, especially in the boundary layer.

2.3 Vortex-Body Interactions

Coherent vortex structures characterize the cylinder wake (see figure 2.2), thus it is important to review the influence of vortex-body interactions. Rockwell's review of vortex-body interactions [47] states any vortex-dominated flow that encounters a downstream body will induce transient loads. These interactions are dependent on the incident vortex scale, with the largest response occurring when vortices are similar in size to the length of the body [47, 48]. If the perturbation vortex is substantially larger than the body, the flow is assumed to be quasi-steady. For small vortex perturbations, the flowfield remains mostly undisturbed and the unsteady influence on the body can be neglected. For an appropriately sized vortex encountering a downstream body, several vortex parameters dictate the unsteady response including the vortex strength, the offset distance relative to the leading edge, vor-

tex rotation, and wavelength if the vortex is part of a von Kármán street [47–50]. A brief presentation of past studies will reveal the impact of these parameters on unsteady loading during a vortex-body interaction.

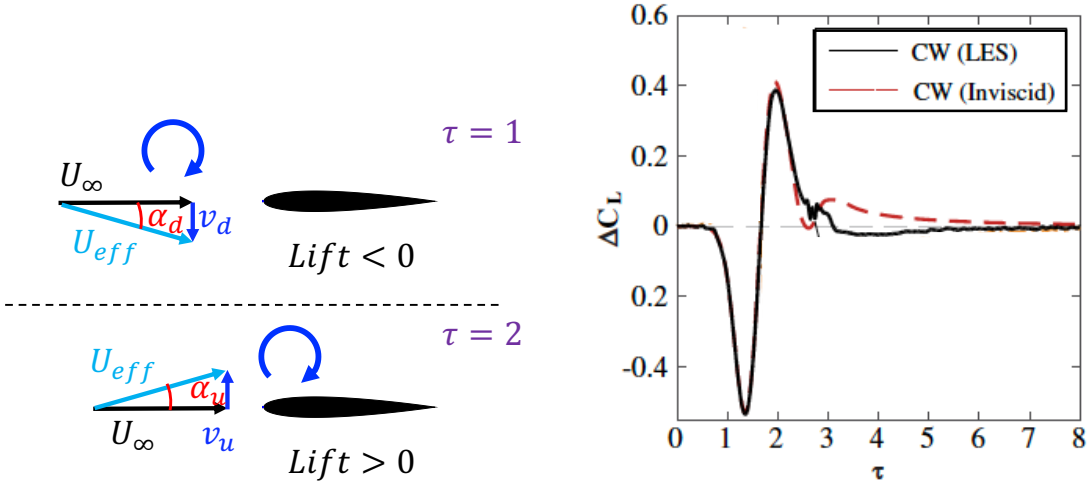

(a) Sketch of blade-vortex interaction

(b) Lift response due to vortex

Figure 2.3: Lift perturbation due to blade vortex interaction. (b) Adapted from Barnes and Visbal [51].

Assume a symmetric airfoil (e.g. NACA 0012) at zero angle of attack in a constant freestream, no net lift is produced. Adding a clockwise rotating vortex upstream of the airfoil convecting with the freestream velocity induces transient loads on the airfoil in a manner similar to blade-vortex interactions [15, 49]. As the vortex approaches the leading edge of the airfoil, shown in the top of figure 2.3(a), it generates a downwash v_d due to the clockwise flow rotation. This creates a negative effective angle of attack α_d, resulting in negative lift [15, 49]. The opposite effect occurs when the vortex core passes the airfoil leading edge as the upstream side of the incident vortex produces an upwash v_u as shown in the bottom of figure

2.3(a). This induces a positive effective angle of attack α_u, generating positive lift. As the vortex encounters the airfoil, it produces an unsteady lift response shown in figure 2.3(b): the blade-vortex interaction first causes a negative lift peak at $\tau = 1.4$ before switching to a positive lift peak at $\tau = 2$. The converse is true if the rotation of the incident vortex is counterclockwise. Varying the circulation of the vortex affects the amplitude of unsteady loading on the body [48, 49, 52] due to the change in induced velocities. A stronger vortex will increase the upwash and downwash velocities encountered by the airfoil, enhancing the vortex-body interaction. The interaction between a vortex and airfoil provokes a time-varying inflow that manifests as unsteady aerodynamic loads on the airfoil.

The offset distance between the vortex trajectory and body also dictates the amplitude of the unsteady body response. For large offset distances, the vortex-blade interaction diminishes, decreasing the transient aerodynamic response of the airfoil [49, 52]. This behavior is expected as the induced velocity of the vortex decreases with distance, resulting in smaller upwash and downwash velocities. Hence, the offset distance is an important parameter as the unsteady body response in a vortex-body interaction is inversely proportional to the transverse vortex distance.

However, Peng and Gregory [49] showed that zero offset distance does not correspond to the maximum amplitude of the fluctuating loads. For a symmetric airfoil at zero incidence angle, different local velocities are induced at the leading edge depending on the offset distance [49]. Assuming a clockwise rotating vortex is below the airfoil (negative offset distance), the top half of the vortex contributes in the streamwise direction and increases the velocity at the leading edge. The converse

is true when the clockwise vortex is above the airfoil (positive offset distance) and reduces the velocity at the leading edge. According to Peng and Gregory [49] the suction peak at the leading edge is responsible for the majority of pressure fluctuations and by extension the load fluctuations. Therefore, a clockwise vortex induces maximum amplitude in the unsteady body response not for zero offset, but for a small negative offset distance.

Flow visualization of a vortex-body interaction reveals intricate flow structures. Depending on the flow angle produced by the vortex upwash (or downwash), the leading edge geometry of the body, and the angle of attack of the body, the vortex-body interaction can initiate the eruption of the body boundary layer [47, 50, 53, 54]. Due to this vortex-induced flow separation, secondary vortex structures, e.g. a leading edge vortex (LEV), form near the leading edge of the body [50,54,55]. As a property of this interaction, the LEV formed is of the opposite rotation from the incident vortex. The LEV is also responsible for pressure fluctuations along the surface and as the LEV convects with the freestream flow, a pressure wave propagates along the body [15,50]. This inherently amplifies unsteady loading on the body compared to a vortex-body interaction where no secondary structure forms, and illustrates that unsteady forces can be related to flow structures.

The incident vortex not only induces flow separation, but also interacts with the boundary layer. These effects are more pronounced at large Reynolds number such as Barnes and Visbal [54] show for numerical simulations of a NACA 0012 pitched at $\alpha = 4^\circ$ when encountering a counterclockwise vortex at $\mathrm{Re}_c = 2 \times 10^5$. Time histories of aerodynamic load perturbations due to the approaching vortex

show expected trends for the lift coefficient due to the induced upwash and downwash. However, the authors report a strong negative drag (thrust) peak without providing an explanation for the flow physics. Barnes and Visbal [54] instead focus on the unsteady response due to the interaction between the vortex and the airfoil's boundary layer. Due to the non-zero pitch angle, the boundary layer behaves differently on the upper and lower surfaces. On the upper surface, a LSB develops briefly before bursting into a LEV and convects towards the trailing edge. This LEV provides a downwash on the upper surface and causes the boundary layer to relaminarize before two-dimensional instability waves transitions the flow to a turbulent state [54]. These unsteady events contribute to large fluctuations in the pitching moment long after the vortex has left the airfoil [54]. The lower surface boundary layer remains laminar throughout most of this interaction, although it thickens before developing two-dimensional instabilities. This illustrates the complexity involved in the vortex-body interaction even as the general trend can be described by the inflow conditions.

Up to this point, review of the vortex-body interaction focused solely on an isolated vortex encountering a body. However, when this interaction occurs periodically, such as from a von Kármán vortex street, the unsteady body loading is no longer locally transient but periodic [56, 57]. Similar to isolated vortex interactions, the offset distance plays an important role in the unsteady pressure amplitude with small offsets producing a larger pressure response [56, 57]. In addition, the pressure response is now also dependent on the wavelength of the incoming vortices, with a large wavelength increasing the magnitude of unsteady pressure along the body's

surface [56, 57]. In the case of a von Kármán vortex street encountering a body, Gursul and Rockwell [56] measured one dominant frequency in the unsteady pressure measurements corresponding to the von Kármán vortex street frequency. This shows that unsteady body loading relates to the unsteady inflow.

As reference [54] showed, the state of the boundary layer influences the body loading during an isolated vortex interaction, and the same applies for a periodic vortex street. Results from Gursul and Rockwell [56] were obtained at a maximum Reynolds number of 619 which did not cause flow separation from the incident vortices, thus pressure fluctuations are simply due to the traversing of these vortices. In contrast, Kaykayoglu and Rockwell [57] used a body with a sharp leading edge to promote flow separation at low Reynolds number (Re = 230) and observed the periodic formation of secondary vortex structures (LEVs) near the leading edge. Results from their study indicated that the magnitude of pressure fluctuations was maximum near the leading edge and the LEVs generated a large negative pressure region at the body's surface [57]. Unlike the non-separated flow encounter, the secondary vortex produced a traveling low pressure wave with decreasing amplitude along the body's surface. Past studies on vortex-body interactions show this unsteady body response depends on the inflow conditions and the resulting flowfields. However, these studies consider the wake either as a single vortex or a vortex street, while the turbulent nature of wakes is often ignored.

2.4 Wake-Body Interactions

It was shown in the previous sections that a cylinder's wake is composed of large coherent structures superimposed with small turbulence scales. As both coherent vortices and turbulence encounter a downstream body, they create flow disturbances which determine the aerodynamic loading on this body. Therefore, it is expected that the turbulent wake behind a cylinder will also alter the pressure distribution on a downstream body. The following presents key flow features affecting force production during a wake-body interaction.

2.4.1 Tandem Cylinders Configuration

Two parallel, circular cylinders in a cross flow is the simplest geometric setup and the most common flow configuration when studying wake-body interactions. Zdravkovich [58] provides an excellent review of this configuration and identifies three key interference regimes: (1) wake interference occurs when two cylinders are in tandem, (2) proximity interference exists when the cylinders are in a side-by-side arrangement, and (3) wake-proximity interference manifests for staggered cylinders. These three configurations are illustrated in figure 2.4. As the current study focuses on wake-body interaction, only the wake interaction from tandem cylinders is discussed here.

As Zdravkovich [59] describes, wake interference for tandem cylinders occurs when the downstream cylinder is submerged in the wake of the upstream cylinder. The effect of a tandem configuration on cylinders is to dramatically alter the wake

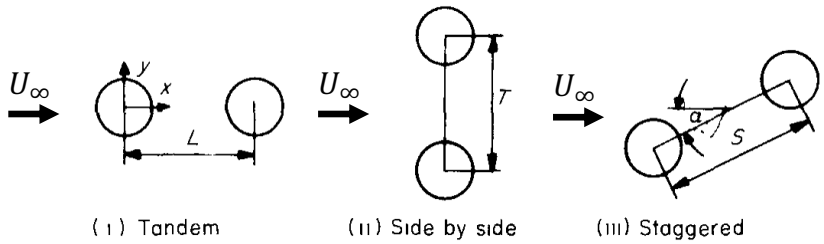

Figure 2.4: Classification of cylinder-cylinder configurations. Adapted from Zdravkovich [59].

regime depending on the gap distance between bodies because the von Kármán street vortex on the upstream cylinder is suppressed for small inter-cylinder distances [58, 59]. Shear layers separating from the upstream cylinder are prevented from rolling-up into the coherent structures that form the well known periodic vortex wake due to the close proximity of the downstream cylinder. This vortex suppression in the inter-cylinder region is typically observed at a critical gap distance less than three diameters. When this gap distance increases to five diameters, both cylinders produce synchronized vortex street wakes due to a coupled shedding mechanism [60]. Beyond a distance of six diameters, the upstream and downstream cylinders become uncoupled as each body sheds its own periodic vortex wake, albeit at two different shedding frequencies [61]. Tandem cylinders offer insight into the influence of wake interactions with a body. This can be strong enough to suppress a cylinder vortex wake or weak, altering only the vortex shedding frequencies. In all cases, however, there is a modification in the wake behavior.

In wake-body interactions, the unsteady nature of a wake critically determines the transient loads on the downstream body. For tandem cylinders where the inter-

cylinder distance modifies the wake structure, it is expected that the drag coefficient for both cylinders will differ from that of an isolated cylinder. Below a critical gap distance of three diameters, and without vortex shedding from the upstream cylinder, the upstream cylinder experiences a drag reduction while the downstream cylinder undergoes a change in drag direction, resulting in thrust [58]. For this configuration, the spacing between tandem cylinders is responsible for altering the pressure distribution across each body [62].

2.4.2 Cylinder-Airfoil Configuration

To understand the influence of wake turbulence on airfoil performance, the cylinder-airfoil configuration must now be reviewed. The cylinder-airfoil configuration shares some similarities with the tandem cylinders configuration, although notable differences exist. Most studies involving the cylinder-airfoil configuration focus on investigating the noise radiation from the cylinder's turbulent wake impinging on a downstream airfoil [63–67]. As a consequence, Jacob et al. [63] and Boudet et al. [64] only characterize the flow between the cylinder and airfoil. Their results highlight a turbulent inflow to the airfoil with a streamwise turbulence intensity of approximately 17.4 % of the freestream velocity.

The cylinder wake in the cylinder-airfoil configuration is also contingent on the gap distance between both bodies. Similar to tandem cylinders, a critical gap distance exists that dictates flow structures in the cylinder-airfoil wake, and Munekata et al. [65] and Jiang et al. [67] identified this critical gap distance as three

cylinder diameters. Below this critical gap distance, the proximity of the airfoil suppresses the cylinder's von Kármán vortex street by inhibiting the shear layer roll-up [65, 67]. Above this critical gap distance, the cylinder's wake fluctuates at an expected Strouhal number of St = 0.20 [63, 64]. Muketa et al. [65, 66] suggest that the frequency of the sound pressure level corresponds to the unsteady pressure along the airfoil's surface, and Jiang et al. [67] substantiate this claim by investigating the airfoil's lift spectrum. These results show that the airfoil's unsteady loading fluctuates at the cylinder's vortex shedding frequency. For an isolated cylinder, the vortex shedding frequency is typically a constant, but Munekata et al. [66] showed that variations in the airfoil's angle of attack affects the cylinder vortex shedding, modifying the airfoil's frequency response. As the angle of attack increases, the airfoil produces a larger blockage effect resulting in an increase of the pressure on the downstream side of the cylinder. Flow visualizations show an increase in the shed vortex size, explaining the decrease in vortex shedding frequency [66]. These aeroacoustic studies [63–67] provide an assessment of the airfoil's frequency response in the cylinder-airfoil configuration and determine that the cylinder vortex shedding frequency influences the fluctuating pressure distribution. Unfortunately, these studies do not investigate the effect of wake turbulence on the airfoil force amplitude and stall behavior, limiting the knowledge of airfoil force production during cylinder-airfoil interactions.

In the cylinder-airfoil configuration, the downstream airfoil encounters a turbulent inflow generated by the upstream cylinder's wake, causing the lift coefficient to reduce [68, 69]. This effect is strongest when the center of the wake impinges with

the leading edge of the airfoil [68]. This lift reduction persists for increasing angle of attack and this results in a decrease of the lift curve slope compared to an isolated airfoil [69–71]. Lift measurements by Durgesh et al. [71] in figure 2.5 compare the variation in lift coefficient for an isolated NACA 0012 (left side) with the airfoil lift when downstream of a cylinder (right side). The dashed line represents the theoretical lift solution ($C_l = 2\pi\alpha$), and the isolated airfoil closely follows this trend, while in the cylinder-airfoil configuration the lift curve slope is decreased. Similar to the influence of freestream turbulence, this shallower lift curve slope is accompanied by an increase in the maximum lift coefficient and in the stall angle [69–71]. To illustrate this, Chen and Choa [69] reported the $C_{l,max}$ of a NACA 0012 increased from 0.90 to 1.05 while stall was delayed from $\alpha = 10°$ to 14°. In most cylinder-airfoil studies, the turbulent wake is generated by a small cylinder ranging from 3.3 % to 16 % of the airfoil chord and the tested gap distance varies from 10 to 30 cylinder diameters [63–67, 69, 71]. Since the largest coherent structures are significantly smaller than the airfoil chord and a wide gap distance enables turbulence to fully develop, the cylinder wake effectively acts as freestream turbulence. This explains why the cylinder-airfoil trends for small cylinders and large gap distances agree with the results of freestream turbulence encountering an airfoil.

The reduction in the lift curve slope, increase in maximum lift, and stall delay continue to occur even as the characteristic length of the upstream body reaches half of the airfoil chord with a gap distance of three cylinder diameters [70, 71]. In the following references [69–71], a velocity deficit ranging from 20 % to 37 % exists upstream of the airfoil. Michelsen and Mueller [68] argue that the airfoil encounters

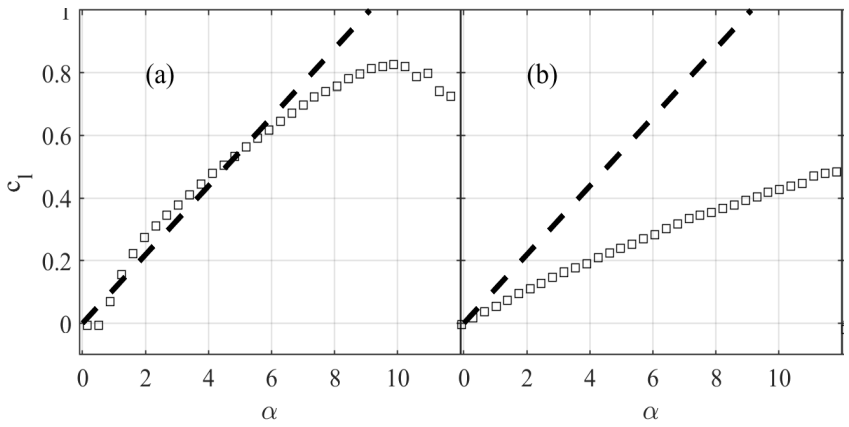

Figure 2.5: Lift coefficient versus angle of attack for an (a) isolated NACA 0012 airfoil and (b) a NACA 0012 downstream of a cylinder. The dashed black line respresents $C_l = 2\pi\alpha$. Adapted from Durgesh et al. [71].

a lower freestream due to the incoming wake and this is responsible for decreasing the lift coefficient at low angles of attack. This artificial decrease occurs since the force normalization uses the undisturbed freestream velocity as the reference velocity instead of using the local wake velocity upstream of the airfoil's leading edge [68]. Durgesh et al. [71] apply this correction to their lift measurements and notice that the corrected lift coefficient follows the theorectical value of $2\pi\alpha$ in the linear region. This indicates that the wake velocity, and by extension the gap distance between bodies, is also a factor in airfoil performance for the cylinder-airfoil configuration.

Zhang et al. [70] identify flow features that enhance lift. Due the periodic wake interacting with the airfoil, flow separation occurs at the leading edge when the airfoil's angle of attack is $\alpha \geq 15°$. This causes the formation of a LEV that is responsible for increasing the maximum lift coefficient while also delaying stall [70]. The influence of lift enhancement on airfoil performance is not maximum at the centerline, but rather at an offset distance. Placing the airfoil at a distance of 70 %

of the chord below the wake centerline increases the maximum lift coefficient by 34 % as the offset wake continues to induce flow separation with less interference on the LEV growth [70]. This offset distance also reduces the amplitude of lift fluctuations as less turbulent kinetic energy resides in the transverse locations of the wake [70, 72].

The presentation of wake-body interactions clearly shows that airfoil force production and the airfoil unsteady behavior are strongly influenced by the incoming wake. However most of these studies focus on the gap or offset distance of the cylinder-airfoil configuration while drag and pitching moment are often neglected.

2.5 Analytical Models

The previous section detailed key force trends and flow features of the cylinder-airfoil configuration, yet understanding the underlying flow physics remains a challenge. Even without a complete knowledge of wake-airfoil interactions, these previous studies reveal that the incoming wake properties play a crucial role in the airfoil force production. Therefore, the following question arises: can airfoil forces be estimated using the incoming wake properties? To answer this question, force predictions from unsteady aerodynamic models will be compared to the lift response from a reference cylinder-airfoil case. Theodorsen, Sears, and Atassi are the three analytical models that will be investigated in this study to assess current capabilities at estimating airfoil force production during cylinder-airfoil interactions. Since these theories are well documented in the literature, the following provides a short

description and lists assumptions for each model.

2.5.1 Theodorsen

The classical approach to estimate unsteady airloads of an airfoil is derived from unsteady thin-airfoil theory which uses potential flow to represent a thin airfoil with a distribution of vortices along the mean camber line. Theodorsen's function provides the solution to the unsteady airloads on a two-dimensional airfoil harmonically oscillating [73]. Figure 2.6 sketches the model with α representing the angle of attack of the airfoil. Since the airfoil is harmonically oscillating, its pitch angle varies in time as $\alpha(t) = \exp^{i2\pi ft}$ where f is the frequency of this oscillation. As thin-airfoil theory dictates, the airfoil is represented by a vortex sheet defining the airfoil's bound vorticity γ_b over the airfoil chord c. This vortex sheet can sustain a pressure difference and generates a lift force. The shed wake is also represented by a vortex sheet γ_w extending from the trailing edge to infinity. Within this wake, alternating circulation sheds from the trailing edge and convects downstream with the freestream velocity. Since the airfoil harmonically oscillates, the inflow conditions are time-varying which causes the bound vorticity on the airfoil to vary. In order to satisfy Kelvin's circulation theorem, vorticity sheds from the trailing edge in response to the change in bound vorticity. As long as the bound vorticity changes, the airfoil continues to shed wake vorticity, affecting the unsteady aerodynamic loads on the airfoil.

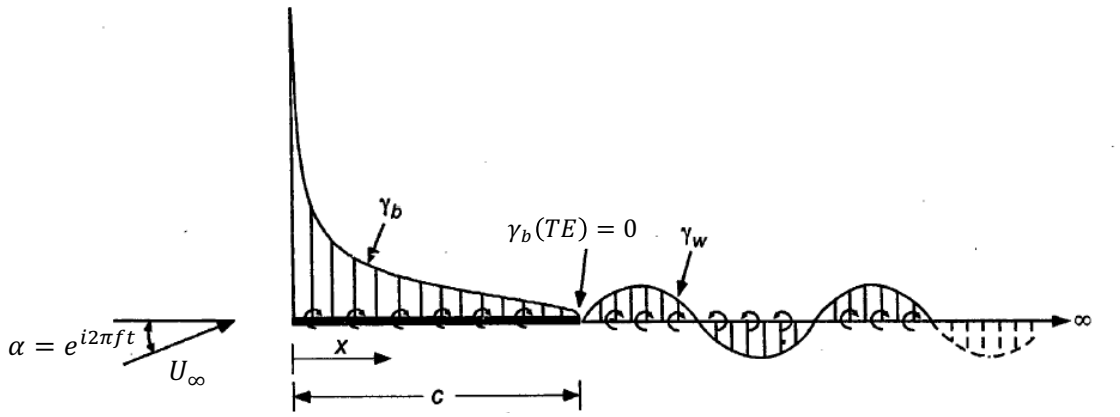

Figure 2.6: Sketch for Theodorsen's model. Adapted from Leishman [74].

Theodorsen's lift solution [74] for a purely pitching airfoil is given by:

$$C_l = \pi \frac{c^2}{4} \left(\frac{\dot{\alpha}}{U_\infty} - \frac{a\ddot{\alpha}}{U_\infty^2} \right) + 2\pi C(k) \left(\alpha + (\frac{1}{2} - a) \frac{\dot{\alpha} c}{2U_\infty} \right). \tag{2.1}$$

$C(k)$ is Theodorsen's function, a is the location of the pitching axis, and k is the reduced frequency. This solution depends on the airfoil pitching kinematics: angular velocity $\dot{\alpha}$ and angular acceleration $\ddot{\alpha}$. The first term in equation 2.1 is called the *added mass* effect and results from flow acceleration due to the angular acceleration of the airfoil. The second term in equation 2.1 represents the contribution from *circulatory* effects from the wake and bound vorticity. Theodorsen's function $C(k)$ serves to reduce the lift amplitude and introduce a phase lag to the *circulatory* term.

This analytical model is only valid under the assumptions of inviscid and attached flow, small angle disturbances, and fulfillment of the Kutta condition at the airfoil's trailing edge ($\gamma_b(TE) = 0$). However, Theodorsen's theory does not take into account viscous effects and the formation of vortices due to shear layers rolling-

up. Nonetheless, Theodorsen's solution provides good estimates when compared to experimental results from references [75,76], showing that this low order model is effective. The configuration under study in this thesis does not involve a harmonically oscillating airfoil, instead the airfoil remains static while encountering an oscillating inflow. It remains to be seen if Theodorsen's model accurately predicts airloads from the cylinder-airfoil configuration, and this will be addressed in chapter 6.

2.5.2 Sears

For a more representative model to inflow disturbance produced by the cylinder wake, von Kármán and Sears [25,26] provided an analytical solution for a thin-airfoil encountering a harmonic vertical gust. Figure 2.7 shows a sketch for this model. Similar to Theodorsen's theory, Sears's solution is derived from thin-airfoil theory resulting in a vortex sheet of length c describing the airfoil. A semi-infinite vortex sheet extending from the trailing edge forms the planar wake. However, the inflow condition is notably different as no kinematics are prescribed to the airfoil. Instead, a sinusoidal transverse gust v_g convects with the freestream velocity and encounters the static airfoil. This gust-airfoil interaction produces a time-varying upwash leading to an unsteady evolution of the airfoil's bound vorticity. In order to conserve circulation and satisfy Kelvin's circulation theorem, vorticity is continuously shed from the airfoil's trailing edge and influences the unsteady airloads. The unsteady airloads from the Sears model depend on two characteristics of the harmonic transverse gust: (1) the vertical gust amplitude v_0 and (2) the gust wavelength λ_g.

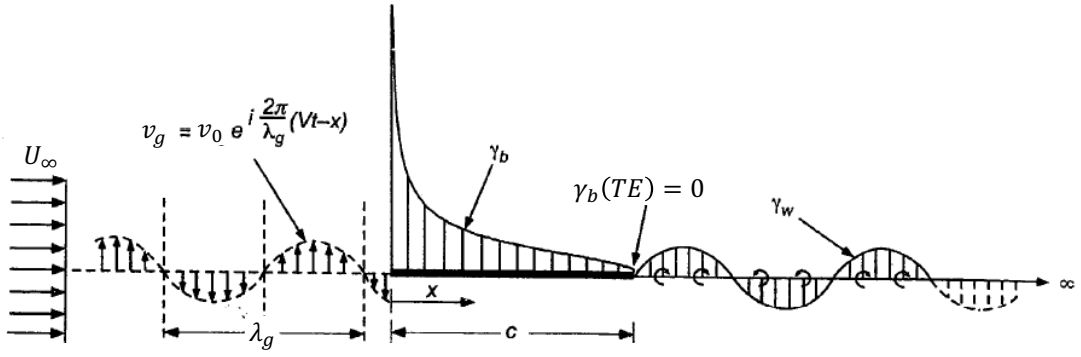

Figure 2.7: Sketch for Sears's model. Adapted from Leishman [74].

The unsteady lift coefficient from a thin airfoil encountering a sinusoidal transverse gust [74] is given by:

$$C_l = 2\pi \left(\frac{v_0}{U_\infty}\right) S(k_g) e^{i2\pi U_\infty t/\lambda_g} \tag{2.2}$$

where v_0 is the vertical gust amplitude, λ_g is the wavelength of the gust, k_g is the gust reduced frequency, and $S(k_g)$ is the Sears function. The gust reduced frequency is defined as

$$k_g = \frac{\pi c}{\lambda_g} = \frac{\pi f_g c}{U_\infty} \tag{2.3}$$

where the gust wavelength can be described by the gust frequency f_g. The Sears function $S(k_g)$ is a first-order transfer function relating the harmonic inflow conditions to the unsteady aerodynamic loads generated by the airfoil and is defined as

$$S(k_g) = \left(J_0(k_g) - iJ_1(k_g)\right) C(k_g) + iJ_1(k_g), \tag{2.4}$$

where J_n is the Bessel function of the first kind. For increasing reduced gust fre-

quency k_g, the Sears function $S(k_g)$ decreases the amplitude of lift coefficient and introduces a phase lag (or lead) because of its dependence on Theodorsen's function $C(k_g)$.

Sears's model is valid for inviscid and attached flow, small gust amplitudes ($v_0 << U_\infty$), and the Kutta condition holding at the trailing edge of the airfoil ($\gamma_b(TE) = 0$). Similar to Theodorsen's model, viscous effects and the formation of vortices from separated flows are not taken into account. The Sears model has the advantage that it models the cylinder wake upstream of the airfoil by a periodic transverse gust. However, the requirement of small gust amplitude limits the applicability of the model for cylinder-airfoil interactions since a cylinder wake can produce large perturbations. Finally, this model ignores flow distortion created by the airfoil's thickness, angle of incidence, and camber.

2.5.3 Atassi

The Atassi model builds on Sears's work by extending the gust to exhibit a streamwise component and include non-linear distortions from airfoil angle of attack, camber, and thickness [27, 28]. A visual representation of this model is sketched in figure 2.8. Taking into account the airfoil's thickness, incidence angle, and camber makes the Atassi model applicable to more configurations than the Sears model. The airfoil is subjected to a transverse gust with amplitude $\hat{v}$ with a reduced frequency of k_1 and a streamwise gust with amplitude $\hat{u}$ with a reduced frequency of k_2. According to Young and Smyth [77], $k_1\hat{u} + k_2\hat{v} = 0$ holds from the continuity

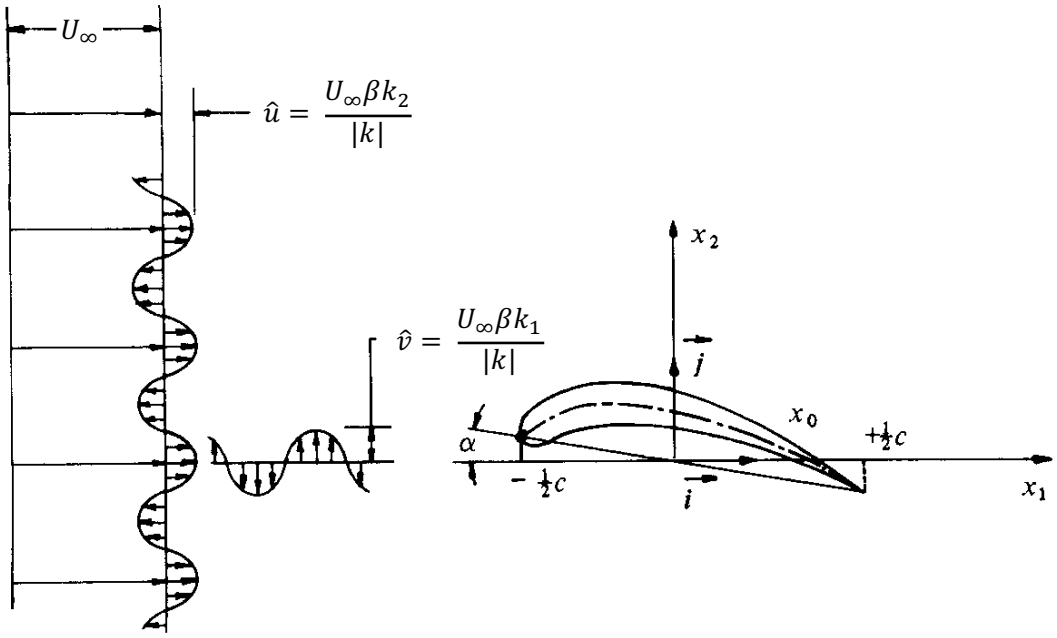

Figure 2.8: Sketch for Atassi's model. Adapted from Atassi [28].

equation and implies that the ratio of gust frequencies must equal the ratio of gust amplitudes, $k_1/k_2 = -\hat{v}/\hat{u}$. This is important in finding the gust strength parameter β as it can be derived from the amplitude of the oscillating inflow angle $\hat{\alpha_g}$. Wei et al. [78] approximate this parameter from

$$\hat{\alpha_g} \approx \frac{\beta k_1}{|k|} \tag{2.5}$$

where $|k| = \sqrt{k_1^2 + k_2^2}$ is the combined gust frequency amplitude and the gust flow angle $\hat{\alpha_g}$ can be determined from the flowfield. Combining all of these parameters, the airfoil's lift response to an arbitrary two-dimensional gust [28] is provided by:

$$C_l = 2\pi\beta A(k_1, k_2) e^{-ik_1 t} \tag{2.6}$$

where A is Atassi's function.

Similar to both Theodorsen and Sears models, Atassi's solution is valid for an inviscid, incompressible, attached flow. The gust must remain of small amplitude for a valid solution, although no restrictions are imposed on the airfoil. This allows the model to extend beyond thin airfoils in order to estimate airfoil forces on a wider range of geometries. Although no restrictions are given on the airfoil geometry, this model remains limited by the small amplitude of the incident gust and thus applies to cylinder-airfoil configurations where the cylinder wake produces small perturbations.

2.6 Summary and Research Objectives

The preceding sections provided an overview of airfoil force production in the cylinder-airfoil configuration. The wake flow structures from the cylinder provide an unsteady inflow for the airfoil and this interaction is responsible for changing airfoil performance compared to an isolated airfoil. At low angles of attack, the presence of freestream turbulence and velocity deficit cause a reduction in the lift curve slope at low angles of attack. These wake flow features induce noticeable change in the flow structures around the airfoil by changing the state of the boundary layer and the formation of leading edge vortices. With these new flow features, the airfoil increases its maximum lift coefficient and delays stall to higher angles of attack. The unsteady force response of the airfoil relates to the cylinder wake since the aerodynamic fluctuations synchronize with the cylinder vortex shedding frequency.

The airfoil force production depends on the relative location from the cylinder, with small gap distances suppressing the cylinder vortex shedding mechanism and large offset distances reducing the amplitude of fluctuations. Although past studies provide clear evidence that a turbulent wake significantly modifies the performance of a downstream airfoil, few studies determine the influence of varying the cylinder-airfoil configuration. There is a lack of aerodynamic knowledge relating to the effect of gap and offset distances between the two bodies and the geometry of the cylinder.

The purpose of this thesis is to understand how cylinder-airfoil interactions affect airfoil performance in a variety of configurations. To achieve a fundamental understanding of the involved flow physics when a turbulent wake encounters a NACA 0012 airfoil, the studied parameter space must be extended from what has been conducted in the literature. Airfoil force production trends must also be related to wake flow structures to understand modifications to the airfoil response. The objectives of the current work are as follows:

1. Identify and quantify wake flow features in the region between the cylinder and airfoil in order to fully characterize the unsteady inflow conditions upstream of the airfoil.

2. Collect lift, drag, and pitching moment forces at a Reynolds number of $\mathrm{Re}_c = 1 \times 10^5$ for a large set of cylinder-airfoil configurations which has not been investigated in previous experimental studies. Parameters of interest include the gap and offset distances between the cylinder and the airfoil, and variations in the cylinder size and cross-sectional geometry.

3. Determine the influence of cylinder-airfoil parameters on airfoil performance from time-averaged airloads, such as the lift curve slope, maximum lift, minimum drag, and stall angle.

4. Relate the time-averaged airfoil performance to key flow features to gain a fundamental understanding of the flow physics involved during cylinder-airfoil interactions.

5. Evaluate the effectiveness of force prediction results obtained from Theodorsen's, Sears's, and Atassi's models with unsteady force histories from CFD simulations.

Chapter 3: Experimental and Numerical Methods

The goal of this thesis is to study the cylinder-airfoil configuration and gain fundamental knowledge of the flow physics occurring in wake-airfoil interactions. This chapter describes the methodology of test campaigns performed to acquire experimental and numerical data. Measurements from experimental aerodynamics constitute the bulk of the data in this thesis. However, numerical methods are complementary as they are not susceptible to the same limitations from experimental test campaigns. Overall, the results presented in later chapters of this work establish a large database for studies involving the cylinder-airfoil configuration.

3.1 Measurements of the Cylinder-Airfoil Configuration

This first section outlines the experimental test campaigns by providing information on the research facility, test models, instrumentation and measurements techniques, and test parameters.

3.1.1 Wind Tunnel Facility

Experiments were performed in an open-circuit, low speed wind tunnel at the University of Maryland. Dimensions of the test section are $508 \times 711 \times 1143$ mm^3

(height × width × length) and the wind tunnel has a maximum operating speed of 60 $\mathrm{m\,s^{-1}}$ at standard atmospheric conditions. Within the test section, streamwise flow non-uniformity is less than 2 % and the freestream turbulence intensity is less than 0.6 % for freestream velocities ranging from $U_\infty = 10\,\mathrm{m\,s^{-1}}$ to $30\,\mathrm{m\,s^{-1}}$. Figure 3.1 shows a picture of the wind tunnel test section with two models installed.

Figure 3.1: Cylinder-airfoil configuration mounted in the wind tunnel test section.

3.1.2 Models and Configurations

Experiments in this thesis focus on the effect of an upstream wake encountering an airfoil. To achieve this in the wind tunnel, a cylinder is placed upstream of the airfoil to produce the turbulent wake (see figure 3.1). As this study aims to understand the fundamental flow physics of the cylinder-airfoil configuration, canonical geometries were used. A NACA 0012 profile with a chord of $c = 70$ mm and a span of $b = 505$ mm, resulting in an aspect ratio of $AR = 7.21$ was selected. Throughout this work, the airfoil dimensions remained fixed while the cylinder properties varied. A total of four cylinder-airfoil parameters were tested to investigate the effect of different wake properties and wake encounters on aerodynamic performance of a

downstream airfoil.

These four parameters include the gap distance G/D between the cylinder and airfoil, the cylinder diameter D, the offset distance z/D between the cylinder and airfoil, and the cylinder cross-sectional geometry. Figure 3.2 shows a detailed sketch for each tested parameter to aid the reader in visualizing these configurations.

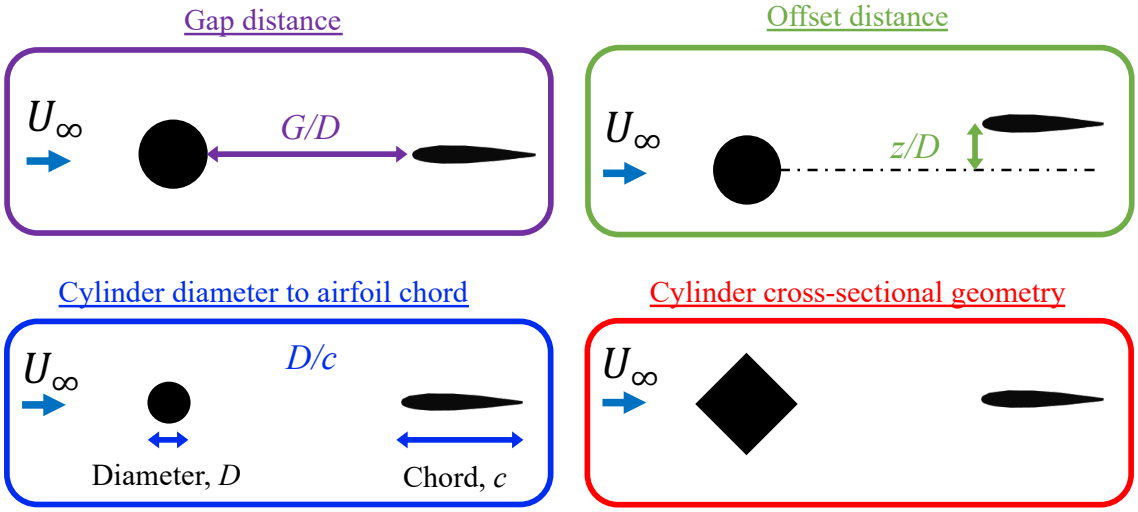

Figure 3.2: Sketches of the four cylinder-airfoil parameters tested.

The gap distance G/D is defined as the distance from the trailing edge of the cylinder to the leading edge of the airfoil when pitched at zero degrees. Varying the transverse spacing between the cylinder and airfoil defines the offset distance z/D. This distance is measured from the cylinder's centerline ($z/D = 0$) to the location of the airfoil's pitching axis, which is located at the quarter chord. While the airfoil chord did not change, different cylinder diameters were investigated to determine the influence of changing the wake size. This defines the cylinder-diameter-to-airfoil-chord ratio D/c, and three different values were tested. Finally, the influence of the cylinder cross-sectional geometry was evaluated by varying the cylinder geometry

from circular to square. The square cylinder was rotated by 45° with respect to the incoming freestream to produce two fixed separation points, one on the upper surface and the second on the lower surface. For a valid comparison with the circular cylinder, the diagonal of the square equals the smallest cylinder diameter.

To assess the effect of varying the cylinder-airfoil configuration on airfoil performance, each parameter was individually studied. Since airfoil performance depends on the angle of attack, each parameter was evaluated for a sweep of angles varying from $\alpha = -5°$ to 40°. The domain of the parametric study is summarized in table 3.1.

Table 3.1: Cylinder-airfoil parameter space.

G/D	z/D	D/c	Cylinder geometry
2, 3, 5, 7, 10, 15	0	0.36	Circular
3	0	0.36, 0.69, 1.04	Circular
3	$0, \pm 0.25, \pm 0.5, \pm 0.75$	0.69	Circular
5	0	0.36	Circular vs. Square

3.1.3 Force Measurements

Force data were measured on the NACA 0012 airfoil using a custom-built force balance system. The airfoil was suspended between two force balances to reduce reaction bending moments as shown in figure 3.3. A close-up view of the lower force balance is depicted in figure 3.3(b). Airfoil lift and drag were measured using two linear load cells (SM-25 and SM-10 by Interface), which were positioned 90° with respect to each other. According to the manufacturer's specifications, nonlinearity error is 0.03 %, hysteresis error is 0.02 %, nonrepeatability error is 0.01 %, and creep

error is 0.025 %. To eliminate friction in the force balance system, each load cell was mounted on linear air bearings (New Way Air Bearings, 0.75-in bushings) and supplied with compressed air as figure 3.3(b) shows. Airfoil pitching moment was measured about the quarter chord using a torque transducer (RTS-100 by Transducer Techniques) with the following specifications: 0.1 % of nonlinearity error, 0.1 % of hysteresis error, and 0.05 % of nonrepeatability error. No creep error was provided by the manufacturer for the torque transducer.

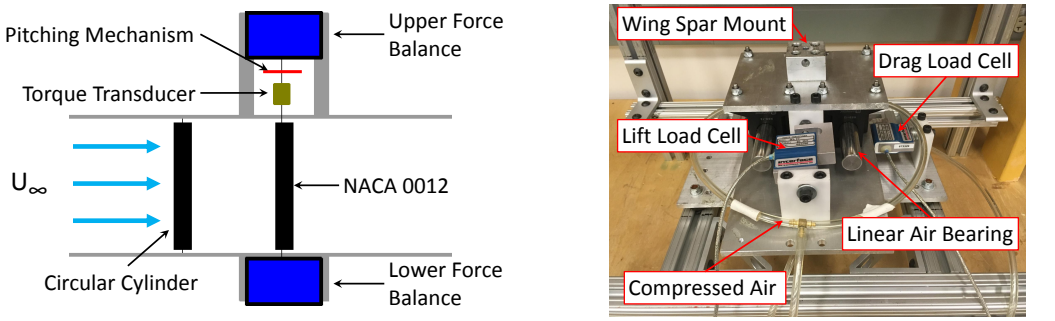

(a) Sketch of force balance system (b) Close-up view of lower force balance

Figure 3.3: Force balance setup. From Lefebvre and Jones [79].

The airfoil's angle of attack was held constant during data acquisition and was adjusted between measurements. An aluminum disk with equally spaced holes was mounted to the airfoil spar and allowed control of the static angle of attack. Force data were acquired in 1° increments.

3.1.3.1 Calibration

Each load cell was individually calibrated using precision weights of class M2. Figure 3.4 shows this calibration process for one of the linear load cells. The output of the load appears quite linear, and fitting a regression line to the measurements

quantified the nonlinearity error as the percentage difference between the output and applied load. The maximum nonlinearity error for all load cells was 0.12 %, suggesting a very linear behavior. However, each load cell is mounted to the force balance structure and inherently this will alter the precision of measurements.

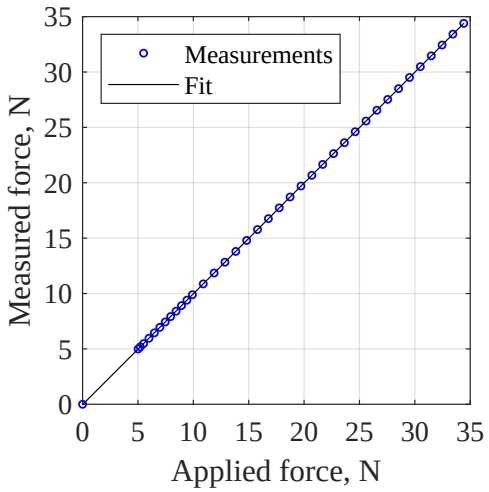

Figure 3.4: Calibration curve for one of the linear load cells mounted in the force balance system.

To quantify these errors, weights were applied to the airfoil in order to characterize the output of the force balance system. Figure 3.5 shows this is achieved by mounting a pulley on a shaft bearing to remove friction when applying the weight. In this picture, loads are applied in the streamwise direction, thus characterizing the drag component of the force balance. Four errors were determined: nonlinearity, hysteresis, nonrepeatability, and creep. Nonlinearity error is the deviation of the output compared to the applied load, and this maximum error was found to be 0.73 % for drag. Hysteresis is the deviation between the output for a reference load achieved by decreasing the load and the same reference load when increasing from a lower value. In the drag direction, the force balance hysteresis was 0.25 %.

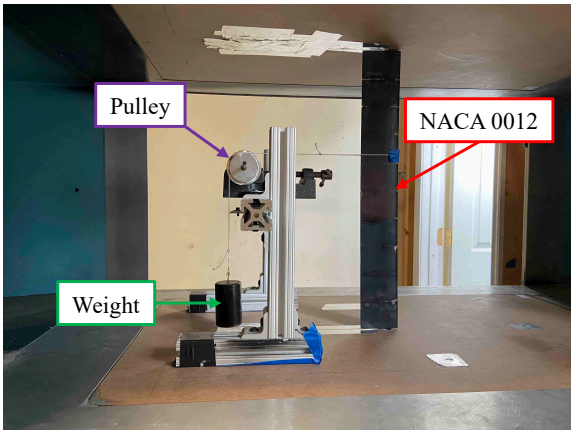

Figure 3.5: Setup used to assess the force balance system behavior.

Nonrepeatability is the error between outputs for repeated loading conditions, and this was 0.6 % in this study. Finally, creep error quantifies the drift in a measured output over 15 minutes and this was 0.02 % for the drag component of the force balance.

Repeating this process for the lift and torque components of the force balance provides a complete characterization of the system. Results are summarized in table 3.2 and shows small errors (≤ 1 %) for all force components. Only nonlinearity errors in torque are above this threshold value. Overall, this demonstrates the precision of the force balance system as uncertainties are generally 1 % or less.

Table 3.2: Characterization of the force balance system.

Loading direction	Nonlinearity error, %	Hysteresis error, %	Nonrepeatability error, %	Creep error, %
Lift	1.00	0.13	0.67	0.09
Drag	0.73	0.25	0.60	0.02
Torque	1.71	0.45	0.63	0.02

3.1.3.2 Data Acquisition and Time-Averaging

Lift, drag, and pitching moment forces were acquired using a USB-6341 data acquisition card from National Instruments and recorded with LabVIEW. Data were collected at a sampling frequency of 10 kHz over a duration of 30 s resulting in 3×10^5 samples. The airfoil's angle of attack remained constant during data acquisition and the wind tunnel speed was fixed during each angle of attack sweep.

Due to the unsteady cylinder wake upstream of the airfoil, a convergence study is necessary to determine if averaging over 30 s is sufficient. The convergence study was performed for the cylinder-airfoil configuration with a gap distance of $G/D = 3$ and measurements were acquired for 145 s. Time-averaged measurements of n samples after t seconds $C_x(t)$ were compared to the time-averaged value including all samples at $t = 145$ s $C_x(t_{max})$ and this deviation is expressed in the following equation

$$\hat{C_x}(t) = \frac{C_x(t)}{C_x(t_{max})} - 1. \tag{3.1}$$

Results of the convergence study at two angles of attack will confirm the required sampling time over a range of α tested in this thesis. Figure 3.6 shows these results for $\alpha = 5°$ and 30°. In this figure, the dashed black lines represent the $\pm 0.75\%$ deviation envelop of the true mean value. All force measurements, both at low and high angles of attack, converge to within 0.75 % in 30 s of the time-averaged value obtained from all available samples. This confirms that 30 seconds suffice for data acquisition in the cylinder-airfoil configuration as the time-averaged values are

accurate to 99.25 % of the true value.

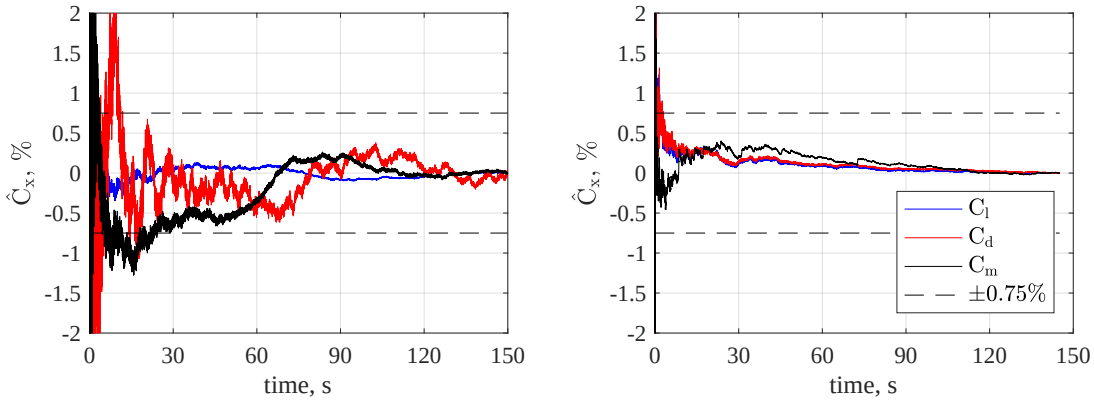

(a) $\alpha = 5°$ (b) $\alpha = 30°$

Figure 3.6: Time-averaging force coefficients over a long period of time in order to determine the minimum acquisition time.

3.1.3.3 Sensitivity to the Reynolds Number

Three different Reynolds numbers were tested to determine the sensitivity of force measurements, and this was performed using a subset of the previously defined cylinder-airfoil parameter space in section 3.1.2. The cylinder-airfoil gap distance was set to $G/D = 3$ with a cylinder diameter of $D/c = 1.04$, while the angle of attack varied from $\alpha = -5°$ to 20°. The Reynolds number in this study is based on the airfoil chord such that

$$\mathrm{Re}_c = \frac{\rho U_\infty c}{\mu} \tag{3.2}$$

where U_∞ is the freestream velocity upstream of the cylinder. Prior to each run, the air density ρ and dynamic viscosity μ were determined from ambient conditions using the ideal gas law and Sutherland's law [80]. As the airfoil chord did not vary in this study, the Reynolds number was controlled by setting the freestream velocity

of the wind tunnel.

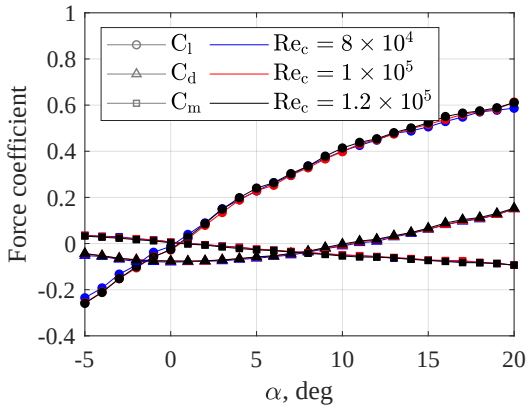

Figure 3.7: The effect of Reynolds number on time-averaged force coefficients when $G/D = 3$ and $D/c = 1.04$.

Figure 3.7 displays lift, drag, and pitching moment coefficients as the Reynolds number is varied from $\mathrm{Re}_c = 8 \times 10^4$ to 1.2×10^5. This range was selected as the upper and lower loading limits for the force balance. Time-averaged airfoil force measurements in the tested range are independent of Reynolds number variations, as no significant difference exists. This suggests that time-averaged airfoil force coefficients downstream of a cylinder are insensitive to Reynolds number in the range of 8×10^4 to 1.2×10^5. For the remainder of this thesis, force measurements will only be conducted at a Reynolds number of $\mathrm{Re}_c = 1 \times 10^5$ as this is well within the operating envelope of the force balance system.

3.1.3.4 Measurement Uncertainty

Characterization of the force balance system provided an analysis of the errors of the force outputs. As force coefficients depend on several measured quantities, each with their own uncertainty, propagation of these errors must be computed. For

a multivariate function $f = f(x_1, x_2, ..., x_n)$, the uncertainty in f is given by the following expression [81]

$$\sigma_f^2 = \sum_{i=1}^{n} \left(\frac{\partial f}{\partial x_i} \right)^2 \sigma_{x_i}^2 \tag{3.3}$$

where σ is the uncertainty of the desired quantity and the partial derivatives correspond to the sensitivity coefficients. These sensitivity coefficients can be thought as a weight applied to the uncertainty of the input quantities x_i [81].

To illustrate this process, an example is detailed for estimating the uncertainty in the air density ρ. Recall the ideal gas law can be expressed as

$$\rho = \frac{p}{R_{air} T} \tag{3.4}$$

where p is the ambient static pressure, T is the ambient fluid temperature, and R_{air} is the specific gas constant for air. Applying equation 3.3 produces the following expression to calculate the uncertainty in ρ

$$\sigma_\rho = \sqrt{\left(\frac{\partial \rho}{\partial p} \right)^2 \sigma_p^2 + \left(\frac{\partial \rho}{\partial T} \right) \sigma_T^2}. \tag{3.5}$$

This error can be expressed as the relative uncertainty by dividing equation 3.5 with equation 3.4 yielding the following relation

$$\frac{\sigma_\rho}{\rho} = \sqrt{\left(\frac{\sigma_p}{p} \right)^2 + \left(\frac{\sigma_T}{T} \right)^2} \tag{3.6}$$

where each term on the right hand side corresponds to the relative error of that

quantity. The relative errors for pressure and temperature are 9.2×10^{-6} and 0.0017, respectively, and as a result the relative error for the density is $\sigma_\rho/\rho = 0.17\,\%$.

Table 3.3: Relative errors of quantities used to calculate the lift coefficient.

Source of error	Variable symbol	Relative error value
Lift	σ_L/L	0.0122
Density	σ_ρ/ρ	0.0017
Velocity	$\sigma_{U_\infty}/U_\infty$	0.0029
Chord	σ_c/c	7×10^{-5}
Span	σ_b/b	0.0010

Using this procedure along with the definition of the lift coefficient $C_l = L/(0.5\rho U_\infty^2 cb)$, the relative error for C_l becomes

$$\frac{\sigma_{C_l}}{C_l} = \sqrt{\left(\frac{\sigma_L}{L}\right)^2 + \left(\frac{\sigma_\rho}{\rho}\right)^2 + \left(2\frac{\sigma_{U_\infty}}{U_\infty}\right)^2 + \left(\frac{\sigma_c}{c}\right)^2 + \left(\frac{\sigma_b}{b}\right)^2} \tag{3.7}$$

where the terms on the right hand side correspond to the relative errors in lift, air density, freestream velocity, airfoil chord, and airfoil span measurements. Table 3.3 summarizes the relative errors for each term in equation 3.7. This shows that the largest source of uncertainty is from force balance measurements. The total uncertainty in the lift coefficient is 2.7 % with a confidence level of 95 %. Repeating this process for drag and pitching moment measurements gives relative uncertainties in their corresponding force coefficients. Table 3.4 compiles the relative uncertainty for lift, drag, and pitching moment coefficients with values of 2.7 %, 2.3 %, and 3.9 %, respectively. All of these uncertainties are given with for a confidence level of 95 %.

Force measurements were repeated over three individual runs to assess the

Table 3.4: Measurement uncertainty in the time-averaged force coefficients.

Force coefficient	Uncertainty
C_l	2.7 %
C_d	2.3 %
C_m	3.9 %

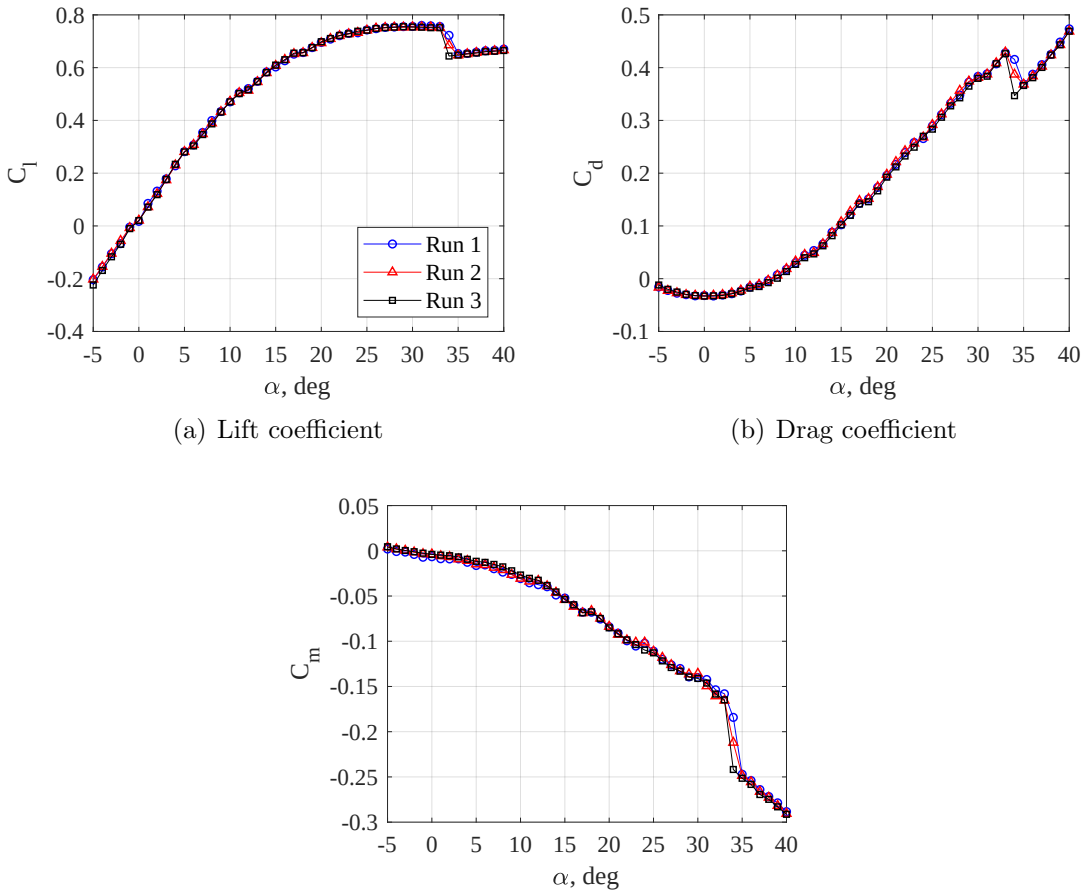

(a) Lift coefficient

(b) Drag coefficient

(c) Moment coefficient

Figure 3.8: Repeatability of the airfoil time-averaged force measurements when $G/D = 3$ and $D/c = 1.04$ at $\mathrm{Re}_c = 1 \times 10^5$.

repeatability of the force data. Figure 3.8 shows the lift, drag, and pitching moment coefficients for a gap distance of $G/D = 3$ and $D/c = 1.04$ where the nonrepeatability errors were largest. Overall, the maximum standard deviation from three independent runs was 0.010, 0.006, and 0.004 for lift, drag, and pitching moment

coefficients, respectively. However, the nonrepeatability error is significantly larger at $\alpha = 34°$ for all force coefficients and increases to 0.032, 0.028, and 0.023 for lift, drag, and pitching moment coefficients, respectively. This decrease in repeatability remains local and at higher angles of attack the agreement between all three runs is excellent. This local variation corresponds to the angle at which force data changes trends and is further discussed in chapter 5 as a consequence of the cylinder-airfoil interaction. Therefore, this angle of attack can be ignored when assessing the repeatability of force measurements as it does not pertain to the accuracy of the force balance system, and force measurement in the current work are deemed very repeatable.

3.1.4 Flowfield Measurements

Time-resolved, two component particle image velocimetry (PIV) was performed to quantify the flow around the cylinder-airfoil configuration. Flowfield measurements were captured for one cylinder gap distance of $G/D = 3$ while the cylinder diameter was $D/c = 1.04$. Variations in the airfoil's angle of attack were limited to three pitch angles, $\alpha = \{0°, 10°, 20°\}$. The purpose of these measurements was to visualize the wake-airfoil interaction and identify key flow structures that alter the airfoil performance in this configuration.

Figure 3.9 shows the PIV setup used to obtain flowfield images. For a given angle of attack, a double-pulsed Nd:YLF laser (Litron LDY-304, 30mJ/pulse, 10 kHz max) was mounted outside the test section and illuminated the flow with a light

sheet thickness of approximately 2 mm at the mid-span of each model. The floor of the test section was replaced with an acrylic plate providing optical access for two high-speed cameras (Phantom V641, 4 Mpx) to image the flow at 725 Hz (double-frame). Both cameras were tilted with respect to the laser sheet as figure 3.9(a) shows camera 1 was tilted upstream by 20° and camera 2 was tilted downstream by 8.5°. Each camera was equipped with a Nikon 50 mm f/1.8 lens and mounted on a Scheimpflug adapter to provide a uniform focus while tilted. Figure 3.9(b) shows the achieved field of view (FOV) for each camera, and the resulting velocity fields were stitched together. The air was seeded at the inlet of the wind tunnel with vaporized mineral oil using an aerosol generator (PIVTEC PIVlight30) producing droplets with an approximate diameter of 1 µm.

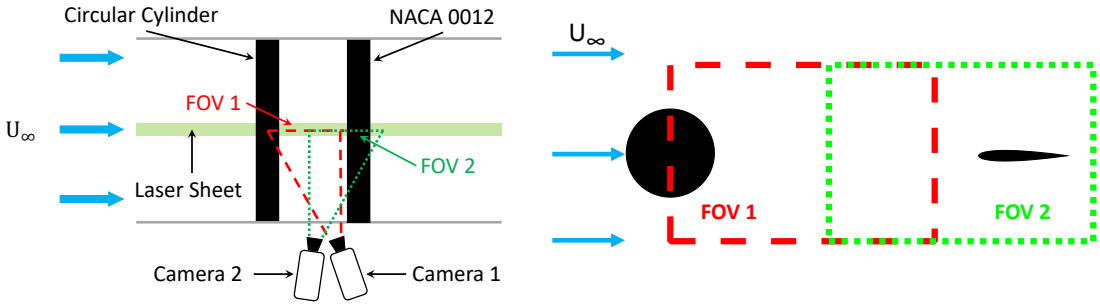

(a) Side view

(b) Top-down view highliting cameras FOVs

Figure 3.9: PIV setup. From Lefebvre and Jones [79].

For each angle of attack, over 2600 images were collected during data acquisition. Processing these images was performed using DaVis software (v8.1.3) by LaVision Inc. Prior to data acquisition, a calibration target (type 31) was used to establish a mapping function to correct warped images captured from the tilted cameras. To achieve a higher signal-to-noise ratio of raw images, a background

subtraction routine during preprocessing removed bright laser reflections from the surface of the cylinder and airfoil test models. A mask was applied to the laser shadow regions to omit these erroneous measurements from the data processing routines. The average particle displacement between each image pair was approximately 6 pixels. A multipass cross-correlation algorithm performed one pass with a window of 32×32 pixels and followed by two passes with a smaller window of 24×24 pixels with 50 % overlap. Circular windows were preferred to avoid diagonal biases from square windows. The resulting velocity field had a spatial resolution of 73 vectors per chord and the uncertainty was estimated at 2 %.

3.1.4.1 Smoke Flow Visualization

As PIV measurements were not acquired for variations of the offset distance and cylinder geometry, smoke flow visualizations provided a qualitative alternative. Figure 3.10 shows the smoke flow visualization setup. Due to hardware technical difficulties, a different laser (Quantel Evergreen 200, 200mJ/pulse, 15 Hz max) provided flow illumination for this test campaign. The same high-speed camera as in the PIV experiments was used, although it was placed normal to the light sheet removing the need for a Scheimpflug adapter. A wider FOV was achieved with a Nikon 35 mm lens attached to the camera.

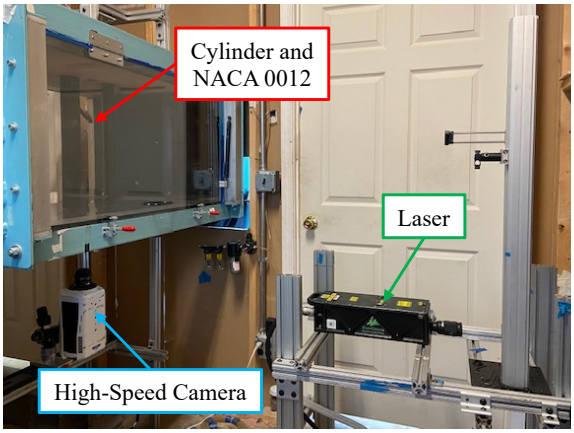

Figure 3.10: Smoke flow visualization setup.

3.1.4.2 Phase-averaged Flowfields

Phase-averaged velocity fields emphasize cyclical flow features, such as the periodic wake of a cylinder, while averaging out random events. In this study, the cylinder wake contains periodic flow structures superimposed with small turbulence scales. The instantaneous velocity $u(x,t)$ can be expressed using the triple flow decomposition [82],

$$u(x,t) = \overline{u}(x) + \tilde{u}(x,\phi(t)) + u'(x,t) \tag{3.8}$$

where $\overline{u}$ is the mean flow, $\tilde{u}$ is the periodic velocity component corresponding to coherent structures, and u' is the remaining velocity fluctuations due to turbulence. Phase-averaging isolates the periodic velocity field $\tilde{u}(x,\phi(t))$ at phase angle ϕ(t), which is determined from the proper orthogonal decomposition (POD) modes. For a detailed introduction to POD and other modal analysis techniques commonly used to study fluid flows, the reader is referred to references [83,84]. The selected technique

for phase-averaging involves finding the phase angle of the periodic component from flowfield measurements as described by van Oudheusden et al. [85]. Thus, the phase angle from velocity flowfields ϕ is given by

$$\phi = \frac{a_1\sqrt{\lambda_2}}{a_2\sqrt{\lambda_1}} \tag{3.9}$$

where a_n represents the first and second POD mode coefficients and λ_n is the corresponding eigenvalue. Once each flowfield is associated with a phase angle of flow periodicity, data are then sorted into phase bins before being ensemble averaged. A more detailed description of the procedure is found in reference [85].

3.1.4.3 Vortex Identification and Characterization

In order to quantitatively analyze vortices from PIV flowfield data, a vortex identification algorithm must be used to identify these flow structures. However, several approaches exist to identify vortices such as using the velocity gradient tensors for the Q-criterion [86], Δ-criterion [87], or λ_2-criterion [88]. There also exist methods based on the velocity field topology as Graftieaux et al. [89] provided the popular Γ_1 or Γ_2 techniques. All of these methods have been successfully used in various studies [88–91], but these vortex identification algorithms depend on user parameters to set thresholds or domain size. This subjective dependence on user inputs does not guarantee a universal identification of vortex structures. To obtain a more objective identification of vortices, an algorithm where the parameter has a physical and non-subjective interpretation will be employed in the current study.

Using the velocity gradient tensor $\nabla\vec{u}$, one can decomposed it into a symmetric tensor $\mathbf{S}$ describing the fluid deformation and an antisymmetric tensor $\mathbf{\Omega}$ describing rotation of the fluid. Truesdell [92] defined the kinematic vorticity number $\mathcal{W}$ as the ratio of fluid rotation to fluid deformation

$$\mathcal{W} = \frac{||\mathbf{\Omega}||}{||\mathbf{S}||} \tag{3.10}$$

where $||\cdot||$ is the Frobenius norm. Equation 3.10 has a simple physical interpretation with $\mathcal{W} > 1$ indicating fluid rotation dominates and $\mathcal{W} < 1$ corresponding to strong fluid deformation. Thus vortices are defined for regions where $\mathcal{W} > 1$, and it becomes clear that the kinematic vorticity number does not require a subjective threshold to identify vortices. Schielicke et al. [93] successfully implemented Truesdell's method to characterize cyclones from atmospheric data.

Vortex identification for the cylinder-airfoil configuration is shown in figure 3.11 with the yellow contour line representing regions where fluid rotation dominates ($\mathcal{W} > 1$). Calculating the centroid for each identified region provides an estimate for the vortex center and its location is represented by the magenta triangular markers. The kinematic vorticity number successfully identifies the three vortices in figure 3.11, as this method is able to separate the clockwise (blue region) vortex forming on the upper cylinder surface from the shed clockwise vortex. After successfully identifying vortices from PIV flowfield using the kinematic vorticity number, the circulation and core radius of each vortex can be characterized.

Estimating the circulation Γ of a vortex involves evaluating the following re-

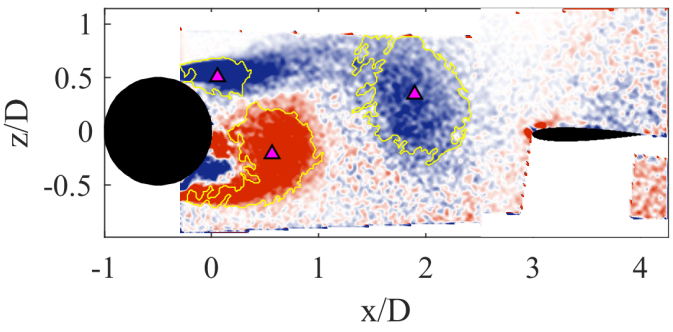

Figure 3.11: Vortex identification using the kinematic vorticity number. Clockwise rotation is shown in blue, whereas counterclockwise rotation is in red.

lation

$$\Gamma = \oint_C \vec{u} \cdot \mathrm{d}l = \int_S \vec{\omega} \mathrm{d}S \tag{3.11}$$

where the left-most integral sums the velocity contribution along the contour C. The integral on the right is obtained by applying Stokes's theorem and includes summing the vorticity $\vec{\omega} = \nabla \times \vec{u}$ over the area S delimited by the boundary C. In order to estimate the vortex core radius c_r, vortices are assumed to have a circular shape and the boundaries in figure 3.11 show this is a fair assumption. Thus, the core radius is found by $c_r = \sqrt{\frac{S}{\pi}}$.

3.1.5 Constant Temperature Anemometer (CTA)

Instantaneous velocity measurements were acquired via constant temperature anemometer (CTA) using a StreamLine Pro anemometer from Dantec Dynamics. A single hotwire probe (model P0141), with a wire length of 1.2 mm and wire diameter of 5 µm, measured the streamwise velocity. Measurements were only performed at the smallest cylinder diameter ($D/c = 0.36$) for a gap distance of $G/D = 9.6$. As

the flow in the near cylinder wake is highly two-dimensional, accurate measurements were not possible for smaller gap distances. Consequently, the test section length did not permit appropriate gap distances to be tested with the larger cylinder diameters.

Figure 3.12 shows the setup used for CTA measurements. Data were collected at the mid-height of the test section for two streamwise locations, $x/D = 8.6$ and 15.2, each corresponding to one cylinder diameter upstream and one chord downstream of the airfoil, respectively. The probe was traversed in the transverse flow direction from $z = -250\,\text{mm}$ to $250\,\text{mm}$ in $5\,\text{mm}$ increments, covering $70\,\%$ of the test section width. This resulted in 101 acquisitions per traverse run. Data were sampled at 2×10^5 Hz for $30\,\text{s}$ using a USB-6341 acquisition board with 16-bit resolution. To measure the effect of angle of attack on velocity measurements, two pitch angles were tested $\alpha = 0°$ and 20°.

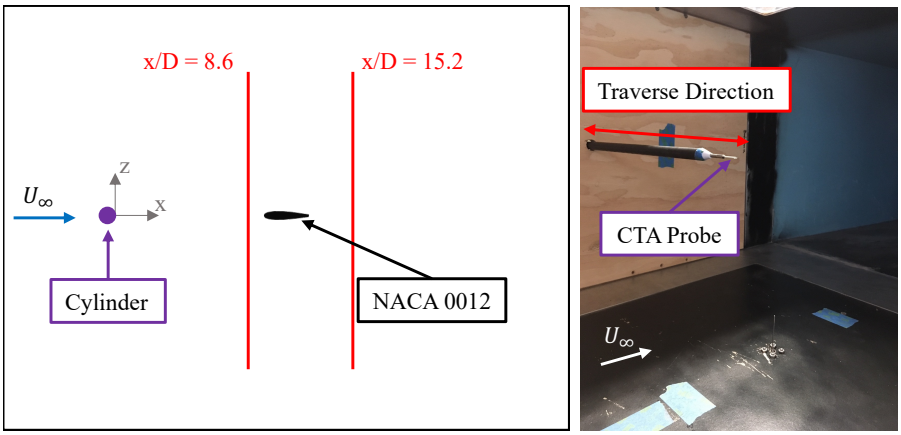

(a) Top view and locations of measurement planes

(b) Side view

Figure 3.12: CTA setup.

3.1.5.1 CTA Calibration

Prior to each experimental run, the hotwire probe was calibrated at the centerline ($z/D = 0$) when the test section was empty. During calibrations, the tunnel velocity was established using a pitot-static tube connected to a CPT6100 differential pressure and calibration velocities varied from $1\,\mathrm{m\,s^{-1}}$ to $35\,\mathrm{m\,s^{-1}}$. Figure 3.13 shows an example of a calibration curve obtained from fitting a fourth-order polynomial, which provides the best fit for CTA calibration data [94]. The error in the calibration curve is estimated to be 0.52 %.

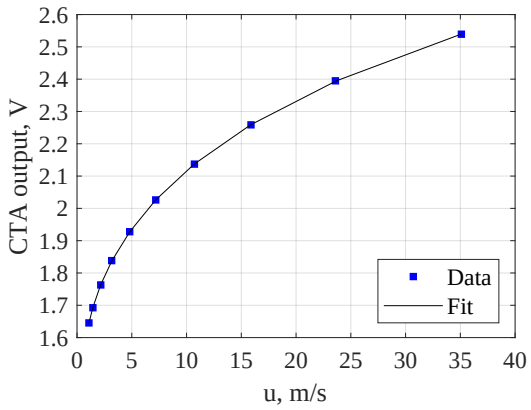

Figure 3.13: Sample calibration curve for the hotwire probe.

3.1.5.2 Uncertainty in CTA Measurements

Uncertainty analysis in hotwire measurements must be performed for the velocity reading from the anemometer and the derived quantities from these measurements. Following the recommended procedures from references [94, 95], the uncertainty of a velocity sample is first presented.

Three sources contribute to the uncertainty of a velocity measurement us-

ing the CTA: (1) uncertainty in the reference velocity used during calibration, (2) uncertainty in the curve-fitting of the calibration data, and (3) uncertainty in the resolution of the acquisition board. Table 3.5 provides a summary of the relative uncertainty for these sources. Uncertainty in the reference velocity is determined from the procedure described in section 3.1.3.4, while the standard deviation of the errors from curve-fitting define the uncertainty in the calibration curve. The combined relative uncertainty in a velocity sample measurement from the CTA system is the root sum square of each contribution and is found to be $\sigma_u/u = 1.2\,\%$ with a confidence level of 95 %.

Table 3.5: Uncertainty of a velocity sample obtained from CTA measurements.

Uncertainty source	Relative uncertainty
Reference velocity	0.0029
Calibration equation	0.0052
Digitization	1.5×10^{-5}

From the hotwire velocity measurements, several quantities are derived for the discussion in chapter 4. These flow parameters include the mean velocity $\overline{u}$, the turbulence energy dissipation rate ϵ, the turbulence integral (Λ) and Kolmogorov (η) length scales. For each calculated parameter, the propagated uncertainties are reported in the table 3.6 with a confidence level of 95 %.

Table 3.6: Uncertainty of reduced data from CTA measurements.

Flow property	Relative uncertainty
Mean velocity, $\overline{u}$	1.2 %
Turbulence energy dissipation rate, ϵ	3.7 %
Kolmogorov length scale, η	1.9 %
Integral length scale, Λ	3.6 %

3.2 Simulation of the Cylinder-Airfoil Configuration

Experimental methods were presented in the previous section and flowfields mesurements are obtained using PIV to study the cylinder-airfoil configuration. Although PIV is a non-intrusive measurement, this technique inherently introduces limitations to the measured data such as constraints on the FOV, coarse spatial-temporal resolution, and laser reflections on the body of interest. The restrictions on spatio-temporal resolution are adequate for the current work, however, reflections prevent PIV measurements from resolving data near the surface of the airfoil. Without surface measurements, the airfoil's boundary layer remains unavailable. For this reason, CFD simulations were performed by our collaborators at Georgia Institute of Technology to complement experimental results in this study with a complete flowfield with improved spatial and temporal resolutions. This section provides only the essential information pertaining to the numerical simulations described in the current work. For a more complete description of the numerical setup the reader is invited to read reference [96].

3.2.1 Mesh Description

A numerical setup of the cylinder-airfoil configuration with a gap distance of $G/D = 3$ and a cylinder diameter to airfoil chord ratio of $D/c = 1.04$ for an angle of attack of $\alpha = 0°$. CFD simulations were calculated using the NASA OVERFLOW solver which uses a structured overset grid. For this work, the entire wind tunnel was meshed resulting in five grids: inlet, test section, diffuser, cylinder, and airfoil. Overset grids were employed for the cylinder and airfoil regions.

Table 3.7: Grid dimensions (streamwise, normal, spanwise) for the numerical cylinder-airfoil simulations.

Inlet	Test section	Cylinder	Airfoil	Diffuser
(401,349,190)	(717,498,190)	(499,100,190)	(897,150,190)	(184,349,190)

Figure 3.14 illustrates the wind tunnel and overset meshes for a nearly identical cylinder-airfoil configuration used by Jarman et al. [96]. In the current study the airfoil overset mesh was modified to include a larger wake refinement than the one shown in figure 3.14(b). Grid dimensions are given in table 3.7 where the triplet numbers represent streamwise, normal, and spanwise grids. The cylinder's mesh includes 499 grid points discretizing the surface with 100 layers, whereas the airfoil's surface used 487 grid points with 150 layers. The remaining grid points in the airfoil's overset mesh represent the wake refinement region. Since this numerical simulation is three-dimensional, 190 points were used to define the spanwise direction, although only data from the mid-span were extracted to compare with experimental results.

A grid refinement study was performed to arrive at the selected grid dimensions and more information can be found in reference [96].

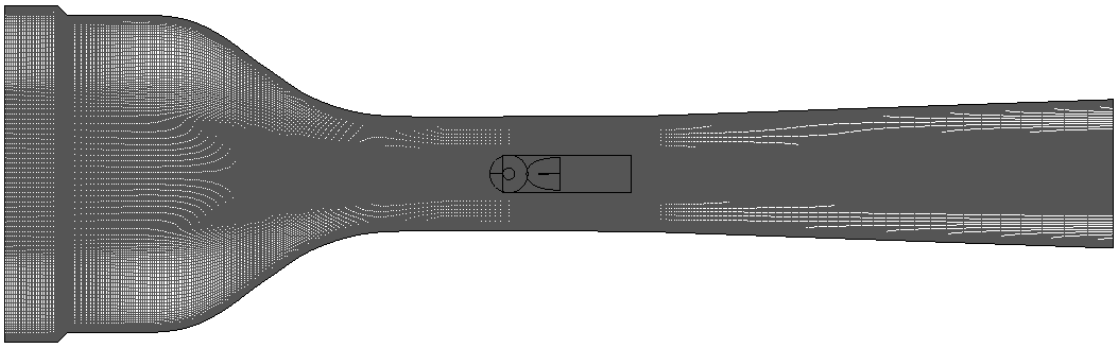

(a) Top-down view of full mesh

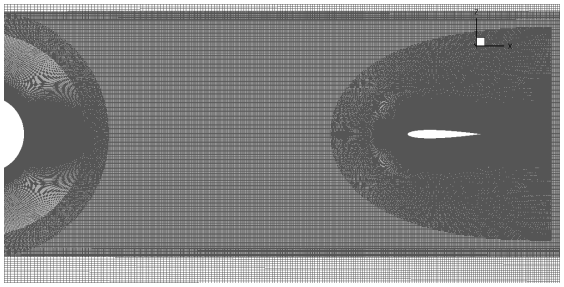

(b) Close-up view of overset meshes for cylinder and airfoil

Figure 3.14: Overset mesh used for the CFD simulations. Adapted from Jarman et al. [96].

3.2.2 Flow Solver

The NASA OVERFLOW code is a three-dimensional compressible flow solver and was used to solve the Navier-Stokes equations for the cylinder-airfoil configuration using a delayed detached eddy simulation (DDES). A Spalart-Allmaras turbulence model provided closure to the set of the Navier-Stokes equations. Invis-

cid terms were obtained from a diagonalized Beam-Warming scheme, while viscous terms were determined from a fourth-order central difference. In addition, the wind tunnel walls and model surfaces were treated as viscous surfaces. A low Mach number preconditioning was required due to the low velocity ($U_\infty \approx 22\,\mathrm{m\,s^{-1}}$) at the inlet of the test section for a compressible solver. The flow solution was implicitly time-marched with a $\Delta t = 5.5 \times 10^{-5}$ s. This time step was determined from a refinement study performed in reference [96]. Results obtained from the numerical simulations included both streamwise and transverse velocity fields, and only data from the midspan of the cylinder and airfoil within the test section region were extracted from the solver.

3.3 Chapter Summary

This chapter describes the methods employed to investigate the modifications of aerodynamic performance as a turbulent inflow interacts with a NACA 0012 airfoil. Wind tunnel experiments were performed using a force balance, particle image velocimetry (PIV), and hotwire anemometry to ascertain the influence of four cylinder-airfoil parameters on time-averaged airfoil aerodynamics and structures in the flowfield. Numerical simulations complemented these experimental techniques by capturing flowfield measurements with higher spatial resolution in regions inaccessible to PIV (e.g. the boundary layer). Results and analysis from these test campaigns are discussed in the following chapters of this thesis. A characterization of the cylinder-airfoil flow environment is presented in chapter 4, whereas airfoil

performance in the wake of a cylinder is given in chapter 5. A thorough discussion on wake-airfoil flow physics is found in chapter 6.

Chapter 4: Flow Characteristics of the Cylinder-Airfoil Wake

This chapter presents a detailed characterization of the cylinder-airfoil wake for gap distances of $G/D = \{2, 3, 9.6\}$, cylinder-diameter-to-airfoil-chord ratio $D/c = \{0.36, 1.04\}$, and two angles of attack $\alpha = \{0°, 20°\}$. Results from PIV and CTA measurements will identify wake flow structures, quantify turbulence intensities, estimate turbulence length scales, and measure wake frequencies. By characterizing this wake flow, the reader will become aware of the flow environment the airfoil operates in when downstream of a cylinder wake. This provides context to elucidate the underlying flow physics responsible for airfoil performance in the cylinder-airfoil configuration.

4.1 Wake Features

The velocity in the wake between the cylinder and airfoil was investigated to ascertain the influence of these bodies on wake flow features. Figure 4.1 shows the time-averaged streamwise velocity field as colored contours with streamlines superimposed for gap distances of $G/D = 2$ (left) and $G/D = 3$ (right). For this case, the airfoil's angle of attack was 0° while the cylinder-diameter-to-airfoil-chord ratio was $D/c = 1.04$.

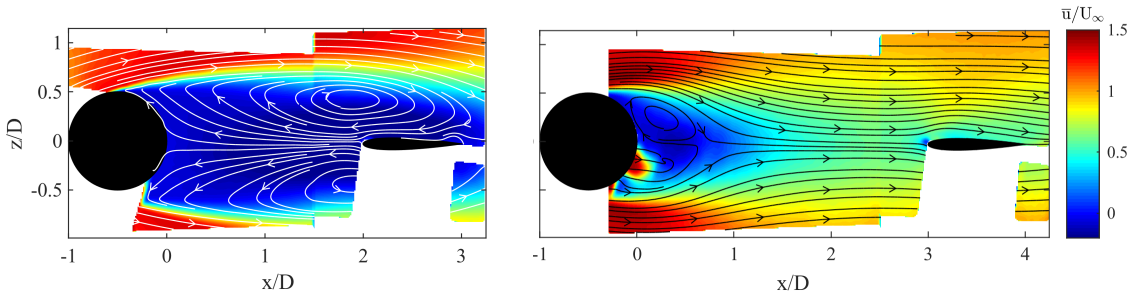

Figure 4.1: Time-averaged PIV streamwise velocity field measurements with streamlines for the cylinder-airfoil at $G/D = 2$ (left) and $G/D = 3$ (right) when $\alpha = 0°$.

At the smallest gap distance ($G/D = 2$), the cylinder-airfoil wake flow features differ from those of an isolated cylinder wake. Shear layers emanating from the surface of the cylinder extend far downstream, beyond $x/D = 3$, to create a large wake region that encompasses the airfoil. Low momentum fluid dominates the wake as the streamwise flow velocity remains less than $0.25U_\infty$. The streamlines also show two large, closed loops within the wake indicating the presence of a pair of counter-rotating vortices centered at $x/D = 2$ and $z/D = \pm\ 0.4$. The vortex pair is elongated in the streamwise direction as it interacts with both surfaces of the airfoil. Consequently, this wake produces a recirculation region and along the centerline ($z/D = 0$) flow direction reverses as shown by the streamlines. As the airfoil is embedded in the wake, it operates in reversed flow with fluid advancing from the trailing edge to the leading edge. For a gap distance of $G/D = 2$, the proximity of the airfoil substantially alters the cylinder wake by extending the low momentum, recirculation region to include the airfoil and thus modifying its flow environment. Since both the cylinder and airfoil induce a mutual aerodynamic influence on each other they are considered aerodynamically coupled. Indeed, previous

studies on tandem cylinders [59, 62, 97] and cylinder-airfoil configurations [65–67] report a critical gap distance of $G/D = 2$ to 3 which determines the aerodynamic coupling between bodies.

Increasing the gap distance to $G/D = 3$, figure 4.1 (right) shows the cylinder-airfoil wake flow features change compared to the $G/D = 2$ case. Shear layers continue to separate from the cylinder's surface; however, the recirculation region reduces to less than $x/D = 1$ and the counter-rotating vortex pair remains attached to the downstream side of the cylinder. Smaller vortices develop in the near wake of the cylinder, allowing the formation of these wake features to be independent of the downstream airfoil. As the cylinder wake recirculation region does not interact with the airfoil, flow in the wake follows the freestream direction even as the wake encounters the airfoil. Yet, in the cylinder-airfoil configuration the wake between both bodies is characterized by a deficiency in the streamwise velocity and this wake deficit functions as the inflow for the airfoil. The cylinder wake causes a reduction in the streamwise velocity by more than 40 % of U_∞ over the range of $1.5 < x/D < 3$ near the centerline. It is reasonable to expect this wake plays a critical role in altering airfoil performance in the cylinder-airfoil configuration. However, qualitatively the cylinder-airfoil wake flow features are analogous to the flow around an isolated cylinder and airfoil, thus there is minimal mutual aerodynamic influence between both bodies suggesting an aerodynamic decoupling at a gap distance of $G/D = 3$.

At a high angle of attack, $\alpha = 20°$, wake flow features remain akin to its low angle counterpart (see figure 4.2). At a gap distance of $G/D = 2$, a large wake

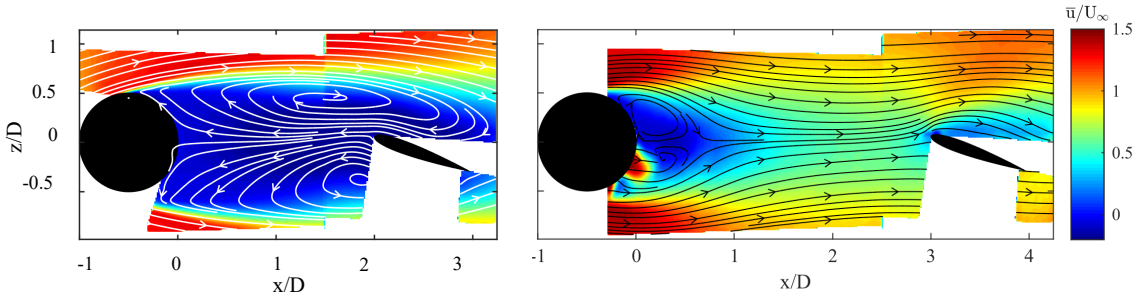

Figure 4.2: Time-averaged PIV streamwise velocity field measurements with streamlines for the cylinder-airfoil at $G/D = 2$ (left) and $G/D = 3$ (right) when $\alpha = 20°$.

with low fluid momentum is present along with a large counter-rotating vortex pair. Although the induced flow recirculation leads to reversal in the wake, the asymmetry caused by the high angle of attack also deforms the streamlines. This case clearly illustrates the strong aerodynamic coupling found in the cylinder-airfoil wake at this gap distance. In contrast, at a gap distance of $G/D = 3$, the wake does not exhibit strong deformation due to the high angle of attack of the airfoil. The near cylinder wake remains identical to the one in figure 4.1, further suggesting that the cylinder-airfoil are decoupled and both bodies continue to behave similar to isolated ones. Streamlines deform slightly upstream of the airfoil due to the increased angle of attack, and pronounced curvature in the flow occurs above the airfoil. These changes do not strongly affect the wake flow as the velocity deficit between the cylinder and airfoil persists as in the low angle of attack case.

It is clear from the results presented here that key wake features occur in the cylinder-airfoil configuration and these will play a role in determining performance on the downstream airfoil. The reduction in inflow velocity to the airfoil caused by the upstream cylinder wake is simple, yet this is a pivotal wake feature that affects

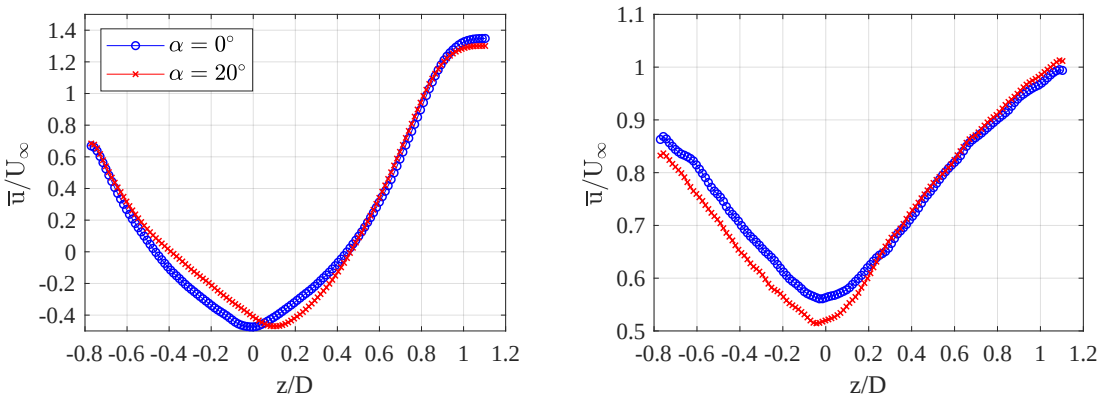

(a) $G/D = 2$ (b) $G/D = 3$

Figure 4.3: Time-averaged streamwise velocity profile at a quarter-chord upstream of the airfoil ($x/D = 2.75$).

airfoil performance in a time-averaged sense. Figure 4.3 characterizes the inflow velocity at a quarter-chord upstream of the airfoil ($x/D = 2.75$) in the cylinder-airfoil configuration. In this figure the abscissa is the transverse position of the PIV flowfield shown above, while the ordinate represents the streamwise velocity normalized by the freestream velocity. When the gap distance is $G/D = 2$ (see figure 4.3(a)), the streamwise velocity is negative from $z/D = -0.46$ to 0.45 with a maximum flow reversal of 47.5 % of the freestream value at the centerline for $\alpha = 0°$. Varying the angle of attack keeps the magnitude of flow reversal nearly constant, but the location of maximum recirculation shifts to $z/D = 0.1$ at $\alpha = 20°$.

For a gap distance of $G/D = 3$ (see figure 4.3(b)), the streamwise velocity is always positve, but the cylinder wake decreases the centerline velocity to 56 % at $z/D = 0$. Moving in the transverse direction shows the streamwise velocity returns to freestream conditions, but at low angle of attack the airfoil is only concerned of the inflow velocity near the centerline. At $\alpha = 20°$, the streamwise velocity is

minimum at $z/D = 0.04$ with 51 % of the freestream value, showing that airfoil's angle of attack further decreases the inflow velocity by 5 %. At this high angle of attack, the pressure side of the airfoil creates significant blockage which manifests as a 5 % streamwise velocity decrease for all negative z/D positions. This figure shows that the inflow to the airfoil in the cylinder-airfoil configuration is significantly reduced compared to the freestream velocity and a high angle of attack contributes to lowering the inflow velocity. Changes to this inflow will affect the aerodynamic forces on the airfoil when compared to an isolated airfoil.

4.2 Turbulence Intensity

This section addresses the unsteadiness of the wake of the cylinder-airfoil configuration by quantifying the amount of turbulence found in this flow. In order to characterize the turbulence intensity, the Reynolds decomposition [98,99] is used to separate a mean velocity $\overline{u}$ from its corresponding velocity fluctuations u' using the following relation:

$$u(t) = \overline{u} + u'(t) \tag{4.1}$$

where $u(t)$ is the instantaneous velocity. Turbulence intensity assesses the level of velocity fluctuations relative to the freestream velocity U_∞ by calculating the root mean square such that

$$\text{Turbulence intensity} = \frac{\sqrt{\overline{u'^2}}}{U_\infty}. \tag{4.2}$$

PIV flowfields were preferred for calculating the turbulence intensity due to the availability of both streamwise and transverse velocity components over a large spatial region instead of local streamwise velocity measurements from single wire CTA.

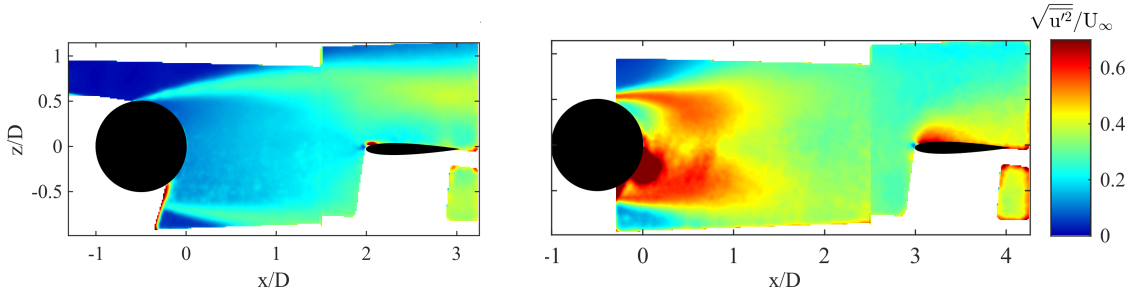

(a) Streamwise turbulence intensity

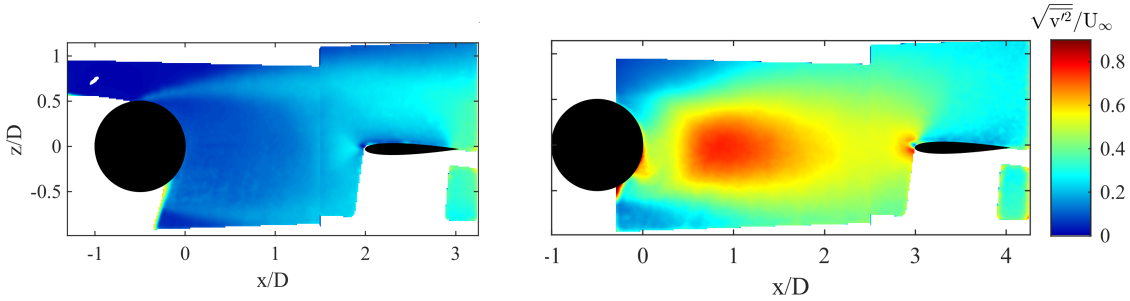

(b) Transverse turbulence intensity

Figure 4.4: Turbulence intensities for the cylinder-airfoil configuration for gap distances $G/D = 2$ (left) and $G/D = 3$ (right) when $\alpha = 0°$.

Figure 4.4(a) shows colored contours of streamwise turbulence intensity for both $G/D = 2$ (left) and $G/D = 3$ (right). Depending on the gap distance, the distribution and magnitude of turbulence intensity varies significantly and this correlates with the wake structure shown in the previous section. In the case with $G/D = 2$, streamwise turbulence intensity accumulates in the extended shear layers and regions above and below the airfoil. Turbulence fluctuates with values ranging from 30 % to 40 % of the freestream value, however streamwise velocity fluctuates

less than 20 % in the area between the cylinder and airfoil. This decrease in wake fluctuations is unlike the isolated cylinder wake, where vortices shedding from the cylinder's surface drives the unsteadiness in the wake. Hence, the suppression of vortex shedding is a direct consequence of the aerodynamic coupling between the cylinder and airfoil.

As the cylinder and airfoil gap distance increases to $G/D = 3$, turbulence intensity in the cylinder near wake strengthens. Large streamwise fluctuations, ranging from 45 % to 55 % of the freestream velocity, originate from the cylinder shear layers and form a two lobe structure near $0 < x/D < 1$ as shown in figure 4.4(a). It becomes clear that as the cylinder and airfoil decouple aerodynamically, strong fluctuations in the cylinder wake emerge indicating the vortex formation region typically found in the cylinder wake. Furthermore, strong streamwise turbulence intensity develops on the upper and lower surfaces of the airfoil, although due to the laser shadow the flow near the lower surface can only be inferred from the symmetrical nature of the flow configuration. This increase in turbulence intensity over the airfoil is explained by strong fluctuations present in the incoming wake due to the cylinder vortex shedding as it interacts with the airfoil.

In figure 4.4(b) contours of transverse turbulence intensity illustrate a similar trend according to the gap distance. A gap distance of $G/D = 2$ limits the transverse fluctuations to less than 10 % of U_∞ for the region between the cylinder and airfoil. The lack of fluctuations in the wake further demonstrates that the airfoil's proximity alters the wake structure by suppressing the cylinder vortex shedding. When $G/D = 3$, figure 4.4(b) (right) shows significant transverse turbulence intensity between the

cylinder and airfoil, with fluctuations up to 75 % of the freestream velocity near $x/D = 1$. Large transverse velocity fluctuations also appear at the leading edge of the airfoil as a result of the unsteady cylinder wake. However, the turbulence intensity decreases over the surface of the airfoil as the orientation of the body restricts vertical motions. This is most noticeable near $x/D = 3$, as the transverse turbulence intensity decreases from 40 % to 25 %.

The effect of increasing the angle of attack to $\alpha = 20°$ is shown in figure 4.5 for both $G/D = 2$ and 3. In general, asymmetry in the distribution of the turbulence intensities appear for $G/D = 2$ due to the aerodynamic coupling between the airfoil and cylinder. This manifests as more turbulence intensity accumulates in positive z/D locations, while turbulence fluctuations decrease for negative z/D locations due to the airfoil's trailing edge lower position. For $G/D = 3$, the airfoil's angle of attack does not alter the region between the cylinder and airfoil; however, both streamwise and transverse turbulence increases on the suction side of the airfoil. Streamwise fluctuations intensify while also extending to a larger region. These measurements from time-averaged PIV do not provide insight on the mechanism of this growth; however, the angle of attack increases the airfoil's interaction with the cylinder's wake enhancing velocity fluctuations. Increasing the angle of attack enhances velocity fluctuations due to an intense interaction between the airfoil and the cylinder's wake.

For a sufficiently large gap distance ($G/D \geq 3$), the unsteadiness in the cylinder-airfoil wake increases considerably, and the contour plots for turbulence intensity show that this relates to the cylinder wake and its vortex shedding mech-

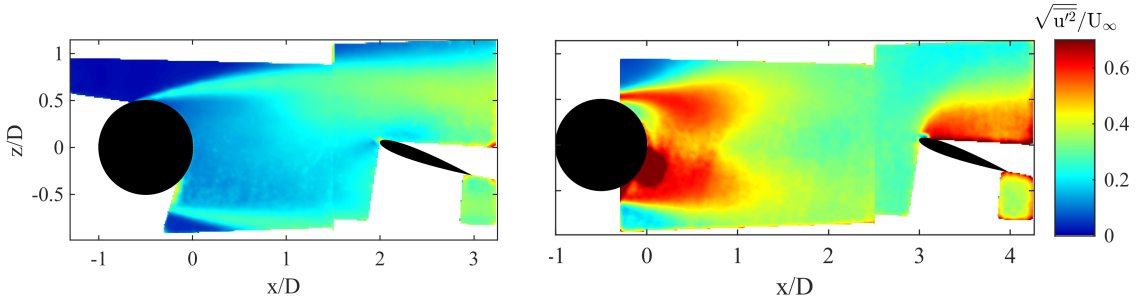

(a) Streamwise turbulence intensity

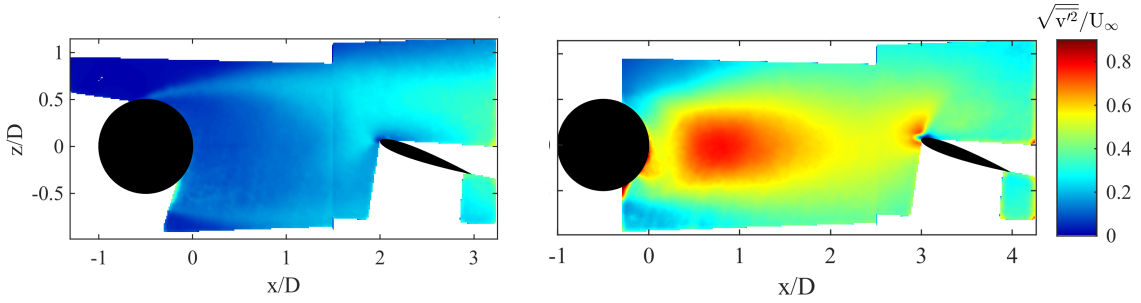

(b) Transverse turbulence intensity

Figure 4.5: Turbulence intensities for the cylinder-airfoil configuration for gap distances $G/D = 2$ (left) and $G/D = 3$ (right) when $\alpha = 20°$.

anism. As the turbulent wake encounters the airfoil, fluctuations develop near the leading edge, upper, and lower surfaces. Figure 4.6 summarizes the previous trends by plotting the spatial variation of turbulence intensities upstream and over the airfoil for both low and high angles of attack. At a quarter-chord upstream of the leading edge (see figure 4.6(a)) streamwise fluctuations depicted by the solid blue curve remain nearly constant between 25 % to 30 % of U_∞. Increasing the angle of attack to 20° produces insignificant change as shown by the blue square marker curve. Transverse fluctuations (dashed red line curve) are maximum at the centerline ($z/D = 0$) with fluctuations reaching 55.8 % of the streamwise velocity, and decreasing linearly for $|z/D| > 0.1$. The effect of increasing angle of attack is more noticeable for transverse fluctuations (red circular marker curve) as the maximum

increases by 1.7 % and shifts from the centerline to $z/D = 0.14$. Upstream of the airfoil, varying the angle of attack does not produce large change to the distribution of turbulence intensity (see figure 4.6(a)), although transverse fluctuations dominate the inflow to the airfoil.

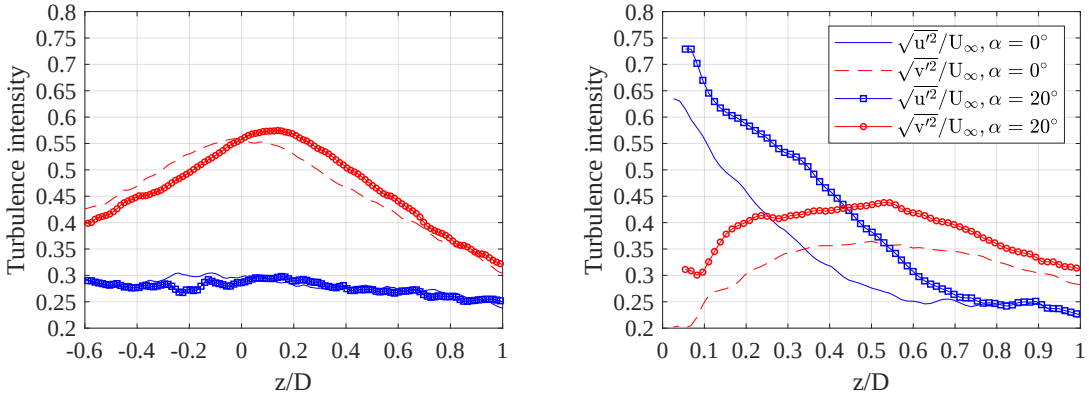

(a) $x/D = 2.75$ (b) $x/D = 3.25$

Figure 4.6: Streamwise and transverse turbulence intensity at two distinct locations for a gap distance of $G/D = 3$: (a) upstream of the airfoil and (b) at the airfoil's quarter-chord.

Over the airfoil and close to the surface ($z/D < 0.1$) as shown in figure 4.6(b), streamwise fluctuations (blue curves) dominate with a turbulence intensity greater than 55 % of U_∞. Transverse fluctuations (red curves) are capped at 25 % of the freestream value, but clearly the airfoil's interaction with the incoming wake produces impressive streamwise turbulence. Again the current results served to characterize the cylinder-airfoil flow environment, as the presented time-averaged quantities are insufficient to elucidate the underlying flow mechanisms. These results, however, demonstrate that an airfoil downstream of a cylinder wake operates in a highly turbulent flow; and with these large velocity fluctuations in the vicinity of the airfoil, performance will be affected.

4.3 Turbulence Length Scales

The previous section quantified the turbulence level the airfoil is exposed to in the cylinder-airfoil configuration. To further characterize the turbulence in this flow, knowledge of existing turbulence scales is essential. Results from this section use CTA measurements obtained for the cylinder-airfoil configuration with a cylinder diameter to airfoil chord ratio of $D/c = 0.36$. The gap distance for this case was set to $G/D = 9.6$ as this was the minimum distance required for accurate measurements from a single wire probe using the current setup. Both previous sections showed the cylinder and airfoil to be aerodynamically decoupled at $G/D = 3$, and this continues to hold at the selected gap distance of 9.6.

4.3.1 Measuring Length Scales

Turbulence is defined by a spectrum of scales, hence it is often meaningful to provide bounds of existing turbulence in a flow. Two such scales used in this section are the integral and Kolmogorov scales [98, 99]. The integral scale Λ represents the energy containing scale in turbulence and is estimated using

$$\rho(\tau) = \frac{\overline{u'(t)u'(t+\tau)}}{\overline{u'^2(t)}} \tag{4.3}$$

where ρ is the auto-correlation coefficient of the velocity fluctuations u' and τ is a time lag. From the auto-correlation equation 4.3, the integral time scale τ_Λ can be

determined from

$$\tau_\Lambda = \int_0^\infty \rho(\tau)\mathrm{d}\tau. \tag{4.4}$$

In applications, all measurements are finite, making the evaluation of equation 4.4 impractical and hence approximations are required. A commonly used approximation is to evaluate 4.4 up to the first zero crossing [100] and this method was selected for the current study. In order to convert the integral time into a length scale, Taylor's frozen turbulence hypothesis must be invoked which states that velocity fluctuations in turbulence are frozen and advect with the mean flow velocity [98,99]. This hypothesis allows for the computation of spatial turbulence statistics from temporal data measured at one point and hence the following can be used to calculate the integral length scale

$$\Lambda = \tau_\Lambda \cdot \overline{u} \tag{4.5}$$

where $\overline{\mathrm{u}}$ is the local mean streamwise velocity. Equation 4.5 is true only if the turbulence intensity $u'/\overline{u} << 1$ [98].

The Kolmogorov microscale defines the smallest turbulence scales present in a flow; smaller eddies dissipates into heat through viscous effects.

$$\eta = \left(\frac{\nu^3}{\epsilon}\right)^{\frac{1}{4}} \tag{4.6}$$

Equation 4.6 defines η as the Kolmogorov scale with ν defined as the kinematic viscosity of the fluid and ϵ as the rate of dissipation of turbulence kinetic energy. Accurately measuring ϵ creates difficulties in properly estimating this microscale.

Many different approaches exist in the literature to estimate the rate of dissipation of turbulence kinetic energy, but they typically fall into two categories: direct and indirect methods. A direct method that can be applied to one-dimensional velocity measurements (e.g. a single hotwire) is to measure the fluctuating velocity gradients in conjunction with Taylor's frozen turbulence hypothesis. The following relation is obtained:

$$\epsilon = \frac{15\nu}{\overline{u^2}} \overline{\left(\frac{\partial u'}{\partial t}\right)^2}. \tag{4.7}$$

Although this equation is elegant as it involves the velocity gradient which is easily measured experimentally, equation 4.7 only holds for isotropic and homogeneous turbulence [101–103]. In addition, the turbulence intensity must be small compared to the mean velocity for accurate calculations. Finally, measurements of the velocity gradients can be problematic as each turbulence scale down to the Kolomogorov scale must be resolved. This demands high temporal resolution in order to measure such short time scales. Another consideration which often limits common hotwire probes is the spatial resolution, as many commercially available probes are approximately 1 mm in length, thus direct measurement of Kolmogorov scales in most turbulence applications are impossible. Equation 4.7 was not considered to estimate the rate of dissipation of turbulence kinetic energy in this study for the previously stated reasons.

Instead, an indirect method was preferred based on Kolmogorov's second similarity hypothesis [104, 105]. In the inertial subrange, turbulence scales depend solely on the turbulent dissipation rate parameter ϵ. Thus, Kolmogorov's four-fifth

law [101, 102, 106] is given by

$$\overline{\Delta u'^3} = \overline{[u'(x+r) - u'(x)]^3} = -\frac{4}{5}\epsilon r \tag{4.8}$$

where $\Delta u'^3$ is the third-order structure function for the streamwise fluctuating velocity and r is a separation distance. Kolmogorov's four-fifth law is only valid for the inertial subrange, hence the separation distance must also lie within the inertial subrange. The advantage of the indirect method is that equation 4.8 is an exact relation which can be derived directly from the Navier-Stokes equations [102]. Since this method is only valid within the inertial subrange, and scales in this range are significantly larger than the Kolmogorov scales, hotwire probes can easily resolve scales both temporally and spatially. This eliminates inaccuracies from the direct method. Using Taylor's frozen turbulence hypothesis, equation 4.8 can be recast in the time domain and the following is used to estimate the rate of dissipation of turbulence kinetic energy:

$$\epsilon = -\frac{5}{4}\left(\frac{1}{\overline{u}\tau}\right)\overline{\Delta u'^3}. \tag{4.9}$$

Figure 4.7 shows an example of energy dissipation rate estimated using Kolmogorov's four-fifth law for a range of separation distances. The black square marker indicates the Taylor microscale, which delineates the end of the inertial subrange and is the largest of the viscous scales. Energy dissipation rate from equation 4.9 shows a plateau region for a wide range of separation distances ($r/c = 0.04$ to 0.15), indicating that the energy dissipation rate is nearly constant within this range. As

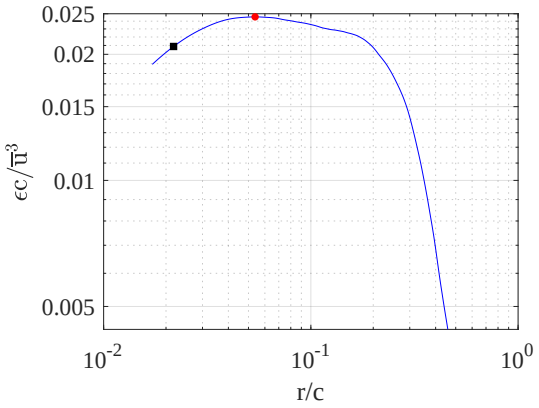

Figure 4.7: Turbulent energy dissipation rate ϵ obtained from Kolmogorov's 4/5 law for a range of separation distances r.

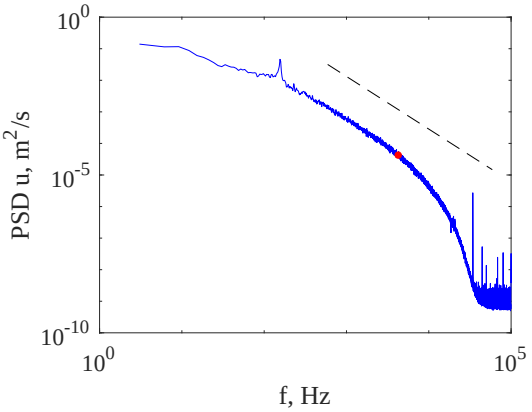

Figure 4.8: Power spectrum density (PSD) for the streamwise velocity upstream of the airfoil at $x/D = 8.6$ with a gap distance of $G/D = 9.6$.

long as the selected separation range is larger than the Taylor microscale and falls in the plateau region, the estimated energy dissipation rate is accurate. The red circular marker is the selected separation distance used to calculate ϵ for this case. Figure 4.8 shows the power spectrum density (PSD) for the corresponding streamwise velocity used to calculate ϵ in figure 4.7. Here the abscissa shows frequency as the measurements were temporally acquired via the CTA.

The dashed black line in figure 4.8 represents the -5/3 slope that character-

izes the inertial subrange. Measurements clearly capture the inertial subrange as a significant portion of the spectrum shares this slope. The red circular marker corresponds to the selected separation distance (here converted to a time lag via Taylor's frozen hypothesis) used to calculate ϵ, and the figure displays this value well within the inertial subrange; hence the indirect method is valid for this case. In the remainder of the study this same method and check was applied to all calculations of ϵ in order to estimate the Kolmogorov length scale.

4.3.2 Integral and Kolomogorov Length Scales

Before a discussion on the results of turbulence scales, a reminder of the selected cylinder-airfoil configuration for hotwire measurements is shown in figure 4.9. This sketch illustrates the smaller cylinder diameter, where the cylinder-diameter-to-chord ratio is $D/c = 0.36$ and the gap distance between both bodies is $G/D = 9.6$. Data were only acquired at one cylinder diameter upstream of the airfoil at $x/D = 8.6$ and the probe was traversed from $z/D = -1.4$ to 1.4, marked by the vertical red line, capturing the inflow to the airfoil.

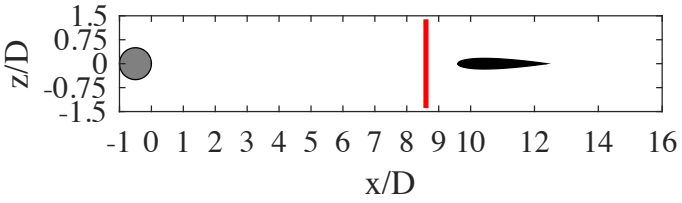

Figure 4.9: Sketch of the cylinder-airfoil configuration for CTA measurements of turbulence scales.

Results for the integral length scale are shown in figure 4.10 for low and high

angles of attack. In this figure, the abscissa axis represents the hotwire probe location in the transverse direction and the ordinate axis is the integral length scale Λ normalized by the airfoil chord. At zero angle of attack the integral length scale is maximum at $z/D = 0$ with a value of 0.97 and it decreases to a minimum of 0.21 away from the centerline. Because the cylinder and airfoil are aerodynamically decoupled at $G/D = 9.6$, periodic vortices shed from the cylinder. These coherent structures advect with the wake to encounter the downstream airfoil, causing Λ/c to be maximum along $z/D = 0$. The decrease in Λ/c with increasing $|z/D|$ suggests shed vortices from the cylinder wake remain in the vicinity of $z/D = 0$ and the airfoil does not influence their trajectories. Increasing the angle of attack to 20° shows a small increase in the maximum integral length scale to 1.03, however, this peaks shifts to $z/D = 0.4$. At a higher angle of attack the spatial distribution of integral length scales modifies upstream of the airfoil's leading edge, suggesting the airfoil's orientation influences these turbulence scales. Although the magnitude of Λ remains nearly independent of the angle of attack, the pressure side of the airfoil creates flow blockage for negative z/D and thus shifts the integral length scale distribution to positive z/D values.

Figure 4.11 shows the Kolmogorov length scales for the current cylinder-airfoil configuration. In a similar presentation as the previous figure, the spatial distribution is plotted for both $\alpha = 0°$ and 20°. At zero angle of attack, the Kolmogorov length scale is smallest at the centerline ($z/D = 0$) with a value of $\eta/c = 5.5 \times 10^{-4}$, and increases for $|z/D| > 0$. This behavior is expected as the flow configuration is symmetric for 0°. In contrast, as the angle of attack increases, the spatial distribu-

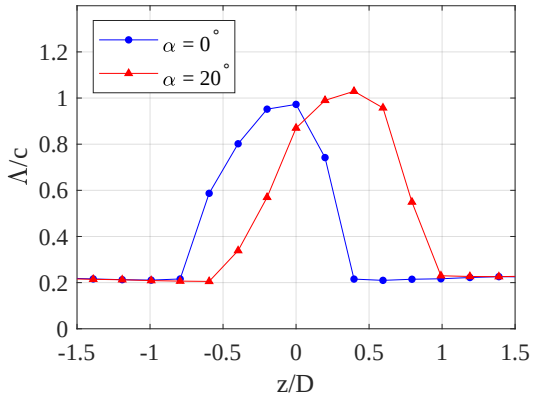

Figure 4.10: Integral length scale upstream of the airfoil at $x/D = 8.6$ with a gap distance of $G/D = 9.6$.

tion becomes asymmetric. The Kolmogorov scale increases to $\eta/c = 5.6 \times 10^{-4}$ and remains nearly constant for $z/D = 0.2$ to 0.8. A larger airfoil angle of attack causes the spatial distribution of these microscales to shift to positive z/D values, yet η/c is the same order of magnitude as at $\alpha = 0°$.

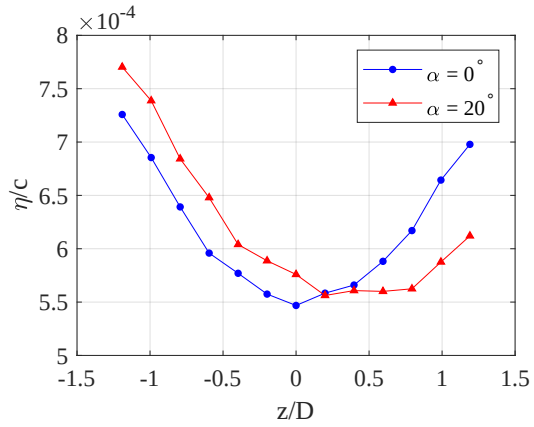

Figure 4.11: Kolmogorov length scale upstream of the airfoil at $x/D = 8.6$ with a gap distance of $G/D = 9.6$.

With the integral length scale as large as the airfoil's chord and the Kolmogorov scale on the order of 1×10^{-4} of the chord, these results indicate a wide range of turbulence scales present in the inflow of the airfoil. As the airfoil encounters these

scales, the aerodynamics will no doubt change, altering the airfoil performance. Varying the airfoil's angle of attack does not considerably change the magnitude of these scales, however, the spatial distribution is affected.

4.4 Wake Frequency Content

In order to complete the characterization of the wake flow in the cylinder-airfoil configuration, this section quantifies the wake frequency content. Parameters of the selected configuration were again $D/c = 0.36$ and $G/D = 9.6$, but measurements were acquired at two locations as shown in figure 4.12. The first measurement plane at $x/D = 8.6$ corresponds to one cylinder diameter upstream of the airfoil's leading edge, whereas the second location at $x/D = 15.1$ is one chord downstream of the airfoil's trailing edge.

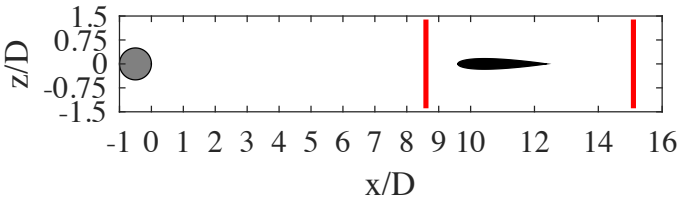

Figure 4.12: Sketch of cylinder-airfoil configuration for CTA measurements of wake frequencies.

The upstream location measures the wake frequency in the inflow to the airfoil (see figure 4.13) by plotting the PSD of the streamwise velocity. The PSD provides a distribution of power for each frequency component from the measured signal. Maximum power is present at low frequencies (large scales) and decreases at higher frequencies (small scales). Frequency is non-dimensionalized by the Strouhal number

which describes fluid oscillation with the following relation

$$\mathrm{St}_D = \frac{fD}{U_\infty} \tag{4.10}$$

where D and U_∞ are the cylinder diameter and the freestream velocity, respectively.

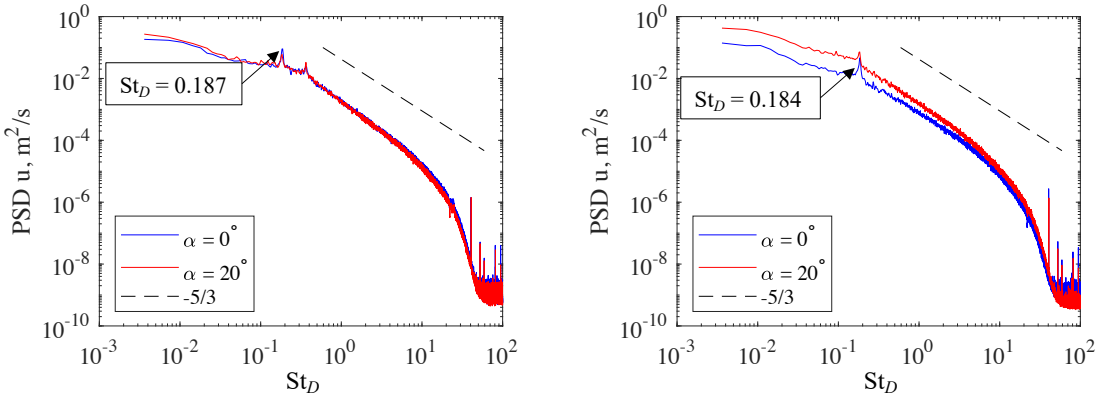

(a) $x/D = 8.6$ (b) $x/D = 15.1$

Figure 4.13: Frequency content in the cylinder-airfoil wake: (a) upstream of the airfoil and (b) downstream of the airfoil.

In figure 4.13(a), the PSD shows that more turbulent kinetic energy resides at low frequencies than at high frequencies. A dominant peak appears at $\mathrm{St}_D = 0.187$ suggesting that a single frequency characterizes the wake flow at $x/D = 8.6$ (upstream of the airfoil). Comparing to the frequency content of an isolated cylinder wake, the Strouhal number varies from $\mathrm{St}_D = 0.18$ to 0.21 indicating the frequency of vortex shedding [34–36] for Reynolds numbers ranging from 300 to 3×10^5. In the region between the cylinder and airfoil, the wake frequency is also characterized by the cylinder vortex shedding frequency. This is true because when the gap distance is $G/D = 9.6$, the cylinder and airfoil are aerodynamically decoupled, and thus there is no suppression of the cylinder vortex shedding mechanism. Furthermore,

the wake frequency upstream of the airfoil is independent of the angle of attack, as the dominant peak remains constant at 20°. For the tested angles of attack, the airfoil does not influence the frequency of the incoming flow. Figure 4.13(b) displays the PSDs at $x/D = 15.1$, which is downstream of both the cylinder and airfoil bodies. The dominant frequency at this wake location is nearly identical to its upstream counterpart with a value of $\mathrm{St}_D = 0.184$. This is well within the range of cylinder vortex shedding frequencies for this given flow configuration [34–36] hence the downstream wake frequency is not affected by the presence of the airfoil.

It appears that the wake frequency in the cylinder-airfoil configuration strongly relates to the cylinder vortex shedding frequency if the gap distance permits it. The frequency of the inflow to the airfoil can be thought as the airfoil's excitation frequency, while the downstream wake frequency hints that the interaction between the airfoil and the unsteady inflow does not modify the wake frequency. It is hypothesized the airfoil's aerodynamic response will match the inflow frequency.

4.5 Chapter Summary

This chapter provided a characterization of the wake flow in the cylinder-airfoil configuration for gap distances $G/D = \{2, 3, 9.6\}$ at angles of attack $\alpha = 0°$ and 20°. PIV measurements were used to describe the wake flow structures and turbulence intensities, and CTA data quantified turbulence length scales and wake frequencies. Several key findings can be harnessed from the presented results.

1. *Low momentum fluid characterizes the inflow to the airfoil.* For gap distances

$G/D \geq 3$ and at all angles of attack tested, the cylinder wake creates a region of low momentum fluid by decreasing the streamwise velocity by 50 %. This cylinder wake functions as the inflow for the downstream airfoil, causing the airfoil to operate in a low momentum fluid.

2. *Turbulence intensities are large in the vicinity of the airfoil.* As the airfoil interacts with the turbulent cylinder wake, the intensity of turbulence is greater upstream and along the surface of the airfoil.

3. *The airfoil interacts with a wide range of turbulence scales.* A large spectrum of turbulence length scales exist upstream of the leading edge of the airfoil. These scales range from $1c$ to $5.4 \times 10^{-4}c$.

4. *Cylinder vortex shedding frequency defines the wake frequency.* For $G/D \geq 3$, flow upstream of the airfoil oscillates at a frequency identical to the cylinder vortex shedding frequency. The airfoil is excited at a frequency of $\mathrm{St}_D = 0.18$.

Characterizing the cylinder-airfoil configuration shows that the flow region upstream of the airfoil is distinct from the flow around an isolated airfoil. These conclusions raise the following questions. How does the low momentum, turbulent inflow alter the airfoil's performance? Which turbulence scales contribute the most in modifying aerodynamic performance of the airfoil? Chapter 5 of this thesis will focus on the former, while chapter 6 will explore the latter question.

Chapter 5: The Aerodynamics of Wake-Airfoil Interactions

This chapter examines a parametric study of the cylinder-airfoil configuration to determine the modifications in aerodynamic performance of a NACA 0012 airfoil in a cylinder wake. Results from force measurements provide the time-averaged and unsteady force production of the airfoil for variations in four parameters. The following parameters were chosen to evaluate the positioning of the airfoil with respect to the turbulent wake and to investigate variations of the cylinder geometry: (1) the cylinder gap distance G/D, (2) the cylinder-airfoil offset distance z/D, (3) the cylinder diameter D normalized by airfoil chord c, and (4) the cylinder cross-sectional geometry.

5.1 Isolated NACA 0012 Airfoil: A Baseline Case

This section presents the time-averaged force coefficients and unsteady airloads associated with an isolated NACA 0012 airfoil. These results provide the reader with an understanding of the baseline airfoil aerodynamic response in a low turbulence inflow by setting the context of the study. Later sections focus on the modifications in airfoil performance due to the variations in the cylinder-airfoil configuration.

5.1.1 Time-Averaged Aerodynamics

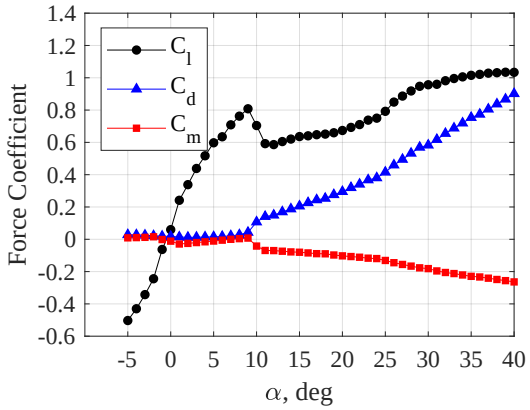

Figure 5.1: Time-averaged lift, drag, and pitching moment coefficients for the isolated NACA 0012 airfoil at $\mathrm{Re}_c = 1 \times 10^5$.

Figure 5.1 shows time-averaged force coefficients of the isolated NACA 0012 for $-5^\circ \leq \alpha \leq 40^\circ$ at $\mathrm{Re}_c = 1 \times 10^5$. Starting at $\alpha = 0^\circ$, the lift coefficient C_l of the airfoil increases with increasing angle of attack to a maximum value of $C_l = 0.81$ before stall occurs at $\alpha = 9^\circ$. An airfoil stalls when flow separates from the surface, causing a decrease in lift production. The current stall is considered abrupt for the NACA 0012 airfoil because the lift coefficient decreases suddenly from $C_l = 0.81$ to 0.59 as the angle of attack increases only by 2° (9° to 11°). Turning our attention to the drag coefficient at low angles of attack, C_d increases slowly and remains less than 0.04 up to $\alpha = 9^\circ$. Further increasing the angle of attack, the airfoil drag rises abruptly to $C_d = 0.11$ when $\alpha = 10^\circ$, indicating that stall is also characterized by a large increase in the drag coefficient. In the post stall region ($\alpha \geq 10^\circ$), drag continues to increase smoothly as it reaches values comparable to lift at $\alpha = 40^\circ$. Finally, the behavior of the pitching moment coefficient about the quarter-chord,

C_m, is also strongly dependent on the angle of attack. In the pre-stall region ($\alpha \leq 9°$), the pitching moment coefficient remains near zero and decreases to negative values, creating a nose down attitude, for post-stall angles of attack ($\alpha \geq 10°$).

5.1.2 Unsteady Airloads

Investigation of the airfoil unsteadiness requires quantifying both the amplitude and frequency of force fluctuations. To achieve this analysis, the root mean square (rms) and the fast Fourier transform (FFT) of time-resolved force measurements are calculated. Although the isolated airfoil does not operate in a turbulent wake, force unsteadiness appears as the airfoil stalls and the following results will illustrate this.

5.1.2.1 Amplitude of Fluctuations

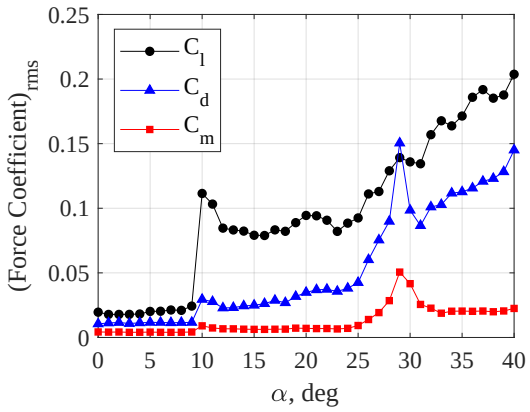

Figure 5.2: Values of fluctuating lift, drag, and pitching moment for the isolated NACA 0012 airfoil at $\mathrm{Re}_c = 1 \times 10^5$.

The amplitude of fluctuations for C_l, C_d, and C_m are shown in figure 5.2 for increasing α. Airfoil fluctuations for all force coefficients are less than 0.02 and nearly

constant prior to stall ($\alpha \leq 9°$), suggesting that aerodynamic forces are steady in this range for the given flow configuration. It is also noted that lift fluctuations are largest, whereas the amplitude for pitching moment fluctuations are the smallest. As the angle of attack increases to 10°, fluctuations for all force coefficients increase, although the amplitude in lift jumps significantly from $C_{l,rms} = 0.02$ to 0.11. Overall, lift fluctuations dominate across the tested angles of attack. A more detailed look reveals that the amplitude of fluctuations remains nearly constant for moderate angles of attack in the range of $10° < \alpha < 25°$ as values vary from 0.80 to 1.11. In comparison, the amplitude of fluctuations for lift and drag increases rapidly with large angles of attack, $\alpha \geq 25°$, reaching rms values of $C_{l,rms} = 0.2$ and $C_{d,rms} = 0.14$ at $\alpha = 40°$. However, the pitching moment does not follow this trend as $C_{m,rms}$ peaks at $\alpha = 29°$ and becomes independent of variations for $32° \leq \alpha \leq 40°$. This figure clearly demonstrates that airfoil lift, drag, and pitching moment coefficients are steady prior to stall and that unsteadiness develops with stall.

To understand the fluid mechanism responsible for fluctuating forces, figure 5.3 compares two time-averaged velocity fields of the NACA 0012 at $\alpha = 6°$ and 12°. Flowfield data in figure 5.3 were obtained by Lind et al. [107] using the same wind tunnel, NACA 0012 test model, and Reynolds number guaranteeing a similar flow around the isolated NACA 0012 in the present thesis. In this figure, the magnitude of the velocity contours is normalized by the freestream and the flow direction is displayed via velocity vectors. Since the NACA 0012 airfoil stall angle was identified at $\alpha = 9°$, figure 5.3(a) clearly shows flow attachment along the entire surface of the airfoil and the separation point appears near the trailing edge of the airfoil. As flow

travels along the entire chord, the airfoil creates a wake smaller than the airfoil's thickness. In contrast, as the angle of attack increases beyond stall (see figure 5.3(b)), flow is no longer tangent to the airfoil's surface. Instead, flow separates from the leading edge and this produces a large wake identifiable by the presence of low fluid momentum. Velocity vectors within this wake show that flow recirculates over the surface of the airfoil and consequently generates turbulence. In summary, this figure shows that prior to stall, flow over the airfoil is smooth with a small wake formed at the trailing edge. In contrast, the stalled airfoil produces a large wake characterized by unsteady flow due to recirculation and turbulence. Fluctuations in forces are thereby related to the flow state over the airfoil with large wakes increasing the unsteadiness of the C_l, C_d, and C_m.

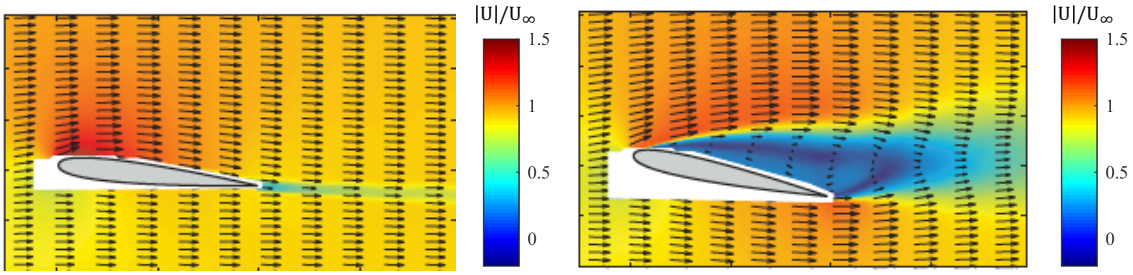

(a) $\alpha = 6°$ (b) $\alpha = 12°$

Figure 5.3: Time-averaged PIV velocity field measurements for an isolated NACA 0012 airfoil at $\mathrm{Re}_c = 1.1 \times 10^5$. Figure adapted from Lind et al. [107].

5.1.2.2 Airfoil Frequency Response

In order to complete the discussion of unsteady airfoil forces, the associated frequency of airloads must be investigated. This is achieved by performing spectral

analysis on force data, and a single case is first analyzed to illustrate the method. Figure 5.4 shows the single-sided amplitude spectrum of the pitching moment coefficient C_m for the NACA 0012 when $\alpha = 30°$ versus dimensional frequency f. Pitching moment was selected due to the increased signal-to-noise ratio. This spectrum identifies one dominant frequency at 106.5 Hz and several lesser prominent frequency contributions for $f \leq 50$ Hz. These low frequencies can be ignored as they were identified as the structural resonance of the force balance and play no aerodynamic role. Therefore, only the frequency at $f = 106.5$ Hz characterizes the unsteady response of C_m. Spectra for lift and drag coefficients at $\alpha = 30°$ also identified the same frequency, suggesting that the airfoil wake produces a periodic, unsteady aerodynamic response for a given α. For the remainder of this study, the airfoil frequency response is established from the pitching data. The same spectral analysis is repeated for angles of attack ranging from $\alpha = 0°$ to $40°$ in $5°$ increments.

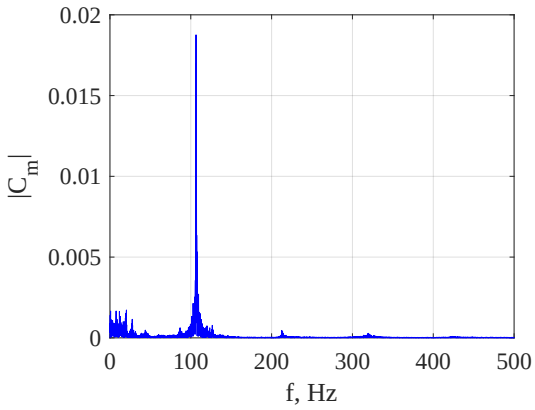

Figure 5.4: Single-sided amplitude spectrum of the pitching moment coefficient for the isolated airfoil at $\alpha = 30°$.

The dependence of the unsteady airloads dimensionless frequency on the angle of attack for the airfoil is presented in figure 5.5. Recall that the Strouhal number

St is defined for a characteristic length and velocity. Taking into account variations in angle of angle, the characteristic length is chosen as the projected height of the airfoil's chord in the streamwise direction. The Strouhal number is given by

$$\mathrm{St}_c = \frac{fc\sin(\alpha)}{U_\infty}. \tag{5.1}$$

Spectral analysis was performed over the entire range of α; however, a dominant frequency was only identified for cases where $\alpha \geq 20°$. At lower angles of attack, the FFT analysis failed to reveal a dominant frequency, suggesting that the flow around the isolated airfoil is not characterized by periodic events. Since flow is attached for low angles of attack, $\alpha \leq 9°$ (see figure 5.3(a)), the airfoil produces a small wake and this results in minimal force fluctuations. Indeed, figure 5.2 shows low rms for all three force coefficients, and thus the aerodynamics of the isolated airfoil are considered steady. For increasing angles of attack $\alpha = 10°$ to $19°$, the airfoil develops a wake (see figure 5.3(b)) and unsteady forces increase as figure 5.2 shows. However, the spectral analysis does not identify a dominant peak for these pitch angles, indicating that the turbulent wake created by the airfoil is aperiodic and contains a broad range of frequencies. Since a dominant Strouhal number can only be detected for $\alpha \geq 20°$, a sufficiently large angle of attack is required for the airfoil wake to become periodic.

The dimensionless frequency at $\alpha = 20°$ is $\mathrm{St}_c = 0.185$ and decreases with increasing angle of attack to $\mathrm{St}_c = 0.161$ at $\alpha = 40°$. This trend was also noticed by Huang and Lin [109] from experimental measurements of the vortex shedding

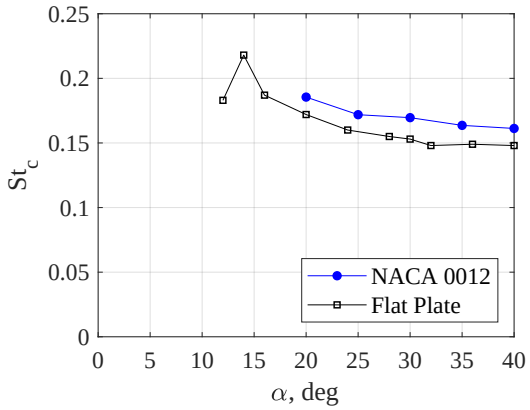

Figure 5.5: Variation of the Strouhal number with angle of attack for a NACA 0012 and a flat plate. Flat plate data is adapted from Fage and Johansen [108].

frequency in the wake of a NACA 0012. However, an explanation as to why the St_c decreases with increasing angle of attack is provided by flat plate studies. Fage and Johansen [108] measured the wake frequency downstream of an inclined flat plate and their data are reproduced in figure 5.5 for comparison with data obtained in this thesis. At $\alpha = 16°$, the evolution of the Strouhal number versus angle of attack for the flat plate trend agrees well with the airfoil in the present study, though the St_c values are systematically larger for the NACA 0012. This strongly indicates that the frequency behavior of the airfoil is comparable to that of a flat plate at moderate to large angles of attack. The flow mechanism for decreasing St_c with increasing α is determined to be the flow separation angle as stated by Chen and Fang [110] and Lind and Jones [111]. The St_c decreases more as the leading edge geometry of the model approaches a flat plate [110]. Thus as the frequency of the wake decreases with angle of attack, so does the frequency of airloads on the airfoil.

5.2 Effects of Varying Gap Distance

This section discusses the first parameter variation for the cylinder-airfoil configuration: the gap distance, G/D. As a reminder, G/D is the distance from the cylinder trailing edge to the airfoil's leading edge when the angle of attack is 0° as shown in figure 5.6. Six different gap distances are tested including $G/D = \{2, 3, 5, 7, 10, 15\}$, while the cylinder-diameter-to-airfoil-chord ratio is held constant at $D/c = 0.36$. Additionally, the cylinder is aligned with the airfoil's quarter chord.

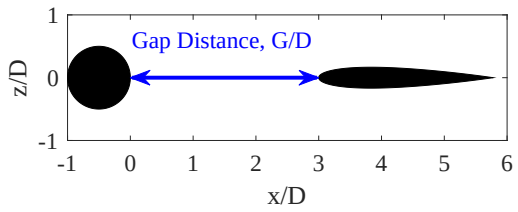

Figure 5.6: Sketch illustrating the gap distance parameter (G/D) defined for the cylinder-airfoil configuration.

5.2.1 Time-Averaged Aerodynamics

In order to understand how variations of the gap distance G/D in the cylinder-airfoil flow affect airfoil performance, measured forces are compared to the isolated airfoil. Figure 5.7 shows lift, drag, and pitching moment force coefficients for various gap distance as the angle of attack ranges from $-5°$ to 40°. The following discussion will first focus on lift, followed by drag, and finally the pitching moment.

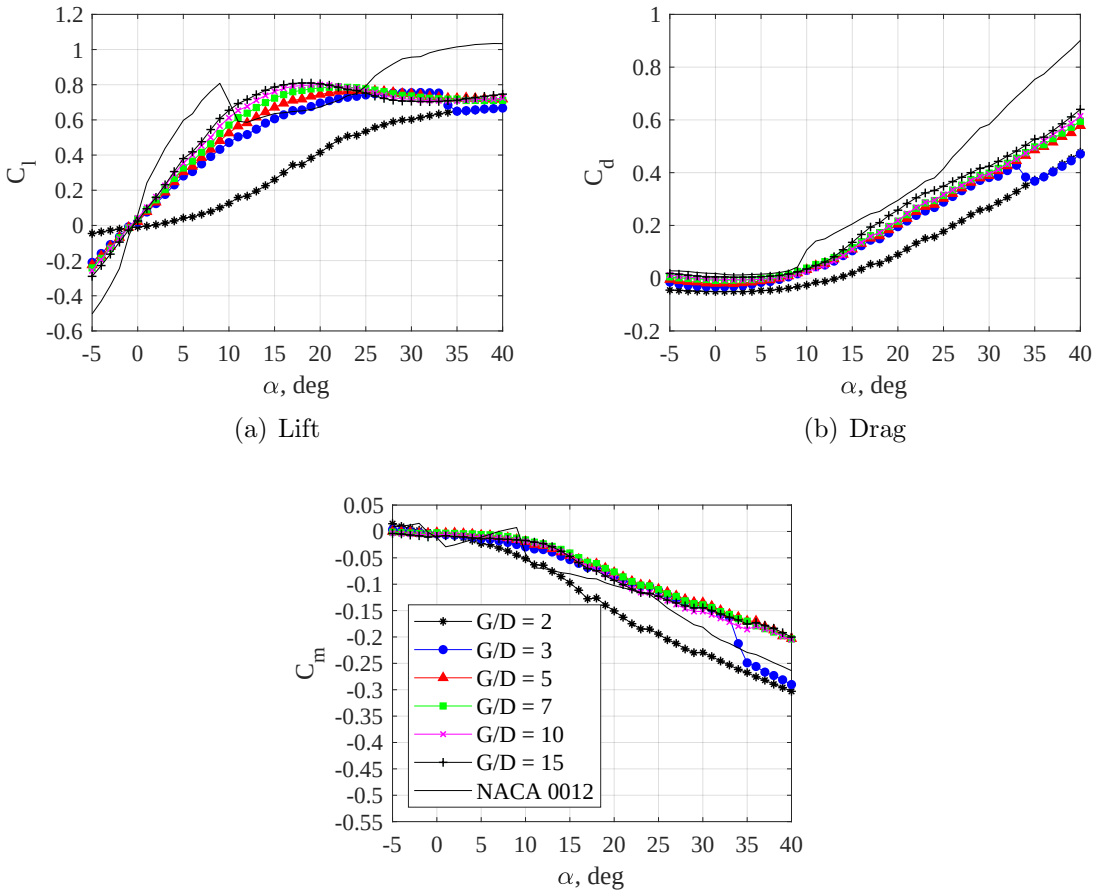

(a) Lift

(b) Drag

(c) Pitching moment

Figure 5.7: Influence of the gap distance parameter (G/D) on time-averaged force coefficients for $-5° \leq \alpha \leq 40°$ at $\mathrm{Re}_c = 1 \times 10^5$.

5.2.1.1 Lift

The influence of the gap distance on the airfoil's lift coefficient is shown in figure 5.7(a) as a function of angle of attack. Depending on the gap distance G/D, this figure distinguishes two distinct trends in C_l which relate to the aerodynamic coupling/decoupling between the cylinder and airfoil. For $G/D = 2$, the lift curve does not follow a typical lift behavior as C_l is concave up for $\alpha \leq 17°$ and concave down for $\alpha > 18°$. At $G/D \geq 3$, the lift curves have a similar trend to the isolated

airfoil case, although discrepancies appear.

Starting with $G/D = 2$, lift is zero at $\alpha = 0°$ which is exemplary of a symmetric NACA 0012 airfoil. Lift increases with increasing angle of attack, but the lift slope is not constant for $\alpha \leq 10°$. In fact, the lift slope is smaller than the isolated airfoil and continues to increase up to $\alpha = 17°$. This results in a significant reduction in the lift coefficient as C_l reaches 0.1 at $\alpha = 9°$ compared to $C_l = 0.81$ for the isolated airfoil. At higher angles of attack, the lift coefficient continues to be smaller than the isolated case, but C_l approaches comparable lift values for cases where $G/D \geq 3$. For the tested angles of attack, no maximum lift coefficient is observed and this is noticeably different than $C_{l,max}$ occuring at $\alpha = 9°$ for the isolated airfoil case. At a gap distance of $G/D = 2$, the proximity of the cylinder wake plays a critical role in modifying airfoil performance by greatly reducing lift and altering the concavity of the lift curve.

For $G/D \geq 3$, the lift coefficient follows the isolated airfoil trend. Lift is zero at $\alpha = 0°$ and C_l increases with increasing angle of attack up to a maximum before decreasing. However, figure 5.7(a) displays the influence of the gap distance on these trends. Similar to the isolated airfoil, the lift coefficient increases linearly for low angles of attack ($\alpha \leq 9°$), but the cylinder-airfoil gap distance reduces the lift curve slope. This effect is more pronounced for $G/D = 3$ and diminishes with increasing G/D, showing that the influence of the cylinder wake weakens with large gap distances. Due to the decrease in the lift curve slope at low angles of attack ($\alpha \leq 9°$), the cylinder-airfoil configuration leads to lower lift with $C_l = 0.43$ at $\alpha = 9°$ for $G/D = 3$ and $C_l = 0.61$ for $G/D = 15$ compared to $C_l = 0.81$ at $\alpha = 9°$ for

the isolated airfoil. Another feature affected by the cylinder-airfoil gap distance is the delay to higher angles of attack in the maximum lift coefficient, and this delay decreases with increasing G/D. Airfoil stall becomes smooth as the decrease in lift after $C_{l,max}$ is gradual and no longer abrupt.

An usual behavior occurs for $G/D = 3$ at $\alpha = 35°$, as the lift coefficient suddenly decreases and C_l is nearly identical to the trend found in $G/D = 2$. This suggests that the flow between the cylinder and airfoil aerodynamically couples at a sufficiently large angle of attack. Previous studies on tandem cylinders performed by Zhou and Alam [97] and Wang et al. [112], demonstrated that the critical gap distance for aerodynamic coupling can be increased if the downstream cylinder diameter is larger than the upstream one. As the airfoil is pitched at $\alpha = 35°$, it creates a blockage effect analogous to a cylinder and thus aerodynamically couples with the upstream cylinder due to a similar phenomenon as for tandem cylinders.

5.2.1.2 Drag

Each drag curve in figure 5.7(b) shows a similar shape as the isolated airfoil drag: the curve is concave up, drag is minimum at $\alpha = 0°$, and C_d increases with angle of attack. Yet, for all cylinder-airfoil gap distances the drag coefficient does not exhibit a sudden increase, further proof that the airfoil's stall behavior is modified in a cylinder's wake. In addition, a reduction in C_d exists for all gap distances at all angles of attack. Variations in the cylinder-airfoil gap distance reveal two trends. At $G/D = 2$, the reduction in drag coefficient leads to negative drag for angles of

attack less than 14° and drag remains lower compared to the other configurations. Increasing the gap distance to $G/D \geq 3$ also shows the drag reduction weakens with no negative drag measured for $G/D = 15$ and the drag coefficient approaches the isolated value. Only the gap distance $G/D = 3$ shows a decrease in drag at $\alpha = 35°$, and as the angle of attack continues to increase, the $G/D = 3$ case collapses to the $G/D = 2$ case. Again, this indicates that aerodynamic coupling between the cylinder and airfoil occurs at a large angle of attack for $G/D = 3$.

5.2.1.3 Pitching Moment

The influence of the gap distance on the pitching moment coefficient is shown in figure 5.7(c). For all gap distances tested, except for $G/D = 2$, the pitching moment behavior compares well with the isolated airfoil case. At $\alpha \leq 5°$, the C_m is near zero for all gap distances. Starting from $\alpha = 6°$, the pitching moment coefficient begins to decreases for $G/D = 2$ while it remains near zero for $G/D \geq 3$. Only once the angle of attack reaches 10° does the C_m decrease for all gap distances. For $G/D \geq 3$, C_m is nearly independent of the increasing gap distance and smaller in magnitude compared to the isolated airfoil case. The cylinder wake reduces the magnitude of the pitching coefficient on the airfoil if $G/D \geq 3$, but C_m becomes more negative at $G/D = 2$ and is larger in magnitude than C_m for the isolated airfoil. As has been the case for both lift and drag coefficients, at $G/D = 3$ the airfoil aerodynamically couples with the cylinder when the angle of attack increases past $\alpha = 35°$.

These results from time-averaged force measurements show that the influence of the cylinder wake dramatically alters lift, drag, and pitching moment for the airfoil. Gap distance effects decrease the lift curve slope, delay stall, and create negative drag.

5.2.2 Flowfields

Flow visualization is necessary in order to understand why force trends vary significantly for gap distances $G/D = 2$ and $G/D \geq 3$. Aerodynamic coupling between the cylinder and airfoil were shown to change the wake flow structure in chapter 4. Figure 5.8 shows instantaneous smoke flow visualization for $G/D = 2$ and 3 for angles of attack 0° and 10°.

For $\alpha = 0°$, figures 5.8(a) and 5.8(b) compare the influence of the gap distance G/D on the wake flow region between the cylinder and airfoil. At $G/D = 2$ (see figure 5.8(a)), the flow is coupled as the proximity of the airfoil suppresses vortex shedding from the cylinder wake. Shear layers emanating from the cylinder's surface define the wake and the airfoil is completely immersed with these shear layers. Vortex shedding in the cylinder wake reappears when the gap distance increases to $G/D = 3$ (see figure 5.8(b)), illustrating that the distance between both bodies is greater than the critical gap distance and the cylinder-airfoil configuration becomes aerodynamically decoupled. The vortex street formed by the cylinder directly encounters the downstream airfoil, depending on the gap distance G/D.

Figures 5.8(c) and 5.8(d) illustrate the ensuing flow as the angle of attack

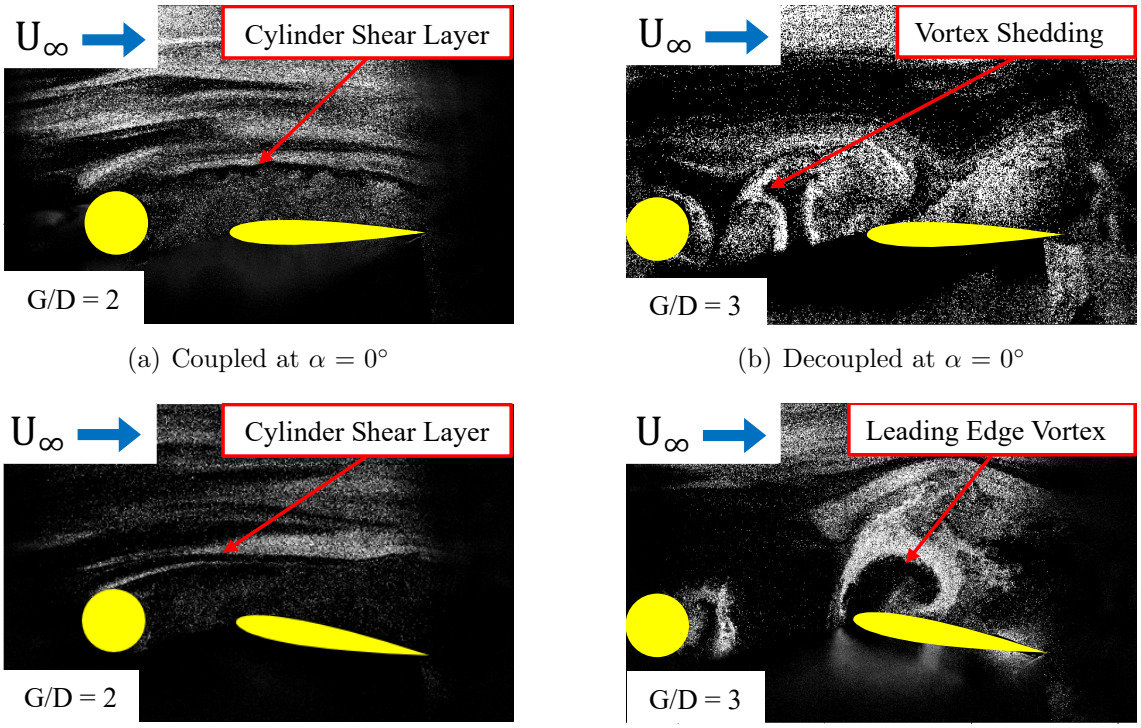

(a) Coupled at $\alpha = 0°$

(b) Decoupled at $\alpha = 0°$

(c) Coupled at $\alpha = 10°$

(d) Decoupled at $\alpha = 10°$

Figure 5.8: Smoke flow visualization for the cylinder-airfoil configuration when $D/c = 0.36$.

increases to $\alpha = 10°$. For the decoupled case when $G/D = 2$ (see figure 5.8(c)), the small gap distance continues to suppress the cylinder vortex shedding in the wake. Hence, the cylinder shear layers keep enclosing the airfoil. At a gap distance of $G/D = 3$ (see figure 5.8(d)), vortices encountering the airfoil form new flow structures as a leading edge vortex (LEV) forms.

This flow visualization demonstrates how the gap distance modifies the wake region between the cylinder and airfoil. In the coupled flow (see figures 5.8(a) and 5.8(c)), the airfoil interaction with the cylinder provides a constant wake structure due to the suppression of cylinder vortex shedding. In contrast, the decoupled flow (see figures 5.8(b) and 5.8(d)) shows that the interaction of the airfoil with the

cylinder vortex shedding wake produces a new structure, the LEV. As the cylinder wake acts as the inflow to the airfoil, these different wake structures manifest as distinct force trends (see figure 5.7) and increase airload fluctuations as section 5.2.4.1 will show.

5.2.3 Aerodynamic Coefficients Using the Local Dynamic Pressure

While the flow visualization does a good job at illustrating key wake flow structures, it does not provide insight into why the gap distance parameter affects the lift curve slope in figure 5.7(a). As previously stated, the region between the cylinder and airfoil is the inflow that the airfoil sees, and chapter 4 characterizes a streamwise velocity in this region corresponding to 52.5 % of the freestream. Force coefficients in figure 5.7 were calculated using

$$C_F = \frac{F}{0.5\rho U_\infty cb} \tag{5.2}$$

where the force F is normalized with the freestream dynamic pressure and therefore does not capture the velocity deficit found in the cylinder wake. To correct equation 5.2, the local wake dynamic pressure at G/D must be used instead. Durgesh et al. [71] successfully implemented this wake correction when calculating the lift and drag coefficients of a NACA 0012 in the wake of a square cylinder. As a result of using the wake velocity in equation 5.2, Durgesh et al. [71] noted the the lift curve slope was also corrected to the theoretical value of 2π.

Taking into account the reduced inflow to the airfoil created by the upstream

cylinder wake, the modified force coefficients are calculated by

$$C_F^* = \frac{F}{0.5\rho\overline{u}_{wake}cb} \tag{5.3}$$

with the reference velocity $\overline{u}_{wake}$ defined as the minimum, time-averaged wake velocity at G/D. Durgesh et al. [71] failed to provide a motivation for selecting the minimum wake velocity as the correct reference velocity. Measurements by Ong and Wallace [40] in figure 5.9(a) show the time-averaged wake velocity in the near wake of an isolated circular cylinder varies significantly with the transverse distance. Since the linear portion of the lift curves in figure 5.7(a) is limited to low angles of attack ($\alpha \leq 9°$), the leading edge of the airfoil will only deviate by 11 % of the cylinder diameter from the centerline when the airfoil pitches about the quarter chord by 9°. Clearly for a transverse distance of $z/D = 0.11$ ($y/d = 0.11$ using the labels in figure 5.9(a)), the minimum wake velocity is an appropriate inflow velocity for evaluating the correct aerodynamic coefficients in the cylinder-airfoil configuration.

The evolution of the centerline wake velocity is given in figure 5.9(b) using data from Cantwell and Coles [37] to supplement the lower spatial resolution data from Ong and Wallace [40]. The wake velocity for the correct normalization of aerodynamic can be obtained using results from these studies; however, data is limited to $x/D \leq 10$. In order to get a wake velocity for $G/D = 15$, a power law of the type $y = ax^b + c$ is fitted to the data measured by Cantwell and Coles [37] with a goodness of fit of 99.8 %. A wake velocity of $\overline{u}_{wake}/U_\infty = 0.834$ is evaluated at $x/D = 15$ from the fit equation.

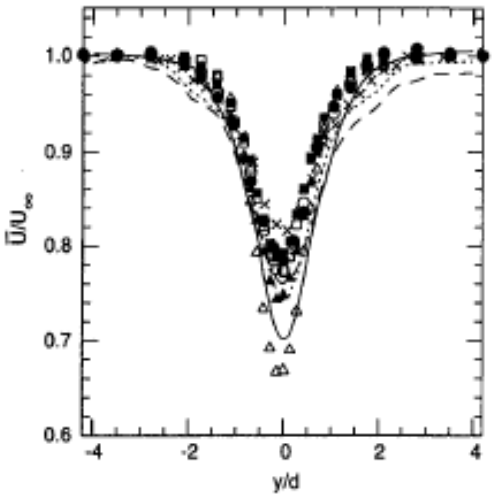

(a) Wake velocity at various streamwise locations. Figure adapted from Ong and Wallace [40].

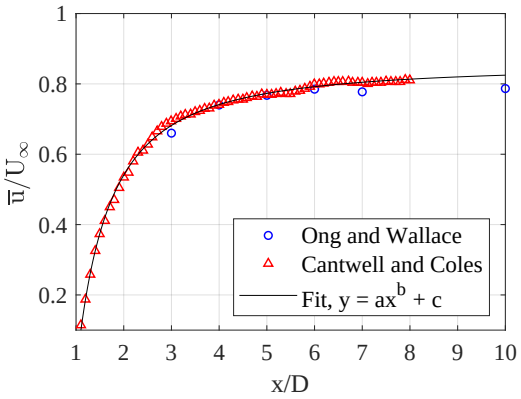

(b) Centerline wake velocity. Figure adapted from [37, 40].

Figure 5.9: Cylinder near wake velocity.

Table 5.1: Value of wake velocity for tested gap distances, G/D.

G/D	$\overline{u}_{wake}/U_\infty$
3	0.660
5	0.767
7	0.777
10	0.787
15	0.834

Figure 5.10 shows the modified lift, drag, and pitching moment coefficients using $\overline{u}_{wake}$ measured at the centerline of an isolated cylinder wake from references [37, 40] and these are summarized in table 5.1. Data from $G/D = 2$ has been removed in the current analysis to focus the influence of the gap distance parameter on the decoupled airfoil performance. Starting with the modified lift coefficient (see figure 5.10(a)), the lift curve slope is independent of the gap distance and all lift curves agree well with the theoretical slope 2π (black dashed line) for angles of attack less than 10°. The collapse of lift coefficients at low α suggests that the wake velocity is the appropriate reference velocity for force normalization in

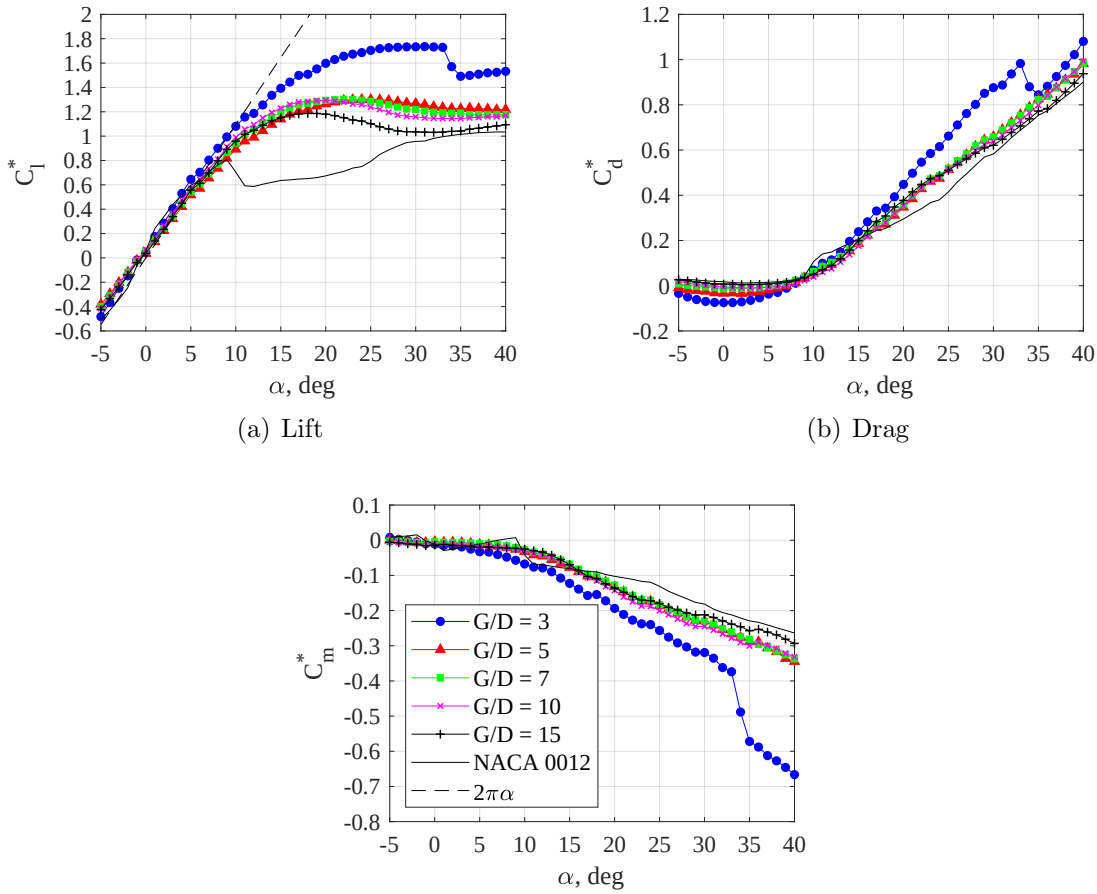

(a) Lift

(b) Drag

(c) Pitching moment

Figure 5.10: Influence of the gap distance (G/D) on time-averaged force coefficients corrected for the wake velocity deficit.

the cylinder-airfoil configuration. This demonstrates that the airfoil performance is altered in the presence of wake flow structures. In the wake of the cylinder, airfoil lift is significantly enhanced with C_l^* reaching a maximum of 1.74 and airfoil stall is delayed to $\alpha = 31°$. Lift enhancement and the delay in stall decrease as the gap distance G/D increases; however, the modified lift coefficient remains larger than the isolated airfoil lift.

Turning our attention to the modified drag coefficient, figure 5.10(b) shows negative drag of C_d^* = -0.07 for $G/D = 3$ and with a zero crossing between $\alpha =$

7° and 8°. C_d^* increases smoothly with increasing angle of attack, and by $\alpha = 14°$ drag becomes larger than the isolated airfoil case. Increasing the gap distance shows the cylinder wake influence weakens for low angles of attack as the modified drag increases to the isolated values. However for $\alpha > 15°$, the modified drag coefficient collapses for gap distances $G/D \geq 5$ and remains larger than to the isolated airfoil case.

The pitching moment coefficient (see figure 5.10(c)) is also affected by the corrected normalization as the magnitude of C_m^* increases compared to the isolated airfoil for $\alpha \geq 15°$. At a gap distance of $G/D = 3$, the cylinder wake produces the strongest influence as the modified pitching moment decreases significantly from the remaining G/D.

Using the local wake dynamic pressure when normalizing force coefficients reveals the true aerodynamic lift, drag, and pitching moment seen by the airfoil. The cylinder wake has a significant effect on the airfoil performance as the gap distance directly influences lift enhancement, delays stall, and produces negative drag.

To gain further insight on the role of the gap distance on lift enhancement and stall delay, figure 5.11(a) compares both the maximum lift coefficient and stall angle for the cylinder-airfoil configuration and the isolated airfoil. For all gap distances, $C_{l,max}^*$ is significantly larger than the maximum lift for the isolated airfoil as it demonstrates the ability of the cylinder wake to enhance airfoil lift. At $G/D = 3$, lift enhancement produces a maximum lift of 1.74 which is more than double the isolated airfoil value. $C_{l,max}^*$ decreases to 1.19 when the gap distance increases to

$G/D = 15$, revealing the cylinder wake still promotes considerable lift enhancement for large G/D.

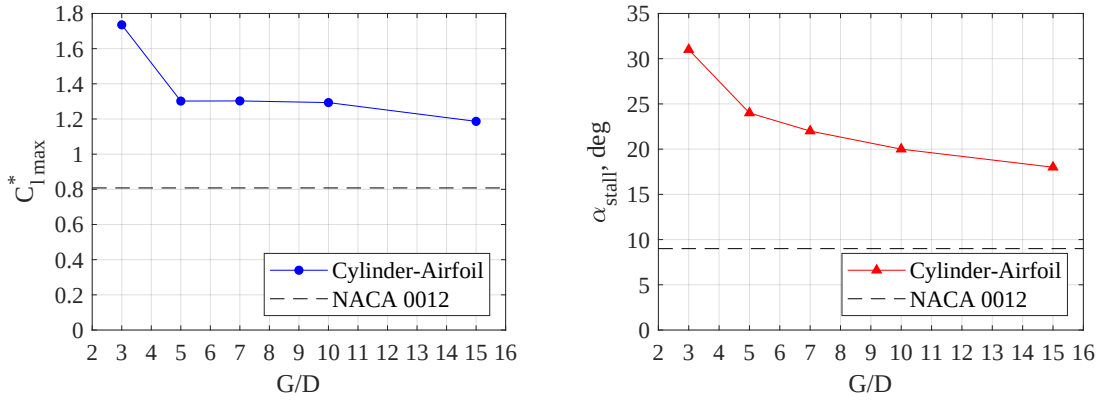

(a) Maximum lift coefficient

(b) Stall angle

Figure 5.11: Effect of the gap distance parameter on the lift enhancement and stall angle.

In addition, the airfoil stall delays to large angles of attack when encountering the cylinder wake. Figure 5.11(b) displays the evolution of stall angle versus the gap distance. At $G/D = 3$, airfoil stall occurs at $\alpha = 31°$ resulting in a delay of 22° compared to the isolated stall angle of 9°. Increasing the gap distance reduces this stall angle to 18° for $G/D = 15$, although it remains twice as large as the isolated stall angle. This delay in stall appears when new flow structures, such as the LEV displayed in figure 5.8(d), are generated from the cylinder-airfoil interaction. As the influence of the cylinder wake on airfoil force production is inversely proportion to the gap distance, figure 5.10(a) shows the lift curve approaching the isolated curve for increasing G/D. Due to this weakening of the cylinder wake as the gap distance increases, the cylinder-airfoil interaction diminishes and lessens the LEV, lowering the stall angle.

The influence of gap distance variation on the modified drag coefficient is shown in figure 5.12(a). Here the minimum drag, which occurs at $\alpha = 0°$ for the NACA 0012, is compared to the isolated airfoil value. Drag decreases due to the interaction with the cylinder yielding negative values from $3 \leq G/D \leq 10$. At $G/D = 3$ the minimum drag coefficient is $C^*_{d,min}$ = -0.075. Only as the gap distance rises to $G/D = 15$ does the minimum drag increase to positive values ($C^*_{d,min} = 0.007$), yet drag remains lower when compared to the isolated airfoil ($C_{d,min} = 0.012$). The significant reduction in drag ensues from the LEV's induced velocity field on the airfoil's surface, and this is further explained in chapter 6. As the LEV structure depends on the cylinder-airfoil interaction, increasing the gap distance will lessen the influence of the LEV on the drag reduction. However, as the vortex characterization in chapter 6 is only performed for $G/D = 3$, it can only be hypothesized that the decreasing wake-airfoil interaction lowers the influence of the LEV on airfoil drag at larger gap distances.

Figure 5.12(b) quantifies the angle of attack at which the modified drag coefficient crosses zero, providing the range of α where drag is negative. For a gap distance of $G/D = 3$, this range of α is maximum with the zero drag coefficient appearing at $\alpha = 7.5°$; whereas with increasing gap distance negative drag is present for a decreasing range of angles. At $G/D = 10$, this range is limited to $\alpha = 4.7°$. These results show that negative drag in the cylinder-airfoil configuration only exists for low angles of attack ($\alpha < 8°$) before positive drag resumes.

The aerodynamic performance of the NACA 0012 airfoil in the wake of a cylinder strongly depends on the gap distance. Wake flow structures shedding from

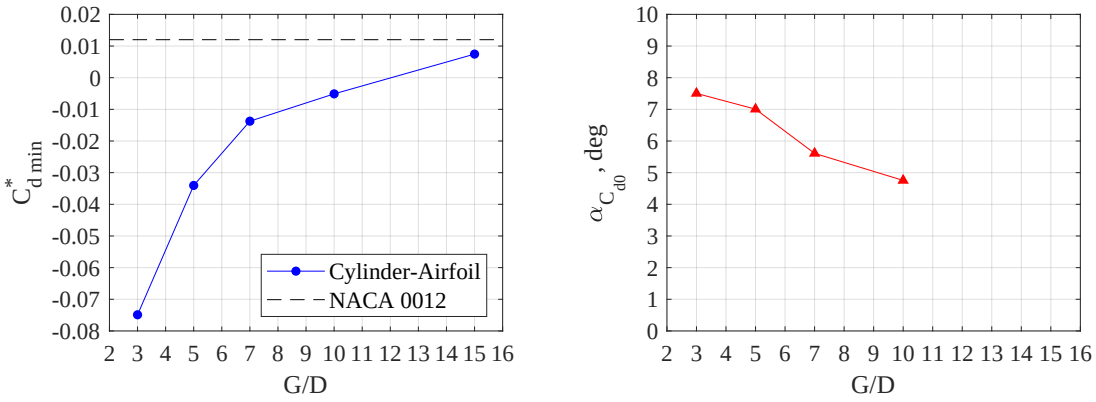

(a) Minimum drag coefficient

(b) Angle of attack when $C_d = 0$

Figure 5.12: Effect of the gap distance parameter on the minimum drag coefficient and the angle of attack for corresponding to zero drag.

the cylinder wake interact with the airfoil to enhance lift, delay stall, and generate negative drag. These effects are pronounced at smaller gap distances, but diminish as G/D increases due to the weakening cylinder wake approaching the airfoil.

5.2.4 Unsteady Airloads

Results up to this point have quantified the change in time-averaged airfoil performance downstream of a cylinder wake. However, the unsteady airfoil response to the turbulent inflow has not yet been investigated. The following results will investigate the amplitude of fluctuations and the frequency response of the airfoil when varying the gap distance parameter.

5.2.4.1 Amplitude of Fluctuations

Figure 5.13 shows the evolution of airfoil force fluctuations for lift, drag, and pitching moment coefficients as the gap distance increases. Results are presented at

select angles of attack $\alpha = \{0°, 10°, 20°, 30°, 40°\}$. The same trends exist for all force coefficients; the amplitude of fluctuations is maximum at the smallest gap distance $G/D = 3$ and decreases with increasing gap distance. For comparison, only the fluctuation levels for $\alpha = 0°$ of the isolated airfoil are shown by the blue dashed curve. At zero pitch angle, the fluctuations in the cylinder-airfoil configuration approaches the isolated value at $G/D = 15$, yet remain larger. This indicates that the airfoil's proximity to the cylinder's wake amplifies airload unsteadiness.

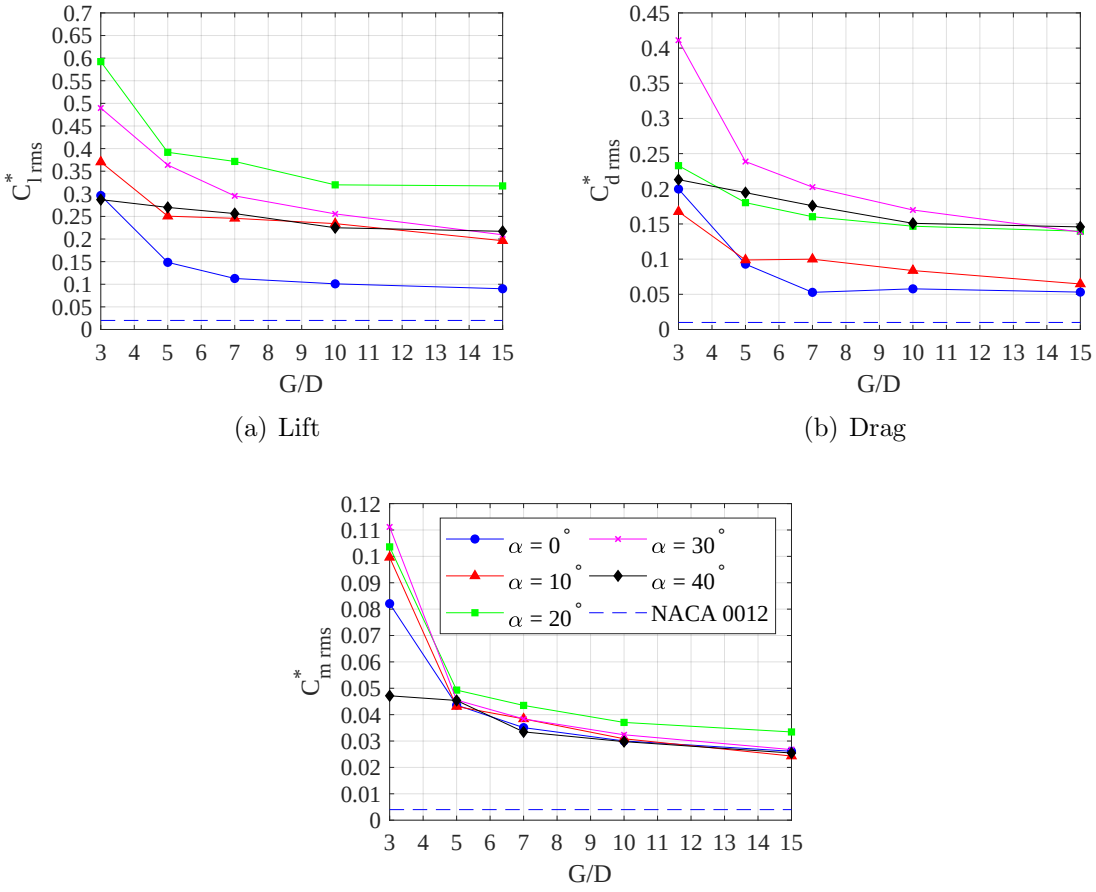

(a) Lift

(b) Drag

(c) Pitching moment

Figure 5.13: Influence of the gap distance parameter on the amplitude of force fluctuations.

The amplitude of fluctuations is also sensitive to variations in angle of attack.

Figure 5.13(a) shows lift fluctuations increase to a maximum from $C^*_{l,rms} = 0.3$ to 0.59 as the angle of attack increases to $\alpha = 20°$ when $G/D = 3$. Increasing the angle of attack further produces a reduction in lift fluctuations and at $\alpha = 40°$ the amplitude is comparable to zero pitch angle case. Drag and pitching moment fluctuations behave similarly at $G/D = 3$, although the maximum amplitude occurs at $\alpha = 30°$, and the pitching moment fluctuations are less susceptible to variations in α. Results from this figure clearly show that the unsteady cylinder wake provokes large amplitude fluctuations in the airfoil aerodynamics.

5.2.4.2 Airfoil Frequency Response

Displaying the airfoil's frequency response in the cylinder wake, figure 5.14 presents the Strouhal number for two different sets of scaling parameters. The first Strouhal number scaling is based on cylinder parameters such that

$$\mathrm{St}_D = \frac{f\ D}{U_\infty} \tag{5.4}$$

uses the cylinder diameter D and the freestream velocity U_∞ as the characteristic length and velocity, respectively. Since the cylinder wake is characterized by vortex shedding and acts as the inflow to the airfoil, employing equation 5.4 provides a direct comparison of the airfoil's frequency response to the inflow frequency. The second Strouhal number scaling uses

$$\mathrm{St}_c = \frac{f\ h}{\overline{u}_{wake}} \tag{5.5}$$

where the wake velocity at G/D defines the characteristic velocity and the projection of the airfoil's height in the streamwise direction is the characteristic length such that $h = c\sin(\alpha)$ for $\alpha \geq 7°$. If the angle of attack is less than 7°, then h corresponds to the airfoil thickness.

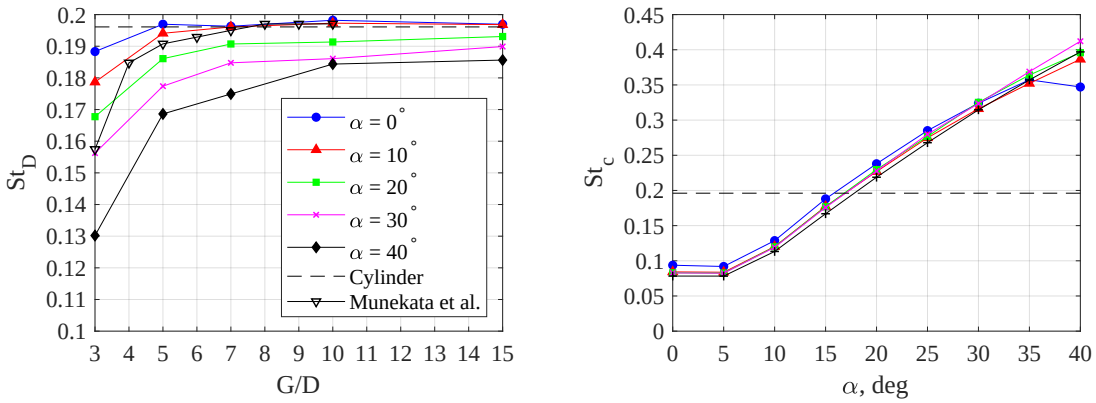

(a) St based on cylinder flow scaling

(b) St based on airfoil flow scaling

Figure 5.14: Influence of the gap distance parameter on the Strouhal number for the unsteady airfoil response.

Figure 5.14(a) shows the evolution of St_D with increasing gap distance for select angles of attack. At $\alpha = 0°$, the non-dimensional frequency of the airfoil forces is $\mathrm{St}_D = 0.188$ at $G/D = 3$ which is in good agreement with the cylinder vortex shedding frequency found in the literature $0.18 \leq \mathrm{St} \leq 0.21$ [34–36] and agrees well with the measured isolated cylinder frequency response of 0.196. This implies that the airfoil's response at $\alpha = 0°$ corresponds to the cylinder vortex shedding frequency. Increasing the gap distance improves the agreement as the Strouhal number increases to $\mathrm{St}_D = 0.197$, which is in excellent agreement with the cylinder wake frequency. Thus at large gap distances, the airfoil's frequency response matches with the isolated cylinder vortex shedding frequency.

For comparison, figure 5.14(a) also shows the evolution of St_D obtained from Munekata et al. [65] (upside-down triangular marker) for a cylinder-airfoil configuration with $D/c = 0.1$ and $\alpha = 0°$. Although the Strouhal number is significantly lower at $G/D = 3$, the overall trend agrees well with data from the current work. Munekata et al. [65] state that the close proximity of the airfoil increases the pressure on the downstream side of the cylinder. Jiang et al. [67] confirmed this pressure increase is due to the presence of the airfoil, indicating that the downstream airfoil influences the upstream cylinder vortex shedding. As the pressure on the cylinder's backside increases, this alters the separating shear layers and causes the vortex shedding frequency to decrease [65]. Consequently, the frequency of the inflow to the airfoil reduces and this results in a decline in the frequency of the airfoil's fluctuating forces. This shows that the airfoil's frequency response directly relates to the upstream wake frequency.

For larger angles of attack, the Strouhal number of airfoil airloads strongly decreases for small gap distances. At $G/D = 3$, the St_D reduces from 0.188 to 0.130 as the pitch angle increases from 0° to 40°, while St_D decreases to only 0.186 for $G/D = 15$. This reveals that the airfoil's frequency response is exceedingly dependent on α for small gap distances and is insensitive for $G/D \geq 10$. Since the wake frequency of an isolated cylinder is known to be periodic and unchanging for a constant freestream flow, these modifications in the airfoil frequency response result from a change in the cylinder-airfoil interaction due to pitch angle. As the presence of the airfoil in the cylinder-airfoil configuration raises the surface pressure on the cylinder [65, 67], increasing the angle of attack will amplify this pressure

augmentation due to a larger airfoil blockage effect [66]. This results in a strong decrease in the Strouhal number of the cylinder vortex shedding and by extension the airfoil's frequency response.

To summarize, the airfoil's frequency response synchronizes with the upstream wake frequency, but this frequency depends on the airfoil's influence on the upstream cylinder wake. For small α and large G/D, the downstream airfoil does not influence the upstream cylinder, thus the frequency corresponds to the isolated cylinder vortex shedding. In contrast, for large α and small G/D, the downstream airfoil influences the incoming wake frequency by decreasing the upstream cylinder vortex shedding frequency, therefore lowering the airfoil's frequency response.

Figure 5.14(b) shows the airfoil Strouhal number using airfoil scaling parameters. In this figure, St_c does not asymptote to the cylinder vortex shedding frequency, instead the airfoil's frequency response increases linearly with values ranging from $\mathrm{St}_c = 0.09$ to 0.40 for $\alpha = 5^\circ$ to 40°. Variations from the gap distance disappear as all G/D curves collapse into one trend. This demonstrates that the wake velocity and the projected airfoil height constitute the appropriate scaling for the cylinder-airfoil flow. Using these scaling parameters removes the effect of the gap distance on the airfoil frequency response. As a consequence, the wake velocity $\overline{u}_{wake}$ no longer influences the airfoil's frequency response and variations in St_c solely depend on the pitch angle α. Unfortunately, this does not inform how the airfoil frequency response relates to the cylinder vortex shedding frequency; and thus the Strouhal number based on cylinder scaling is preferred to study the effect of a cylinder wake on unsteady airfoil force production.

Depending on the choice of scaling parameters, the airfoil's frequency response either asymptotes to the isolated cylinder vortex shedding frequency with increasing gap distance (see figure 5.14(a)), or collapses to one trend that increases linearly with angle of attack (see figure 5.14(b)). In order to advance our understanding of the effect of a cylinder wake interacting with an airfoil, the Strouhal number based on the cylinder scaling, illustrated in figure 5.14(a), is decidedly more informative. In this figure, results for low angles of attack ($\alpha \leq 10°$) and moderate gap distances ($G/D \geq 5$) show the unsteady airloads measured on the airfoil fluctuate approximately at the isolated cylinder vortex shedding frequency. This does not come as a surprise since the flow characterization in chapter 4 identified the cylinder vortex shedding frequency as the inflow to the airfoil. Increasing the angle of attack in figure 5.14(a) reveals that the airfoil decreases the incoming wake frequency at low gap distances, G/D.

the upstream wake frequency as it reduces with increasing α at low gap distances.

5.3 Effects of Varying Cylinder Diameter

Variations of the cylinder diameter while the airfoil chord is kept constant will affect airfoil performance due to changes in the cylinder wake. Thus, this section investigates the effect of three cylinder diameters with the following cylinder-diameter-to-airfoil-chord ratios of $D/c = \{0.36, 0.69, 1.04\}$. In the following cylinder-airfoil configuration, the gap distance remains constant at $G/D = 3$ and no offset exists

between the cylinder and the airfoil's quarter chord. Figure 5.15 sketches the resulting configuration and shows that the physical spacing between the cylinder and airfoil must increase to keep the gap distance constant.

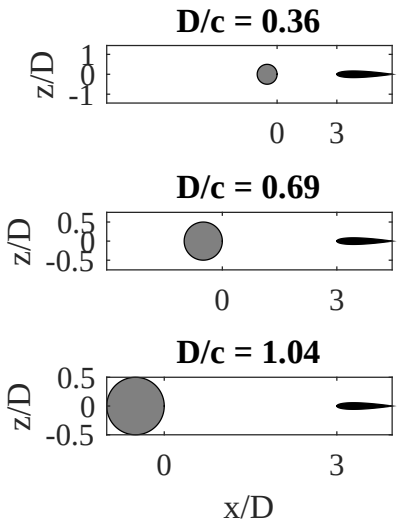

Figure 5.15: Sketch illustrating the cylinder-airfoil configuration for varying cylinder diameter with a constant gap distance, $G/D = 3$.

5.3.1 Time-Averaged Aerodynamics

Figure 5.16 presents the airfoil time-averaged lift, drag, and pitching moment coefficients for increasing the cylinder diameter. Each force coefficient is corrected for the low fluid momentum in the cylinder wake by referencing the local wake velocity. Overall, the force trends remain similar to the results presented for the gap distance parameter in figure 5.10.

A closer examination of the modified lift coefficient C_l^* in figure 5.16(a) shows no significant influence of increasing the cylinder diameter at low angles of attack. The lift curve slope is identical as D/c increases from 0.36 to 1.04 and agrees well

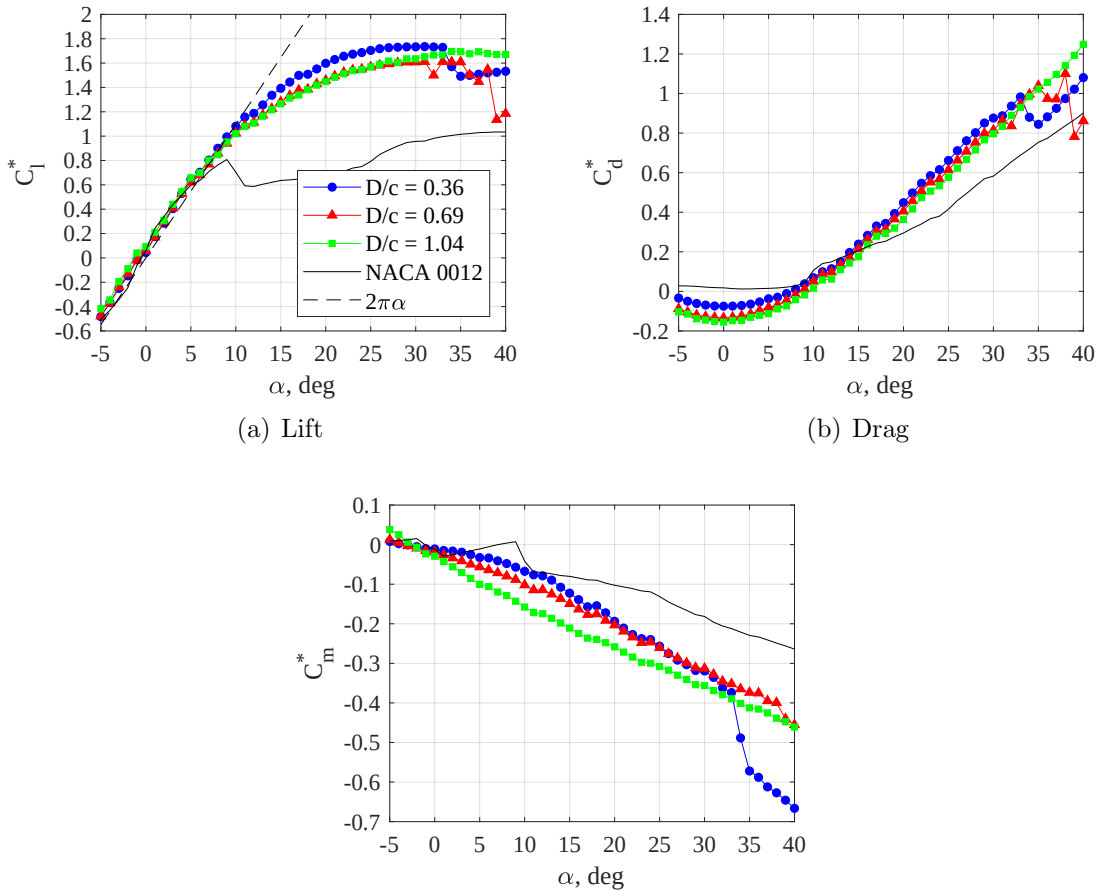

(a) Lift

(b) Drag

(c) Pitching moment

Figure 5.16: Influence of the cylinder diameter (D/c) on the airfoil's time-averaged force coefficients for $-5° \leq \alpha \leq 40°$ at $\mathrm{Re}_c = 1 \times 10^5$.

with the theoretical slope of 2π until $\alpha = 10°$. For larger angles of attack ($\alpha > 10°$), the lift curve slope decreases and reaches a maximum lift value at a large angle of attack. Table 5.2 compares $C^*_{l,max}$ and corresponding stall angle for variations of the cylinder diameter D/c. Increasing the cylinder diameter leads to a reduction in the maximum lift coefficient to values of $C^*_{l,max} = 1.61$ and 1.70 for $D/c = 0.69$ and 1.04, respectively. Although the lift reduction for $D/c = 1.04$ may not be meaningful as it is within the uncertainty error for lift measurements. This is not the case for $D/c = 0.69$ as a local minimum in $C^*_{l,max}$ exists for the tested cylinder diameters.

In contrast, the stall angle increases slightly with increasing cylinder diameter from $\alpha = 31°$ to $34°$ as shown in table 5.2. For $D/c = 0.36$ and 0.69, an abrupt decrease in lift at $\alpha = 35°$ (see figure 5.16(a)) was previously identified as the aerodynamic coupling between the cylinder and airfoil. This coupling phenomenon occurs at $\alpha = 39°$ for a cylinder diameter of $D/c = 0.69$ and is absent when $D/c = 1.04$ for the tested range of α. Aerodynamic coupling between the cylinder and airfoil is sensitive to the cylinder diameter and increasing the diameter delays this phenomenon to larger incidence angles.

Table 5.2: Variations in maximum lift, stall angle, and minimum drag due to increasing cylinder diameter, D/c.

D/c	$C^*_{l,max}$	α_{stall}, deg	$C^*_{d,min}$
0.36	1.74	31	-0.07
0.69	1.61	33	-0.13
1.04	1.70	34	-0.16

The modified drag coefficient C^*_D in figure 5.16(b) is not strongly influenced by the increasing cylinder diameter, as the drag decreases by less than 8 % on average. Only at low angles of attack ($\alpha < 10°$) does a noticeable decrease in drag emerge with increasing D/c. Table 5.2 reports the evolution of minimum drag ($\alpha = 0°$) as a function of D/c. Regardless of the cylinder diameter, the presence of the cylinder creates negative drag on the airfoil. As the cylinder diameter increases from $D/c = 0.36$ to 1.04, the minimum drag decreases from $C^*_{d,min}$ = -0.07 to $C^*_{d,min}$ = -0.16. This clearly shows the cylinder diameter has a strong effect on the drag coefficient at low angles of attack.

Variations in the pitching moment coefficient are shown in figure 5.16(c). Over-

all, no major differences occur between $D/c = 0.36$ and $D/c = 0.69$ and the sudden discrepancy at $\alpha = 35°$ relates to the aerodynamic coupling. At $D/c = 1.04$, the pitching moment curve is no longer near zero for $\alpha \leq 5°$, instead C_m^* decreases linearly with increasing pitch angle. This results in an increase in the absolute value of the moment coefficient.

As the cylinder diameter changes significantly, the time-averaged airfoil performance retains the same trend over the tested range of $D/c = 0.39$ to 1.04 with the following discrepancies. Lift experiences a reduction of approximately 8 % for $\alpha \geq 15°$ and interestingly this decrease is identical for both $D/c = 0.69$ and 1.04. Drag and pitching moment exhibit a small, yet noticeable decrease with increasing cylinder diameter D/c over most angles of attack. Except for lift, the effect of increasing the cylinder diameter in the cylinder-airfoil configuration is to decrease drag and the pitching moment.

5.3.2 Flowfields

As the previous analysis showed, the cylinder diameter is not as significant as the gap distance in modifying airfoil forces. A visualization of the cylinder-airfoil flowfield will aid in understanding the impact of increasing the cylinder diameter. Figure 5.17 compares an experimental smoke flow visualization for $D/c = 0.36$ (figure 5.17(a)) with vorticity contours for $D/c = 1.04$ (see figure 5.17(b)) obtained from CFD (A. Grubb, private communication, July, 2020), and both flowfields are presented to scale.

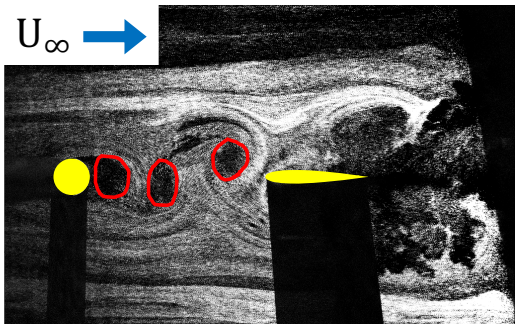

(a) Smoke flow for $D/c = 0.36$ at $G/D = 5$

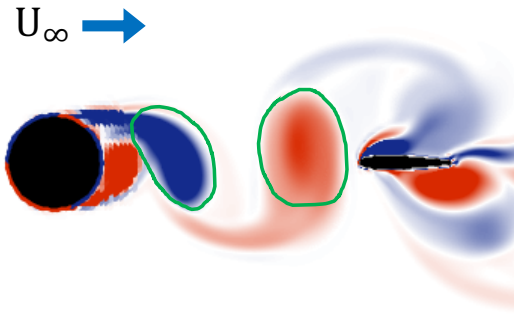

(b) CFD vorticiy field for $D/c = 1.04$ at $G/D = 3$ (A. Grubb, private communication, July 2020)

Figure 5.17: Comparison of the cylinder-airfoil wake flow structures for increasing cylinder diameter.

In both cases, the gap distance between the bodies is greater than the critical value as cylinder vortex shedding is present. From the smoke visualization in figure 5.17(a), vortices shed from the cylinder are qualitatively represented by the regions void of smoke particles and these are highlighted with red contours. In the vorticity fields from CFD simulations (see figure 5.17(b)), these vortices are qualitatively expressed by the intensity of the vorticity contour, and green contours were added to facilitate their visualization. The cylinder diameter clearly affects the size of vortices in the cylinder near wake, as the red contours are comparable to the small cylinder diameter and remain significantly smaller than the airfoil chord. In contrast, the green contours agree with the larger cylinder diameter and these structures are nearly identical in size to the airfoil chord. Depending on the cylinder diameter D/c, vortices with different size populate the inflow to the airfoil, resulting in a wake-airfoil interaction with increasing vortex core diameter as D/c increases. Although the size of vortices increases significantly with D/c, the organization of the cylinder

wake remains independent of its diameter. This explains why the time-averaged force coefficients retain a similar trend for variations in D/c, but it is reasonable to believe the cylinder diameter will affect the unsteadiness of the airloads.

5.3.3 Unsteady Airloads

As the above flow visualization illustrates, varying the cylinder diameter alters the size of flow structures in the cylinder-airfoil flow. Yet, the time-averaged airfoil force trends are similar as D/c varies, suggesting that the vortex size effect averages out. Thus, the effect on unsteady forces will now be investigated.

5.3.3.1 Amplitude of Fluctuations

The influence of cylinder diameter on the amplitude of fluctuations for lift, drag, and pitching moment coefficients is presented in figure 5.18. Starting with the case for lift fluctuations (see figure 5.18(a)), the rms is plotted versus the cylinder-diameter-to-airfoil-chord ratio for five selected angles of attack. Increasing from a small diameter ($D/c = 0.36$) to a moderate diameter ($D/c = 0.69$) presents a minor growth in the lift amplitude, while $C_{l,rms}$ remains less than 1. At the largest cylinder diameter $D/c = 1.04$, the amplitude in lift fluctuations rise significantly with $C_{l,rms} > 2$. Increasing the angle of attack varies the amplitude in lift fluctuations for all gap distances, although this effect is strongest for $D/c = 1.04$ as $C_{l,rms}$ grows by 0.90 when α is pitched from 0° to 30°.

Fluctuations of the drag coefficient shares a similar trend as discussed for the

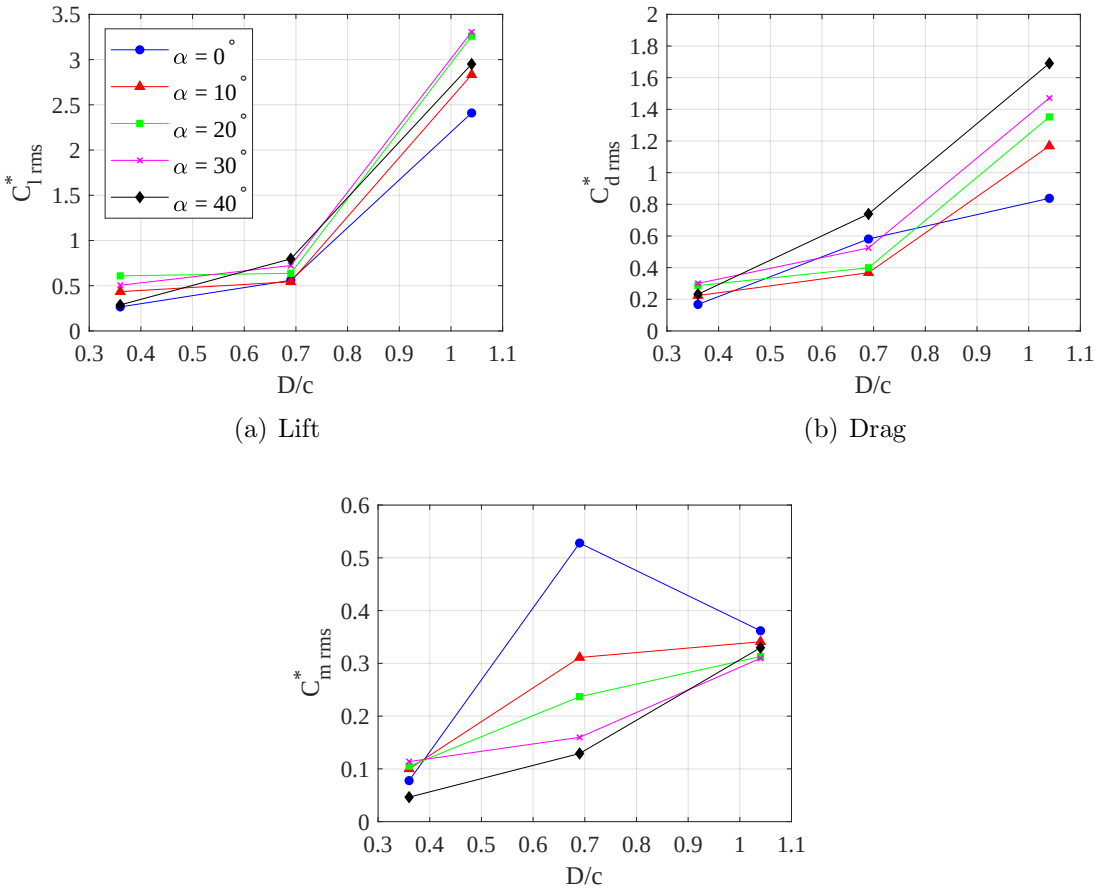

(a) Lift

(b) Drag

(c) Pitching moment

Figure 5.18: Effect of the cylinder diameter on the amplitude of the NACA 0012 force fluctuations.

lift case (see figure 5.18(b)). The amplitude of fluctuations is lowest at $D/c = 0.36$ with minimal variations due to the pitch angle, and increases with the largest cylinder diameter $D/c = 1.04$. For the large cylinder, the effect of angle of attack becomes significant as fluctuations increase from 0.84 to 1.69 over the entire range of α. However, figure 5.18(c) shows the fluctuations for the pitching moment follow a distinctly different trend. For $\alpha = 0°$, fluctuations increase from 0.08 at $D/c = 0.36$ to 0.53 for $D/c = 0.69$ and then decreases to 0.36 at the largest diameter. Furthermore, the angle of attack greatly affects the level of fluctuations

at $D/c = 0.69$ as the amplitude of $C_{m,rms}$ decreases to 0.13 at $\alpha = 40°$, while the amplitude remains nearly constant for both $D/c = 0.36$ and 1.04. This suggests that an optimal cylinder diameter exists for augmenting pitching moment coefficient during cylinder-airfoil interactions at low angles of attack, and this could originate from a resonance phenomenon. However, this peak in amplitude fluctuations is not observed in lift or drag results. No conclusive explanation is provided in this thesis and it is recommended that future studies further investigate this anomaly.

As these results illustrate the effect of the cylinder diameter increasing airfoil force fluctuations, the flow visualization from figure 5.17 provides the explanation. Increasing the cylinder diameter generates larger vortices in the wake upstream of the airfoil. These larger structures correspond to intense flow perturbations, which amplifies aerodynamic fluctuations in the wake-airfoil interaction.

5.3.3.2 Airfoil Frequency Response

Previous results demonstrated the amplitude of airload fluctuations is related to the cylinder diameter. Here, the development of the airfoil frequency response is associated with the cylinder diameter D/c as illustrated in figure 5.19. The Strouhal number of the airfoil airloads is plotted versus the cylinder diameter for increasing pitch angles. In all cases, the Strouhal number increases with cylinder diameter D/c as it converges to the isolated cylinder vortex shedding frequency (black dashed line). This occurs because the influence of the airfoil on the cylinder's wake decreases with increasing cylinder diameter. At zero angle of attack, the airfoil

frequency response reduces when downstream of the small cylinder, $\mathrm{St}_D = 0.188$, as opposed to an excellent agreement as the cylinder diameter increases to $D/c = 1.04$. For zero angle of attack, the cylinder wake determines the airfoil response frequency independently of the cylinder diameter.

Similar to the explanation provided in section 5.2.4.2, increasing the angle of attack reduces the Strouhal number regardless of the cylinder diameter. Although, this effect is strongest for $D/c = 0.36$ and weakens as the cylinder diameter increases. The relative size between the cylinder diameter and airfoil chord dictates the influence of the airfoil's blockage effect on the cylinder's surface pressure. At $D/c = 0.36$, the airfoil's blockage affects a larger portion of the cylinder, effectively reducing the St_D as the angle of attack rises. For $D/c = 1.04$, the airfoil's influence on the upstream cylinder wake diminishes, thus the airfoil's frequency response mostly agrees with the isolated cylinder vortex shedding frequency.

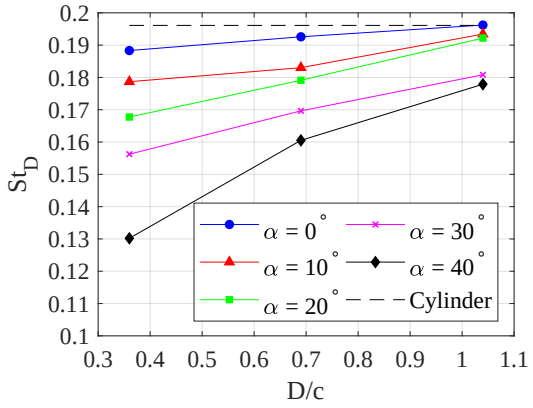

Figure 5.19: Effect of the airfoil's frequency response due to variations in the cylinder's diameter.

The frequency response of the airfoil's airloads is sensitive to the cylinder-diameter-to-airfoil-chord ratio since the cylinder wake is the inflow to the airfoil.

For large D/c, the airfoil frequency response is dictated by the cylinder wake up to $\alpha = 20°$. At a smaller cylinder diameter, the airfoil's pitch angle influences the upstream cylinder wake, causing a decrease in the airload frequency.

5.4 Effects of Varying Offset Distance

The following section examines the influence of the offset distance, z/D, between the cylinder and airfoil. An offset distance is defined as a non-zero transverse distance from the cylinder's centerline ($z/D = 0$) to the location of the airfoil's quarter-chord. Figure 5.20 shows the relative position of the airfoil pitched at $\alpha = 30°$ for all tested offset distances. A total of six offset distances are investigated, $z/D = \{-0.75, -0.5, -0.25, 0.25, 0.5, 0.75\}$, and they are compared to the non-offset case ($z/D = 0$). For all permutations in this section, the cylinder-diameter-to-airfoil-chord ratio was $D/c = 0.69$ and the gap distance was fixed at $G/D = 3$.

5.4.1 Time-Averaged Aerodynamics

Looking at the influence of varying the offset distance z/D on airfoil performance, figure 5.21 shows the time-averaged lift, drag, and pitching moment coefficients. Normalizing the force coefficients with the freestream velocity U_∞ is sufficient here as the relative change due to z/D is the focus of this section. Overall, the three force coefficients display similar trends as those observed in figure 5.7 with a few discrepancies.

For all tested offset distances, the lift coefficient (see figure 5.21(a)) exhibits

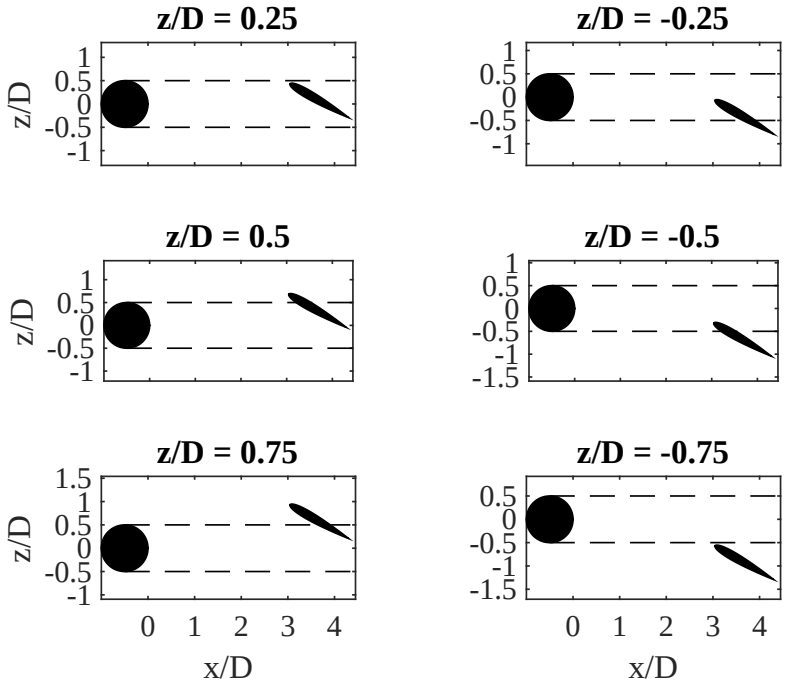

Figure 5.20: Sketch illustrating all offset distance (z/D) configurations between the cylinder and airfoil with $\alpha = 30°$ when $D/c = 0.69$ and $G/D = 3$.

a reduction in each lift curve slope for $\alpha \leq 10°$ depending on z/D. This decreasing effect correlates with the absolute value of the offset distance and becomes more prominent for small $|z/D|$. At $\alpha = 10°$, the lift coefficient is $C_l = 0.59$ for $z/D = -0.75$ and decreases to $C_l = 0.43$ for $z/D = -0.25$. Furthermore, the sign of the offset distance also affects the lift coefficient, with positive z/D reducing C_l compared to negative offset distances. This is easily visible for angles of attack larger than $\alpha = 30°$. In addition, the offset distance also modifies the airfoil stall angle and behavior. At negative z/D, the stall angle is approximately 35° and decreases to $\alpha = 26°$ for positive z/D. Across all offset distances, stall continues to be characterized by a gradual decrease in lift unlike the abrupt drop for the isolated airfoil.

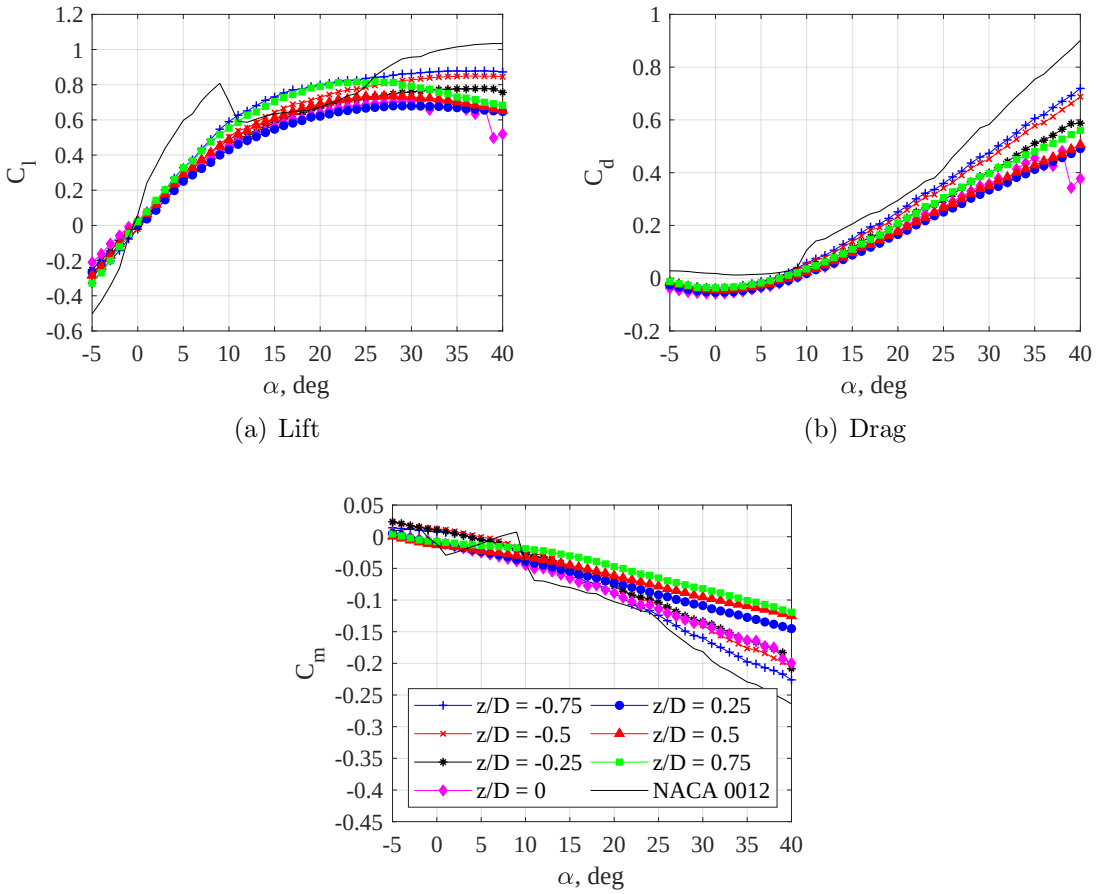

(a) Lift

(b) Drag

(c) Pitching moment

Figure 5.21: Influence of the offset distance parameter (z/D) on time-averaged force coefficients for $-5° \leq \alpha \leq 40°$ at $\mathrm{Re}_c = 1 \times 10^5$.

The drag coefficient (see figure 5.21(b)) presents little modifications at low angles of attack. For $\alpha \leq 10°$, increasing the magnitude of the offset distance $|z/D|$ causes drag to grow, but C_d continues to remain negative for $\alpha \leq 5°$ for the tested parameters. At larger angles of attack ($\alpha > 10°$), the drag coefficient increases smoothly without any abrupt changes in C_d except for $z/D = 0$ at $\alpha = 38°$. Positive offset distances produce a more substantial reduction in C_d compared to negative z/D, showing that offset distances provide an asymmetrical effect at large angles of attack. In a similar fashion, the pitching moment coefficient (see figure 5.21(c))

varies significantly at larger angles of attack depending on the offset distance. In this case, pitching moment decreases more for negative offset distances than positive ones, but for $\alpha \leq 10^{\circ}$ C_m for the isolated airfoil remains the largest in magnitude.

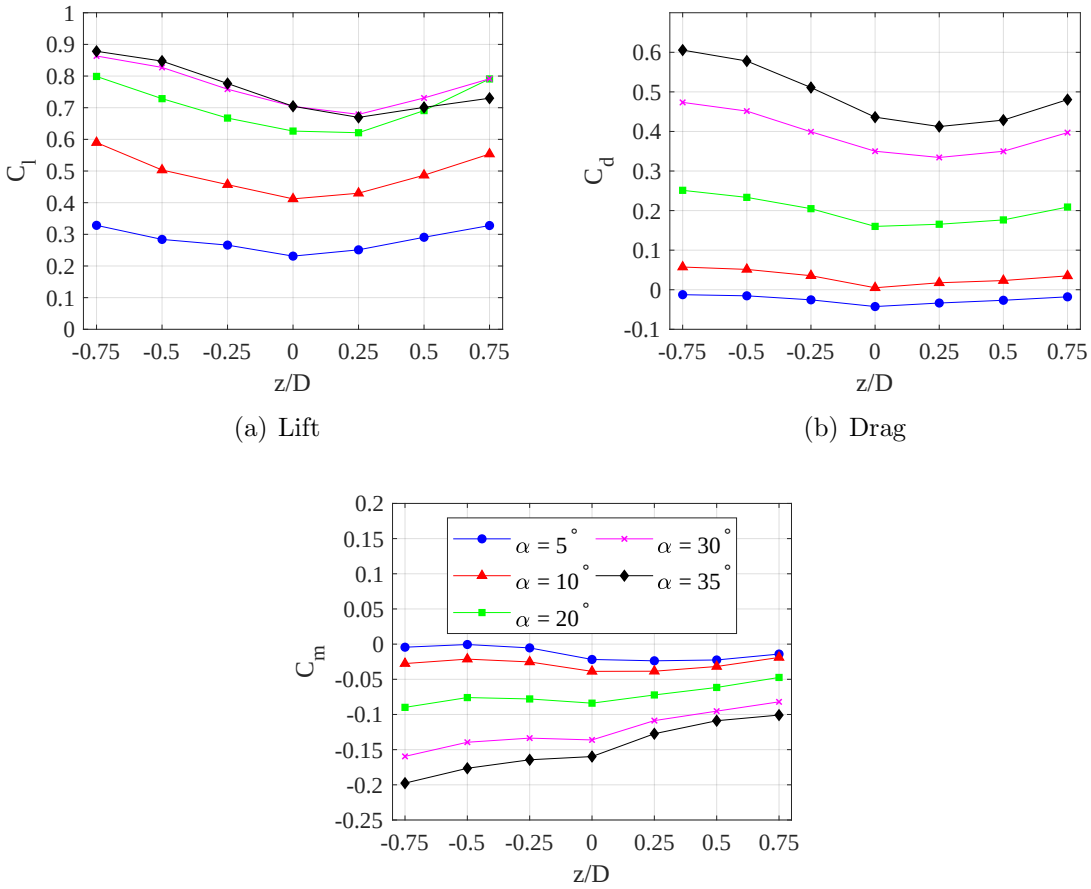

(a) Lift

(b) Drag

(c) Pitching moment

Figure 5.22: Effect of the offset distance parameter on time-averaged force coefficients at select angles of attack.

A closer examination of these results reveal hidden trends in the force data. Figure 5.22 shows C_l, C_d, and C_m plotted as a function of the offset distance for the following angles of attack, $\alpha = \{5^{\circ}, 10^{\circ}, 20^{\circ}, 30^{\circ}, 35^{\circ}\}$. For $\alpha \leq 10^{\circ}$, the lift coefficient (see figure 5.22(a)) is nearly symmetrical for both positive and negative z/D, with a minimum C_l occurring at zero offset ($z/D = 0$). This indicates that at

low angles of attack, varying the offset distance results in a symmetrical lift force production for both positive and negative z/D. However, asymmetries in the lift develop due to the offset distance when pitching the airfoil to angles of attack $\geq 20°$. In the tested range, C_l is maximum at $z/D = -0.75$ with a value of $C_l = 0.88$ and a minimum of $C_l = 0.67$ occurs at $z/D = 0.25$ when $\alpha = 35°$. This illustrates that the lift coefficient is sensitive to the offset distance for large angles of attack and varies up to $\Delta C_l = 0.21$ in the current experiments.

A similar trend is observed for the drag coefficient as seen in figure 5.22(b). At $\alpha = 0°$, drag is symmetrical for all tested z/D with the minimum again occuring for zero offset ($z/D = 0$). Asymmetries begin to develop as the angle of attack increases to $\alpha = 20°$, but the minimum continues to appear at $z/D = 0$. Only when the angle of attack reaches at least $\alpha = 30°$ does the asymmetry in the drag coefficient resemble the C_l case. For the tested offset distances, C_d is maximum at $z/D = -0.75$ with a value of 0.60 and a minimum exists at $z/D = 0.25$ with $C_d = 0.41$ when $\alpha = 35°$. Similar to the lift trend, the drag coefficient is reliant on the offset distance between the cylinder and airfoil, with a maximum difference of $\Delta C_d = 0.19$ identified.

The pitching moment coefficient behavior differs from C_l and C_d as shown in figure 5.22(c). At low angles of attack ($\alpha \leq 10°$), C_m varies little with the offset distance, but a minimum and maximum establish at $z/D = 0.25$ and -0.5, respectively. Increasing the angle of attack up to $\alpha = 35°$ shows a significant change in the evolution of C_m from variations in the offset distance. The pitching moment coefficient is $C_m = -0.20$ at $z/D = -0.75$ and increases in a nearly linear fashion

to $C_m = -0.10$ at $z/D = 0.75$ for $\alpha = 35°$. Results from varying the offset distance parameter show that the relative positioning of the cylinder and airfoil plays a critical role in time-averaged airfoil performance. The following section further investigates the effect of z/D on the maximum lift coefficient and the airfoil stall angle.

5.4.1.1 Maximum Lift and Stall Angle

Figure 5.23 shows how the offset distance z/D alters the maximum lift coefficient and the stall angle. In figure 5.23(a), the $C_{l,max}$ displays a minimum of 0.68 at $z/D = 0.25$ and a maximum of $C_{l,max} = 0.88$ at $z/D = -0.75$. These locations of maximum and minimum correspond to the same locations identified in figure 5.22(b), showing that the dependence on z/D also applies to the maximum lift coefficient. Comparing the maximum lift coefficient to the isolated airfoil case with a value of $C_{l,max} = 0.81$ shows that the maximum lift coefficient is lower for offset distances ranging from $z/D = -0.25$ to 0.5 in the cylinder-airfoil configuration. Only for $z/D \leq -0.5$ does the offset distance produces a larger $C_{l,max}$.

Unlike the lift coefficient, the stall angle is not affected the same by variations in the offset distance. Rather than continuously evolving, the stall angle is nearly independent as the absolute value of z/D increases. For $z/D < 0$, the stall angle is further delayed to $\alpha = 35°$ to $36°$ compared to $33°$ from the zero offset case ($z/D = 0$). Positive offset distances reduce the stall angle of attack to approximately $25°$, although this remains significantly larger than the isolated stall angle of $\alpha = 9°$. In the cylinder-airfoil configuration, the stall angle depends on the offset distance

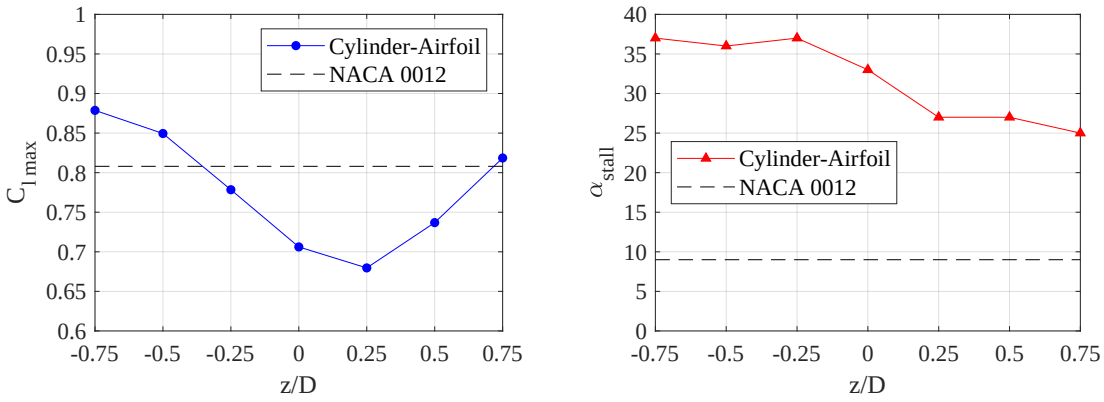

(a) Maximum lift coefficient

(b) Stall angle

Figure 5.23: Effect of the offset distance parameter on the maximum lift coefficient and stall angle.

with the maximum stall angle occurring for negative z/D and a lower stall angle exists for positive z/D. Changing from a negative to a positive offset distance decreases the stall angle by approximately 10°.

In summary, results from figures 5.22 and 5.23 clearly demonstrate the influence of the offset distance in the cylinder-airfoil configuration on airfoil performance. Generally, negative offsets increase lift, drag, and stall angle, while a minimum of these values occurs at $z/D = 0.25$. The relative position between the airfoil and incoming cylinder wake affects wake-airfoil interactions, resulting in different wake structures which are responsible for the changes in time-averaged airfoil performance described in this section.

5.4.2 Flowfields

To understand how flow structures in the cylinder wake change with the offset distance, results from smoke flow visualization are presented in figure 5.24. Since C_l

and C_d are minimum for $z/D = 0.25$ (left column) and maximum for z/D = -0.75 (right column), only these two offset distances are displayed.

Starting with $\alpha = 0°$ and $z/D = 0.25$, figure 5.24(a) shows two vortices in the cylinder near wake. A clockwise vortex (CW1) forms at the cylinder's upper surface, while a counterclockwise vortex (CCW1) sheds from the lower cylinder surface. At this offset distance, the airfoil is aligned with vortices shedding from the cylinder wake, leading to a direct encounter between these structures and the airfoil's leading edge. This is shown by the collision of the clockwise vortex (CW2) resulting in a large deformation of the vortex structure due to the wake-airfoil interaction. This smoke flow visualization illustrates that the airfoil is completely immersed in the cylinder wake.

In figure 5.24(b), the airfoil offset distance is z/D = -0.75 which prevents the airfoil from directly encountering the cylinder wake. Both clockwise and counter-clockwise vortices shedding from the cylinder (CW1 and CCW1) advect over the airfoil. This is noticeable by the previously shed clockwise vortex CW2 directly above the airfoil which is not deformed, suggesting that clockwise vortices do not collide with the airfoil at this offset distance. For this flow configuration, the airfoil is located at the edge of the cylinder wake.

Differences in the flowfields between $z/D = 0.25$ and $z/D = -0.75$ show that the airfoil sees disparate inflow fluid momentum. At $z/D = 0.25$ shown by figure 5.24(a), the airfoil is fully immersed in the cylinder wake which is characterized by lower momentum fluid (see figure 5.9(a)). This results in the decrease in time-averaged lift and drag forces reported in figure 5.22. At z/D = -0.75, the converse

is true as the airfoil sees higher momentum fluid due to being offset from the wake centerline (see figure 5.9(a)), increasing airfoil force production as noted in figure 5.22. However, as the cylinder wake is highly unsteady and dominated by vortices, increasing the angle of attack will modify structures in the wake flow.

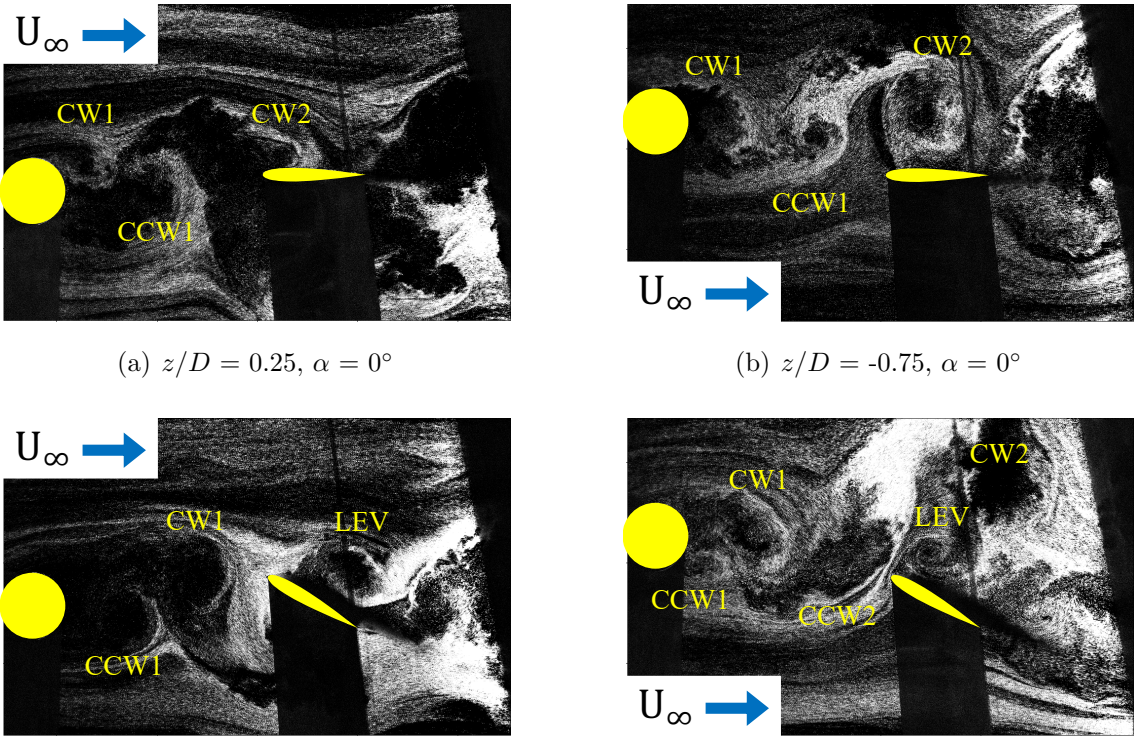

(a) $z/D = 0.25$, $\alpha = 0°$

(b) z/D = -0.75, $\alpha = 0°$

(c) $z/D = 0.25$, $\alpha = 30°$

(d) z/D = -0.75, $\alpha = 30°$

Figure 5.24: Smoke flow visualization showing the effect of the offset distance parameter on wake flow structures in the cylinder-airfoil configuration when $G/D = 3$.

As the airfoil is pitched to $\alpha = 30°$, the counterclockwise vortices (CCW) shed from the lower cylinder surface to interact with the airfoil's leading edge, forming a leading edge vortex (LEV). This appears for both offset distances, $z/D = 0.25$ and -0.75, on the suction side of the airfoil as shown in figures 5.24(c) and 5.24(d). The LEV structure was absent on the pressure side of the airfoil, thus the corresponding

smoke flow visualization are not shown.

For $z/D = 0.25$ (see figure 5.24(c)), the clockwise vortex (CW1) is at the same height as the LEV. This leads to an interaction between these two structures which will affect the development of the LEV [70, 113], thereby reducing lift. This lift reduction manifests as the minimum values measured in figure 5.22 when $\alpha \geq 20°$. For z/D = -0.75, only the counterclockwise vortices (CCW1 and CCW2) will interact with the airfoil's leading edge, as the clockwise vortices (CW1 and CW2) will advect downstream without colliding with the airfoil. This allows the LEV to form without interruption [70,113] and produces more lift as noted by the maximum values in figure 5.22.

Flow visualization provides evidence of different flow structures in the cylinder-airfoil wake which manifest as modifications in airfoil for production related to the offset distance. At $z/D = 0.25$, clockwise vortices interact with the airfoil and hinder the development of the LEV. In contrast, at z/D = -0.75 clockwise vortices do not collide with the airfoil since it is at the edge of the cylinder wake, enabling the LEV to further develop.

5.4.3 Unsteady Airloads

The offset distance parameter z/D alters the airfoil performance as the time-averaged coefficients in figures 5.21 and 5.22 show, yet the effect on the unsteady airfoil behavior remains unknown. First the amplitude of fluctuations is investigated, followed by the frequency response of the airfoil.

5.4.3.1 Amplitude of Fluctuations

Figure 5.25 shows the variation in amplitude of fluctuations for lift, drag, and pitching moment coefficients for $\alpha = 0°$ and 40°. At zero angle of attack, lift fluctuations are symmetrical as the offset distance varies. For $-0.5 \leq z/D \leq 0.5$, the amplitude of fluctuations in the lift coefficient is independent of the offset distance as $C_{l,rms}$ is approximately constant with a value of 0.24 over this range. Increasing the offset distance to $z/D = \pm 0.7$ shows a symmetrical decrease in the fluctuations to $C_{l,rms} = 0.20$. This reduction in fluctuations represents the airfoil moving to the edge of the cylinder wake and encountering a less turbulent inflow as illustrated in figure 5.24(b). Increasing the angle of attack to $\alpha = 40°$ causes the amplitude of fluctuations to vary with z/D and increase in magnitude. Over the range of $-0.75 \leq z/D \leq 0.75$, the lift amplitude is minimum at $z/D = -0.75$ with a value of $C_{l,rms} = 0.23$ and increases with increasing z/D to a maximum of 0.38 at $z/D = 0.25$.

Flow visualization from figure 5.24 provides an explanation for these values. At $z/D = 0.25$, the airfoil is fully immersed in the cylinder wake and aligned with the clockwise vortices shedding from the cylinder. This results in a direct collision between the wake and the airfoil which amplifies lift fluctuations. At z/D = -0.75 the smoke flow visualization shows that only the leading edge of the airfoil interacts with the cylinder wake. Hence at this offset distance, the wake-airfoil interaction is significantly reduced and this causes a decrease in the amplitude of lift fluctuations.

Drag follows a similar trend with a few notable differences. For $\alpha = 0°$ the

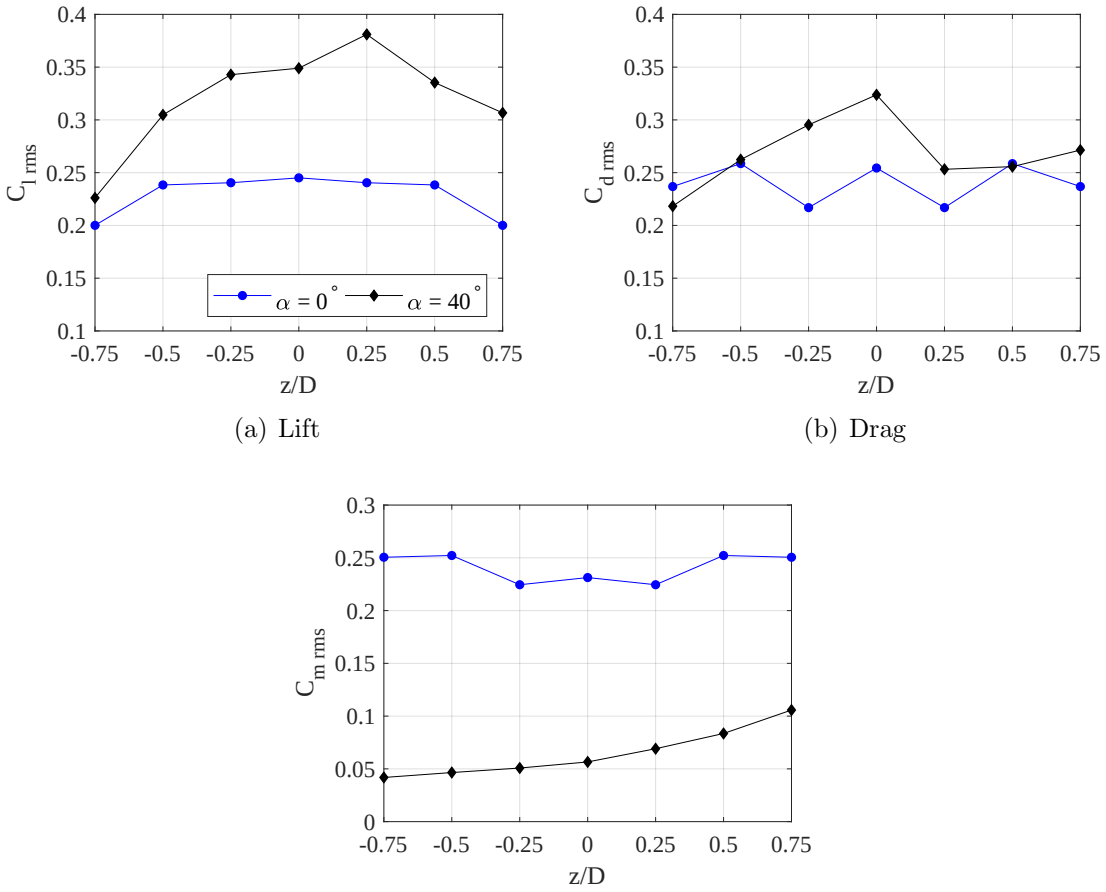

(a) Lift

(b) Drag

(c) Pitching moment

Figure 5.25: Effect of the cylinder-airfoil offset distance (z/D) on the amplitude of airfoil force fluctuations.

amplitude fluctuations of drag are symmetrical for positive and negative z/D and oscillates between 0.2 and 0.25. Since these oscillations are smaller than 0.05, the amplitude of drag fluctuations can be considered independent of offset variations. Increasing the angle of attack to $\alpha = 40°$ shows fluctuations are maximum at $z/D = 0$ with a value of $C_{d,rms} = 0.32$ and fluctuations decrease with increasing $|z/D|$. Again, the maximum fluctuations correspond to small offset distance with the airfoil fully embedded in the cylinder. Whereas at larger offset distances the airfoil moves away from the influence of the cylinder wake and reduces the amplitude of drag

fluctuations.

Fluctuations for the pitching moment behave differently, as figure 5.25(c) shows. Unlike the two other force components, fluctuations are largest for $\alpha = 0°$. In addition, at this low angle of attack fluctuations are minimum for $-0.25 \leq z/D \leq 0.25$ and increase for $|z/D| > 0.25$. This is the opposite of what occurs for the lift fluctuations. Furthermore, increasing the angle of attack not only reduces the amplitude of pitching moment fluctuations, it also lacks a local maximum value for the tested offset distances. Instead, amplitudes start low with values near $C_{m,rms} = 0.048$ at $z/D = -0.75$ and increase monotonically to $C_{m,rms} = 0.1$ at $z/D = 0.75$. This last trend occurs as the airfoil is pitched at a large angle with a positive offset distance. In this configuration, the pressure side of the airfoil is fully exposed to the turbulent cylinder wake and this amplifies fluctuations.

Results from this section demonstrate that the offset distance between the cylinder and airfoil influences the amplitude of the unsteady airloads on the airfoil. Negative offset distances reduce the amplitude of fluctuations across all force components. For lift and drag, larger angles of attack tend to increase the amplitude of fluctuations and create a local maximum near $z/D = 0$ to 0.25. In the case of the pitching moment, fluctuations are maximum for $\alpha = 0°$ and remain nearly independent of the offset distance.

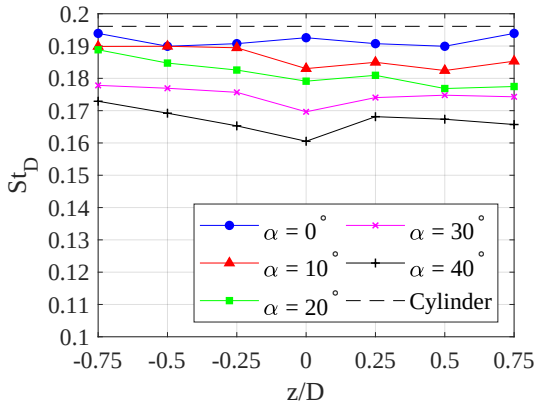

Figure 5.26: Evolution of the airfoil's frequency response due to variations in the offset distance parameter when $D/c = 0.36$ and $G/D = 3$.

5.4.3.2 Airfoil Frequency Response

Evolution of the Strouhal number for the airloads versus the offset distance is shown in figure 5.26 for various angles of attack. The dashed black line, $\mathrm{St}_D = 0.196$, represents the frequency of vortex shedding. For $\alpha = 0°$, the airfoil's frequency response is symmetrical for increasing magnitude of offset distance z/D, and St_D agrees well with the isolated cylinder frequency. Over the entire range of z/D, the Strouhal number varies from 0.190 to 194, indicating that the influence of the offset distance is minimal. Increasing the angle of attack to $\alpha = 20°$ shows a general decrease in St_D. In addition, the Strouhal number decreases more for positive offset distances, showing that the influence of the offset distance is noticeable at higher angles of attack. Further increasing the angle to $\alpha = 40°$ reveals a local minimum at $z/D = 0$ along with an asymmetry in the distribution of St_D. In the tested range of z/D, the Strouhal number is largest at $z/D = -0.75$ and decreases towards the local minimum at the zero offset configuration. The St_D begins to increase at $z/D = 0.25$

before the Strouhal number plateaus or decreases.

For all variations of z/D in figure 5.26, the Strouhal number does not vary more than 0.010 for all angles of attack. This suggests that the offset distance does not strongly influence the airfoil's frequency response when compared to the gap distance or cylinder diameter parameters. Therefore, the offset distance does not significantly alter the inflow to the airfoil and the cylinder wake continues to excite the airfoil at the cylinder vortex shedding frequency for low angles of attack ($\alpha \leq 10°$).

5.5 Effects of Varying Cylinder Cross-Sectional Geometry

This last section examines the effect of changing the cylinder cross-sectional geometry from a circle to a square. Figure 5.27 shows a sketch of the configuration where a square cross-sectional cylinder is rotated 45° with respect to the freestream flow. This orientation provides separation points at $z/D = \pm 0.5$ on the upper and lower corners. In order to perform an accurate comparison, the diagonal of the square must equal the circular cylinder diameter. Throughout this section D will also refer to the diagonal of the square cylinder. Comparison of the cylinder geometries are carried out for a single gap distance of $G/D = 5$, with zero offset between the cylinder and airfoil, and with a cylinder-diameter-to-airfoil-chord ratio of $D/c = 0.36$.

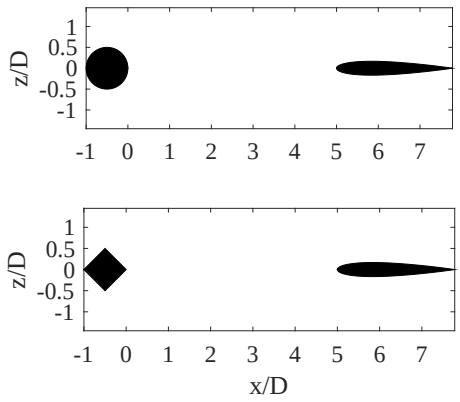

Figure 5.27: Sketch illustrating the cylinder-airfoil configuration for comparison of the cylinder geometry.

5.5.1 Time-Averaged Aerodynamics

The effect of varying the upstream cylinder cross-sectional geometry is illustrated in figure 5.28 by comparing lift, drag, and pitching moment coefficients. Globally, the airfoil force trends from a square cylinder wake are comparable to the circular cylinder case with some differences.

For the square cylinder configuration (blue square markers in figure 5.28(a)), the lift coefficient increases linearly for low angles of attack ($\alpha \leq 10°$), but there is a reduction in the lift curve slope when compared to the circular cylinder case (red circular markers). This indicates that the velocity deficit in the square cylinder wake is stronger than in the circular cylinder, based on the similar trend in figure 5.7(a). In addition, the square cylinder reduces the maximum lift coefficient from $C_l = 0.69$ compared to $C_l = 0.77$ for the circular geometry. However, the wake from the square cylinder increases the stall angle from 24° to 30°. This change in the stall angle is thought to be related to stronger velocity deficit and vortices in

the square cylinder wake. The stall behavior continues to lack the abrupt drop in lift, indicating that the cylinder-airfoil configuration is responsible for modifying the airfoil stall behavior. The square cylinder provides a very gradual drop in lift beyond stall, producing a plateau region up to $\alpha = 40°$.

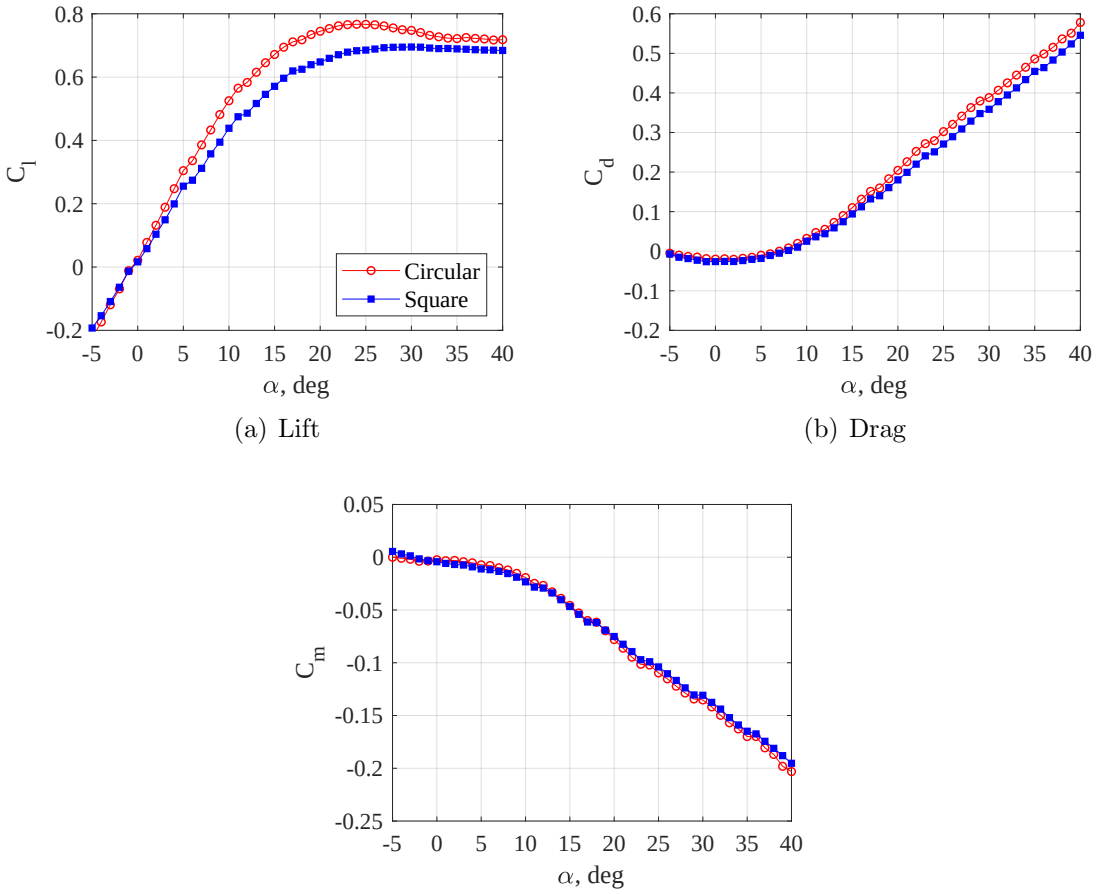

(a) Lift

(b) Drag

(c) Pitching moment

Figure 5.28: Influence of cylinder cross-sectional geometry on airfoil performance for $-5° \leq \alpha \leq 40°$ at $\mathrm{Re}_c = 1 \times 10^5$.

Minor differences exist for the drag and pitching moment coefficients as the cylinder geometry changes to a square. At low angles of attack, the square cylinder reduces drag slightly. Starting from $\alpha = 20°$, the difference in drag becomes a constant $\Delta C_d = 0.03$ up to $\alpha = 40°$ as the cylinder geometry changes to a square.

In contrast, the pitching moment coefficient is nearly indistinguishable regardless of the cylinder cross-sectional geometry. Overall, the cylinder cross-sectional geometry produces minute variations for the tested parameters.

5.5.2 Flowfields

The square cylinder does not significantly vary the time-averaged forces of a downstream airfoil as shown in figure 5.28. To understand why this is possible, an inspection of the flowfields is required. Figure 5.29 compares the resulting flowfield from cylinder cross-sectional geometries via smoke flow visualization.

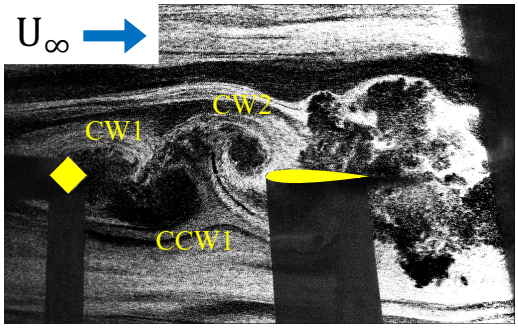

(a) Square cylinder, $\alpha = 0°$

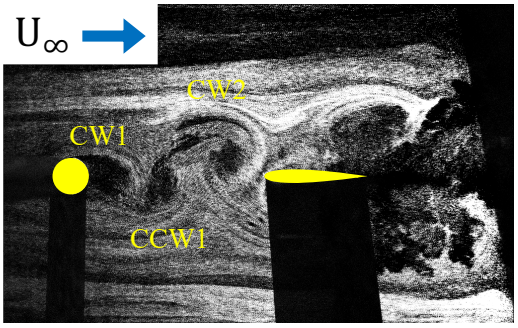

(b) Circular cylinder, $\alpha = 0°$

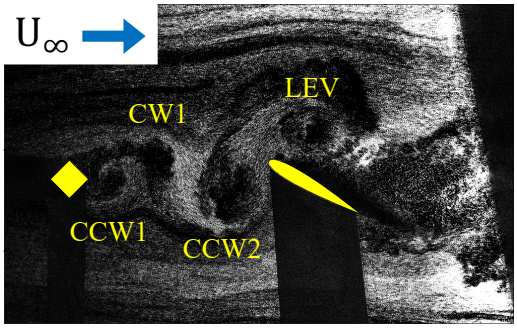

(c) Square cylinder, $\alpha = 30°$

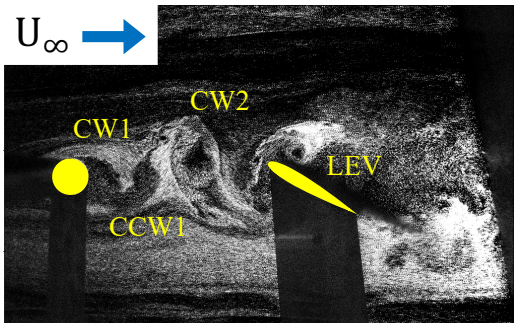

(d) Circular cylinder, $\alpha = 30°$

Figure 5.29: Comparison of smoke flow visualization for square and circular cylinder cross-sectional geometries when $D/c = 0.36$ and $G/D = 3$.

At $\alpha = 0°$, the square cylinder wake (see figure 5.29(a)) is characterized by

vortex shedding due to the formation of clockwise (CW1) and counterclockwise (CCW1) vortices from the upper and lower surfaces, respectively. Since the cylinder and airfoil are aligned, the shed vortices will impinge at the airfoil's leading edge as the clockwise vortex CW2 shows. In the case of the circular cylinder (see figure 5.29(b)), an identical wake is observed as the shed vortices encounter the downstream airfoil. At low angles of attack, flow structures in the wake of a square cylinder are nearly indistinguishable from a circular one.

Increasing the angle of attack to $\alpha = 30°$ shows the square cylinder continues to shed periodic vortices (see figure 5.29(c)). However, as the counterclockwise vortex (CCW2) sheds from the lower cylinder surface, it advects towards the airfoil. This induces the formation of a LEV on the suction side of the airfoil. Again, the circular cylinder exhibits nearly identical vortex structures in the wake flow as shown in figure 5.29(d).

Due to the similarity in the wake structures for both the square and circular cylinders, it is not surprising that the airloads in the cylinder-airfoil configuration have comparable trends. Although small differences were noted in figure 5.28, it is most likely these arise from wake properties that cannot be quantified from smoke flow visualization. Although the size of vortices seem comparable in 5.29, a complete vortex characterization is needed along with an estimation of the vortex strength. Unfortunately, the vortex characterization in this study was not carried out for these parameters.

5.5.3 Unsteady Airloads

Variations in the cylinder geometry show little effect on the airfoil performance and the smoke flow visualization shows qualitatively identical flow structures in the wake. To ascertain the influence of the cylinder geometry on the unsteady airfoil behavior, the following results will investigate the amplitude and frequency of the fluctuating airloads.

5.5.3.1 Amplitude of Fluctuations

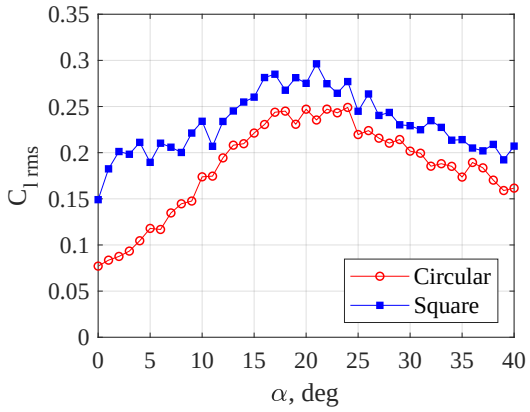

Figure 5.30: Influence of cylinder geometry on airfoil lift fluctuations.

Only the amplitude of fluctuations for C_l are presented here because the trends are qualitatively similar for the drag and pitching moment coefficients. Figure 5.30 shows the evolution of lift fluctuations versus the angle of attack for both the circular and square cylinders. The general trend for the square cylinder is identical to the circular case: fluctuations increase for $0° \leq \alpha \leq 17°$, peak in the vicinity of 20°, and decrease for $\alpha \geq 25°$. However, the square cylinder generates larger

fluctuations than the circular configuration for all tested angles of attack. At zero angle of attack, lift fluctuations increase from $C_{l,rms} = 0.08$ to $C_{l,rms} = 0.15$ simply by changing the cylinder geometry. As $\alpha \geq 12$, the influence of the square cylinder diminishes as fluctuations rise by 0.3 to 0.4. Although flow visualization showed similar wake structures for both cylinder cross-sectional geometries, the square cylinder increases the amplitude of fluctuations for the downstream airfoil, suggesting that the underlying difference depends on the cylinder wake properties.

5.5.3.2 Airfoil Frequency Response

Cylinder vortex shedding frequency depends on the bluff body geometry and figure 5.31 shows the influence of cylinder geometry on the airfoil frequency response. Reference Strouhal numbers are given for each cylinder geometry: the dashed line corresponds to a circular cylinder wake frequency, while the dot-dash represents the square cylinder frequency. A circular cylinder has a typical vortex shedding frequency higher ($\mathrm{St}_D = 0.196$) than its square counterpart ($\mathrm{St}_D = 0.170$ to 0.180) [114–117]. For the circular cylinder geometry, the airfoil frequency response matches the cylinder vortex shedding frequency at low angles of attack ($\alpha < 20°$). Increasing the angle of attack beyond $\alpha = 20°$ shows significant deviation from the reference frequencies for isolated cylinders. At large angles of attack, the airfoil's blockage effect influences the upstream cylinder vortex wake [65]. For the square cylinder cross-section, the frequency of the airloads synchronizes with the isolated square cylinder frequency of $\mathrm{St}_D = 0.170$ at low angles of attack, but deviates as α increases

past 20°.

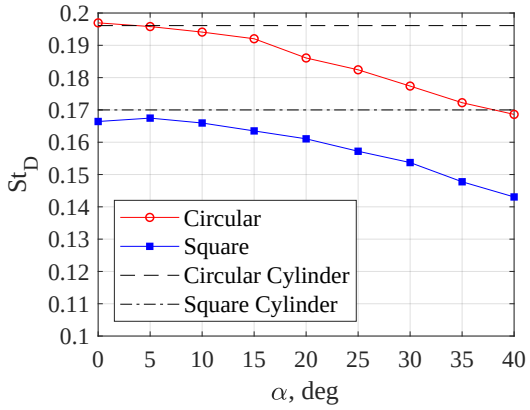

Figure 5.31: Effect of cylinder cross-sectional geometry on the Strouhal number of airfoil airloads.

This clearly shows that the frequency of airloads in the cylinder-airfoil wake is fully dependent on the frequency content of the cylinder wake. In the cylinder-airfoil configuration, the cylinder acts as turbulence generator with a characteristic frequency related to the vortex shedding mechanism. Since this wake is the inflow for the airfoil, the airfoil is excited as the same frequency; this results in lift, drag, and pitching moment to fluctuate at this cylinder wake frequency.

5.6 Chapter Summary

This chapter presented the modifications of airfoil performance due to four cylinder-airfoil parameters by varying the gap distance (G/D), the cylinder diameter to airfoil chord ratio (D/c), the offset distance (z/D), and the cylinder cross-sectional geometry. Results from time-averaged force measurements, smoke flow visualization, and spectral analysis revealed significant alterations to airfoil lift, drag,

pitching moment, stall, and unsteady behavior.

Prominent features of airfoil performance downstream of a cylinder wake are summarized as follows:

1. *Lift is augmented while stall is delayed.* For angles of attack $\geq 10°$, the true lift of the NACA 0012 airfoil downstream of the cylinder wake is significantly enhanced. At a gap distance of $G/D = 3$, the maximum lift coefficient increases to $C_{l,max} = 1.74$ which is more than double the isolated NACA 0012 value. This lift augmentation alters the airfoil stall characteristics, as stall is delayed to $\alpha = 31°$ and the post-stall lift curve is defined by a gradual decrease in lift. The gap distance parameter plays a critical role for lift enhancement and stall delay, as increasing G/D causes lift and stall angle to decline as they asymptote to the isolated airfoil values.

2. *NACA 0012 produces negative drag.* For low angles of attack ($\alpha \leq 8°$), the interaction between the cylinder wake and airfoil reduces airfoil drag to negative values. This effect decreases with increasing gap distance as drag approaches the isolated airfoil value, although C_d remains negative up to $G/D = 10$. It was found that increasing the cylinder diameter D/c amplifies negative drag on the NACA 0012, as larger wake structures interact with the airfoil.

3. *Fluctuations of the NACA 0012 airloads.* Encountering a periodic and turbulent wake, the NACA 0012 airfoil develops unsteady aerodynamic force production. The amplitude of fluctuations strongly depends on the relative position of the airfoil with respect to the cylinder wake, as fluctuations are maximum

at a small gap distances ($G/D = 3$) with no offset ($z/D = 0$). Cylinder geometry also influences the unsteadiness of airloads with larger cylinder diameters ($D/c = 1.04$) and a square cross-sectional geometry further increasing the amplitude of fluctuations.

4. *Frequency response of the NACA 0012.* In the cylinder-airfoil configuration, the cylinder wake acts as the inflow to the airfoil and excites the airloads at the cylinder vortex shedding frequency. For angles of attack $\alpha \leq 20^{\circ}$ and for gap distances $G/D \geq 5$, the airfoil's unsteady response is nearly identical to the frequency content found in the cylinder wake. This suggests the airfoil's unsteady airloads strongly depend on the properties of the incoming wake. However, at large angles of attack ($\alpha \geq 30^{\circ}$) and small gap distances ($G/D = 3$), the airfoil's blockage effect decreases the cylinder vortex shedding frequency. Since the frequency of the incoming flow decreases, the airfoil's airloads oscillate as this lower frequency. The airfoil's blockage effect decreases the cylinder vortex shedding frequency

These key findings are evidence that the cylinder-airfoil configuration significantly alters the NACA 0012 airfoil performance downstream of a cylinder wake. To make sense of the airfoil lift augmentation and negative drag during wake-airfoil interactions, an understanding of the responsible flow physics is presented in chapter 6.

Chapter 6: Elucidation of the Wake-Airfoil Flow Physics

The objective of this chapter is to understand the underlying flow physics found in the wake-airfoil interaction by relating flow structures to force trends identified in chapter 5. Flowfields from PIV and CFD provide the data for the analysis included in this chapter. The cylinder-airfoil configuration is limited to one case with a gap distance of $G/D = 3$, a cylinder-diameter-to-airfoil-chord ratio of $D/c = 1.04$, and a zero offset distance ($z/D = 0$). Each subsequent section will address one of the following questions:

1. How does the wake-airfoil interaction enhance lift and delay stall?
2. What flow structure causes negative airfoil drag at low angles of attack ($\alpha \leq 8°$)?
3. Which turbulence scales are responsible for the unsteady airfoil response during the wake-airfoil interaction?
4. How well do existing analytical models predict airloads of an airfoil subjected to a periodic disturbance?

Answering these questions will provide the reader with knowledge pertaining to the flow mechanisms found when a NACA 0012 airfoil encounters a cylinder wake.

6.1 Lift Augmentation and Stall Delay

This section will answer the following question: How do flow structures in the wake-airfoil interaction enhance airfoil lift and delay the stall angle? In order to gain a fundamental understanding of the flow physics, a detailed presentation of flow structures must first be given. The ensuing analysis will then identify and characterize key flow structures before associating them with lift augmentation and airfoil stall.

6.1.1 Phased-Averaged Flow Features

Flow visualization in previous chapters were either of a time-averaged or an instantaneous snapshot. Due to the periodicity of the cylinder wake, the cylinder-airfoil flow is revisited by phase-averaging PIV flowfields. Figure 6.1 displays vorticity contours at four distinct flow phases $t/T = \{0, 0.25, 0.5, 0.75\}$, where T is the period of cylinder vortex shedding. Blue contours indicate clockwise fluid rotation, while red corresponds to counterclockwise rotation.

At $t/T = 0$, the cylinder near wake shows the formation of clockwise and counterclockwise vortices on the upper and lower surfaces, respectively. Further downstream near $x/D = 3$, a previously shed clockwise vortex encounters the airfoil and collides with the leading edge. Interaction with the airfoil splits this vortex structure into two. As the cylinder wake continues to evolve at $t/T = 0.25$, the clockwise vortex grows, while the counterclockwise vortex sheds from the cylinder and advects towards the airfoil on a collision path. Further along the cylinder vortex

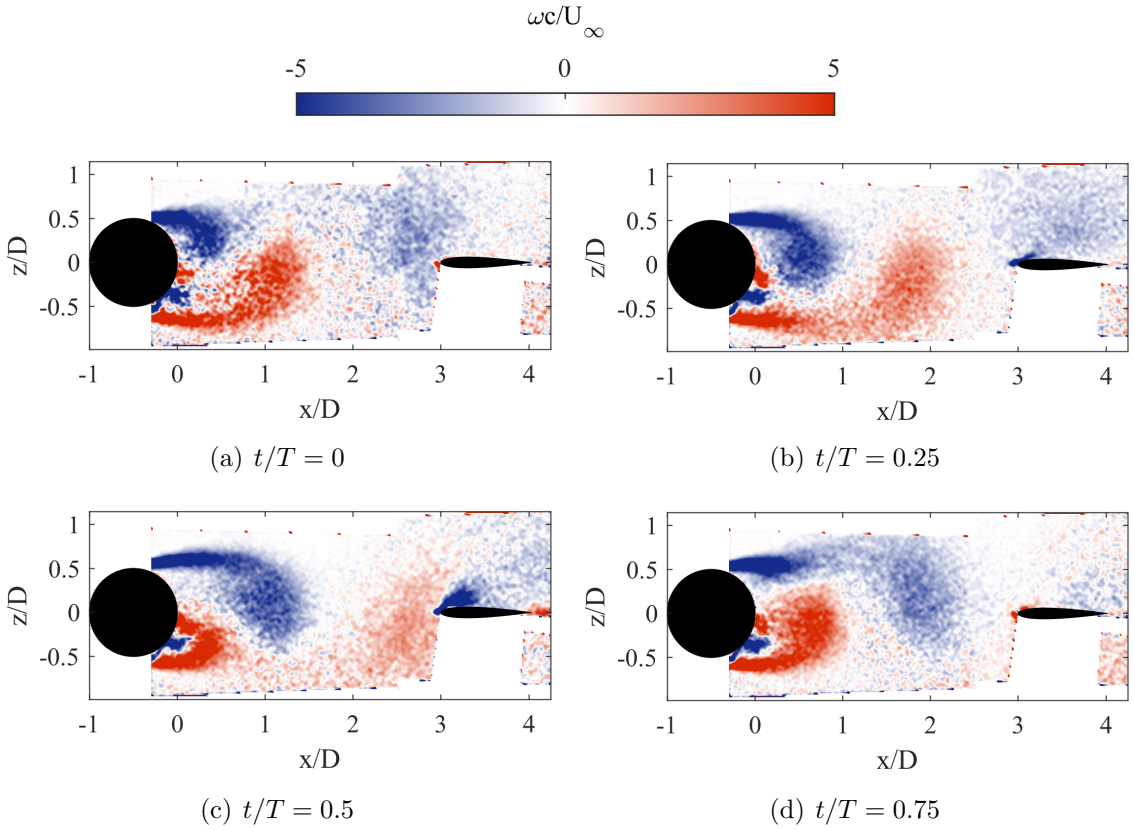

(a) $t/T = 0$ (b) $t/T = 0.25$

(c) $t/T = 0.5$ (d) $t/T = 0.75$

Figure 6.1: Phase-averaged vorticity contours of the cylinder-airfoil interaction when $\alpha = 0°$, $D/c = 1.04$, and $G/D = 3$.

shedding cycle, the flow at $t/T = 0.5$ is completely out of phase compared to $t/T = 0$, and the counterclockwise vortex encounters the airfoil. During this interaction, a new flow structure appears as a clockwise vortex is formed at the leading edge of the airfoil. Although the leading edge vortex (LEV) was previously observed in smoke flow visualizations in chapter 5, the current phase-averaged flowfields show this LEV forms as a result of the wake-airfoil interaction. At $t/T = 0.75$, the counterclockwise vortex interacting with the airfoil continues to advect downstream along with the LEV, where it begins to dissipate and lose coherency. The cylinder wake continues to shed new vortices and this process repeats, periodically forming new LEVs from

this wake-airfoil interaction.

These vorticity contour plots identify a critical flow feature that results from the periodic cylinder wake interacting with the airfoil: the LEV. In many cases, the formation of an LEV appears when the airfoil undergoes unsteady and aggressive kinematics such as pitching, translation, or a combination of both [118–122]. However, in the current study no kinematics are prescribed to the airfoil, and thus it is not immediately clear how the LEV is generated when the airfoil is held static at zero angle of attack.

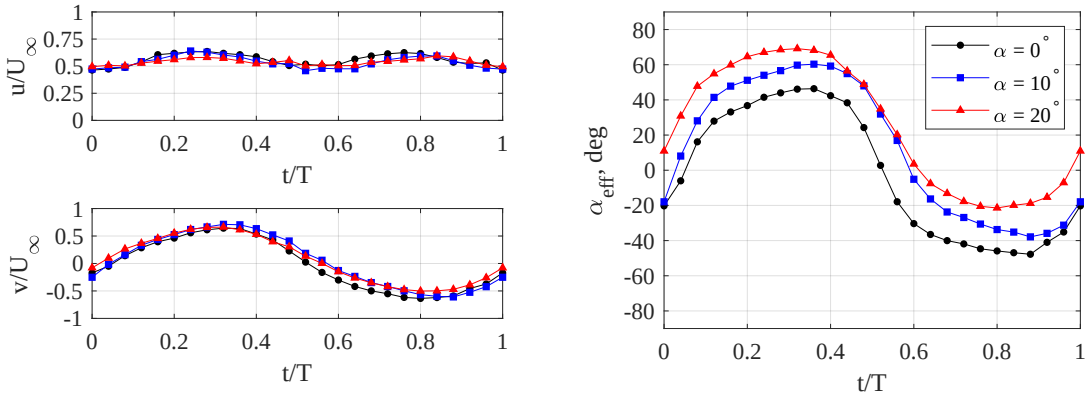

(a) Streamwise and transverse velocities

(b) Airfoil effective angle of attack, α_{eff}

Figure 6.2: Characterization of the phase-averaged airfoil inflow velocities at $x/D = 2.75$ and the resulting effective angle of attack when $D/c = 1.04$ and $G/D = 3$.

It is suspected that the unsteady inflow, produced by the upstream cylinder wake, plays a pivotal role in the LEV formation. Figure 6.2(a) characterizes both streamwise and transverse velocities upstream of the airfoil at $x/D = 2.75$, which corresponds to a quarter chord upstream of the leading edge. This location was selected due to the proximity to the airfoil while experiencing minimal flow distortion from its presence.

Due to the periodic nature of the cylinder wake, the streamwise and transverse velocities oscillate as shown in figure 6.2(a). In the time it takes to complete one vortex shedding cycle, the streamwise flow completes two cycles with maximums of $u/U_\infty = 0.64$ occurring at $t/T = 0.25$ and 0.75 and minimums of $u/U_\infty = 0.47$ at $t/T = 0$ and 0.5. In contrast, the transverse velocity only completes one cycle with a maximum amplitude of $|v/U_\infty| = 0.66$ at $t/T = 0.32$ and 0.8. Upstream of the airfoil, the inflow is characterized by a reduction in streamwise flow with moderate fluctuations, whereas the transverse velocity oscillates with a magnitude equal to 66 % of the freestream velocity.

Due to the significant transverse flow created by the cylinder wake, the flow angle upstream of the airfoil also varies during a vortex shedding cycle. The wake flow angle is defined as $\alpha_{wake} = \tan^{-1}\left(\frac{v}{u}\right)$ and in conjunction with the airfoil's geometric angle of attack α, the effective angle of attack for the airfoil is defined as

$$\alpha_{\text{eff}} = \alpha_{\text{wake}} + \alpha. \tag{6.1}$$

Figure 6.2(b) displays the variation of the airfoil's effective angle of attack during the cylinder vortex shedding cycle. For a geometric angle of attack $\alpha = 0°$, the effective angle of attack varies harmonically between $\alpha_{\text{eff}} = \pm 47°$. This provides an explanation for the development of the LEV when the NACA 0012 airfoil is at zero incidence. At these large effective angles of attack, flow cannot remain attached to the airfoil's surface and separates at the leading edge as a shear layer before rolling up into a coherent vortex structure. This flow mechanism is similar

to the formation of the dynamic stall vortex described for harmonically pitching airfoils [119,120]. Increasing the geometric angle of attack shifts the α_{eff} curve along the positive ordinate axis direction, and leads to maximum and minimum effective angles of $\alpha_{\text{eff}} = 69°$ and $-21°$, respectively, when the airfoil is pitched at 20°. This creates an asymmetry in the flow which will be discussed later.

Results presented up to this point show that the interaction between the cylinder wake and airfoil periodically creates a vortex at the airfoil's leading edge, even when the geometric angle of attack is $\alpha = 0°$. The formation of this structure is attributed to the oscillating flow created by the periodic cylinder wake as it induces a large effective angle of attack ($\alpha > 47°$) for the airfoil. Inevitably flow separates from the airfoil's leading edge, rolling up into the LEV even as the airfoil remains static.

6.1.2 LEV Characterization

The LEV is an important flow structure in the cylinder-airfoil configuration. To understand the underlying flow physics of this structure, the LEV must be quantitatively analyzed after being identified in the PIV flowfield. A detailed description of the vortex identification and characterization process is given in chapter 3, but a brief summary is provided here.

Vortices are identified from PIV velocity fields by decomposing the velocity gradient tensor $\nabla\vec{u}$ into a tensor $\mathbf{\Omega}$ describing fluid rotation and a tensor $\mathbf{S}$ describing fluid deformation. From these two tensors, the kinematic vorticity number $\mathcal{W} =$

$||\mathbf{\Omega}||/||\mathbf{S}||$ reveals vortex structures when $\mathcal{W} > 1$ [92]. The circulation of the LEV is estimated by $\Gamma = \int_S \vec{\omega} \mathrm{d}S$ where S is the surface area of a vortex region. Assuming vortices have a circular shape, the vortex core radius c_r is calculated by $c_r = \sqrt{\frac{S}{\pi}}$. Results from the vortex characterization are displayed in figure 6.3.

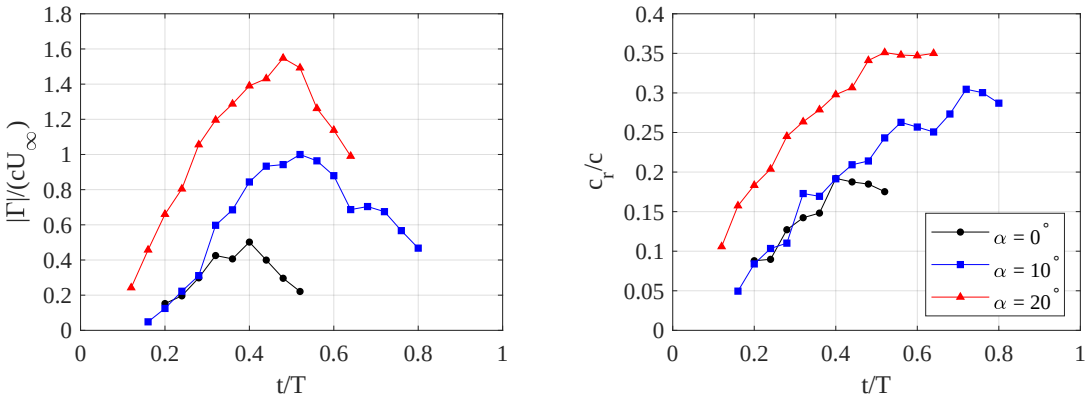

(a) Vortex strength, Γ (b) Vortex core radius, c_r

Figure 6.3: Characterization of the leading edge vortex when $D/c = 1.04$ and $G/D = 3$.

Vortex circulation in figure 6.3(a) is normalized by the airfoil chord c and the freestream velocity U_∞. For a geometric angle of attack $\alpha = 0°$, the LEV is first detected at $t/T = 0.2$ with $|\Gamma|/(cU_\infty) = 0.15$ and the vortex strength grows to a maximum of 0.5 at $t/T = 0.4$. Flow separation feeds the LEV growth as the effective angle of attack reaches a maximum of $\alpha_{\text{eff}} = 47°$ (see figure 6.2(b)) during the vortex shedding cycle. Beyond $t/T = 0.4$, the vortex strength begins to decrease as α_{eff} drops rapidly, suggesting that the wake-airfoil interaction no longer produces enough flow separation to sustain the LEV's strength.

Increasing the geometric pitch angle of the airfoil shows similar vortex growth, but the maximum circulation increases to $|\Gamma|/(cU_\infty) = 1.0$ and 1.5 for $\alpha = 10°$

and 20°, respectively. With a larger geometric airfoil angle of attack, α_{eff} increases accordingly to produce a more intense shear layer separation, which subsequently feeds the LEV growth to attain a larger vortex strength. Decrease in $|\Gamma|/(cU_\infty)$ is delayed to $t/T \approx 0.5$ for non-zero angles, as this correlates with the effective angle of attack rapidly decreasing in the later portion of the vortex shedding cycle, as shown in figure 6.2(b).

The core vortex radius c_r is normalized by the airfoil chord c and results are displayed in figure 6.3(b). Overall, the same trend applies to the evolution of the LEV size: as the vortex strength grows from $t/T = 0.2$ to 0.5 so does the vortex core radius. At zero angle of attack the maximum vortex size is 0.19, and this increases with increasing geometric angle of attack α to $c_r = 0.3$ for $\alpha = 10°$ and to $c_r = 0.35$ for $\alpha = 20°$. These results illustrate that the characteristics of the LEV depend on the airfoil's pitch angle α.

6.1.3 Effect of the LEV on Lift Augmentation and Stall

Assembling all the results from this section will provide an explanation as to why the wake-airfoil interaction promotes lift augmentation and stall delay. From phase-averaged vorticity contours shown in figure 6.1, the periodic nature of the cylinder wake creates an oscillating inflow for the airfoil which is reponsible for the formation of the LEV. As the wake flow angle is significant (see figure 6.2(b)), this LEV exists even at zero geometric angle of attack. Vortex characterization in figure 6.3 demonstrates the LEV size and strength depend on the airfoil angle of attack

and both quantities increase with α. Using the Kutta-Joukowski theorem, vortex circulation induces lift with the following relation

$$L = -\rho U_\infty \Gamma \tag{6.2}$$

where ρ is the fluid density. This equation relates the circulation of a vortex Γ to the lift force L.

Figure 6.4 compares the vortcity flowfields when a vortex shed from the cylinder encounters the downstream airfoil for geometric angles of attack $\alpha = 0°$ and $20°$. These flowfields are also compared at two phases ($t/T = 0$ and 0.5) of the vortex shedding cycle to visualize the LEV formation on both the suction and pressure sides of the airfoil. Figures 6.4(a) and 6.4(c) show a positive LEV on the lower surface at $t/T = 0$ and a negative LEV on the upper surface at $t/T = 0.5$. As the angle of attack increases to $\alpha = 20°$, figures 6.4(b) and 6.4(d) show that the LEV formation occurs only on the suction side of the airfoil. This indicates that for the given configuration, the effective angle of attack α_{eff} is not sufficiently large to generate a comparable LEV on the pressure side.

For zero angle of attack, the vortex strength of both LEVs are identical due to flow symmetry. Owing to the opposite signs in vorticity at $t/T = 0$ and 0.5, along with equation 6.2, the lift contribution from the LEV alternates from negative to positve during the shedding cycle. Therefore, this produces a net zero lift contribution at $\alpha = 0°$, which agrees with force measurements in chapter 5. In contrast, the net lift contribution at $\alpha = 20°$ will not be zero because the LEV only forms on the

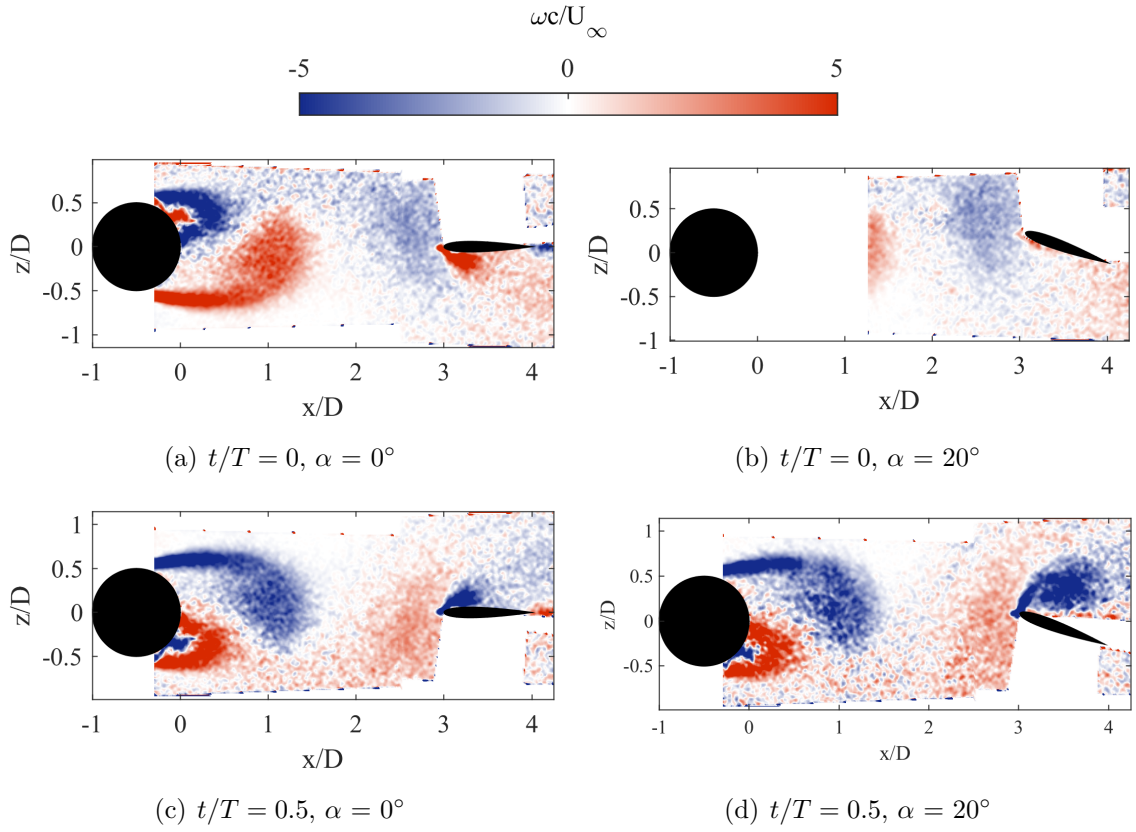

(a) $t/T = 0$, $\alpha = 0°$

(b) $t/T = 0$, $\alpha = 20°$

(c) $t/T = 0.5$, $\alpha = 0°$

(d) $t/T = 0.5$, $\alpha = 20°$

Figure 6.4: Comparison of phase-averaged vorticity fields for the airfoil's suction and pressure sides at $\alpha = 0°$ and $20°$.

suction side of the airfoil. This vortex lift contribution produces the lift augmentation seen in the force measurements in chapter 5. Therefore, the time-averaged lift for the airfoil is augmented in the cylinder-airfoil configuration. Increasing the angle of attack increases the lift augmentation mechanism as figure 6.3(a) shows the vortex strength Γ grows with α. With significant lift production due to the LEV at $\alpha = 20°$, it becomes evident that airfoil stall is significantly delayed.

6.2 Negative Drag

Generally, airfoil drag is not expected to be negative. Yet, drag reduction techniques are constantly sought after in most aerodynamic applications. In the current thesis, negative drag was measured as a consequence of the cylinder-airfoil configuration affecting airfoil performance. Unraveling the underlying flow physics of negative drag during a wake-airfoil interaction will also further our knowledge of drag-reducing techniques. Thus this section will answer the following question: What flow physics are responsible for negative drag production in the cylinder-airfoil wake at low angles of attack?

In a similar study to the current one, Liao et al. [72] investigated force behavior of an elliptical foil in the wake of a circular cylinder and numerically measured negative drag. Although the authors did not provide an explanation for the production of thrust, they noted that forces generated by an inflow of vortices is the primary mechanism for airfoil propulsion [123, 124]. A key difference in references [123, 124] is that the airfoil is prescribed a pitching and heaving motion, and as this dynamic airfoil interacts with an upstream cylinder wake it produces thrust. This propulsive force arises from a tilting of the lift vector in the upstream direction due to body kinematics [47, 125] and the presence of a reverse von Kármán vortex street downstream of the airfoil. Results from Koochesfahani [126] and Triantafyllou et al. [127] show that this reverse von Kármán vortex street produces a wake with a jet profile, inducing thrust production. However, the airfoil in the current study remains static and does not display a reverse von Kármán vortex wake as shown by the vorticity

contours in figure 6.5. Therefore a different flow mechanism must be responsible for negative drag in the current study.

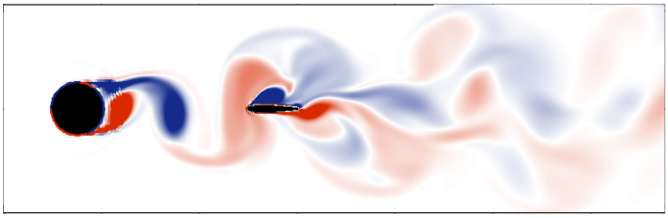

Figure 6.5: Instantaneous vorticity field from CFD for $D/c = 1.04$ and $G/D = 3$ (A. Grubb, private communication, July, 2020).

In an incompressible flow, the total drag on a body is due to a combination of pressure drag and friction drag. For a streamlined body, such as an airfoil at low angles of attack, skin friction drag dominates compared to the pressure term. Hence, only skin friction drag will be included in the following analysis. The skin friction coefficient is defined as

$$C_f = \frac{\tau_w}{0.5\rho U_\infty^2} \tag{6.3}$$

with

$$\tau_w = \mu \frac{\partial u}{\partial n} \tag{6.4}$$

where τ_w represents the shear stress at the airfoil's surface for a fluid with dynamic viscosity μ, flow velocity u, and calculated in the outward direction n normal to the surface.

Using flowfield data from CFD (A. Grubb, private communication, July, 2020), the local skin friction coefficient C_f of the airfoil downstream of a cylinder's wake is

shown in figure 6.6. The time-averaged skin friction coefficient is plotted for both the upper and lower surfaces of the airfoil with the abscissa depicting the distance from the airfoil's leading edge ($x/c = 0$) to the airfoil's trailing edge ($x/c = 1$). A sketch of the NACA 0012 airfoil is added to aid in visualizing the skin friction distribution along the surface. Results show that the skin friction coefficient has a strong negative peak near the leading edge ($x/c = 0$) and remains negative until $x/c = 0.06$. From $0.07 \leq x/c < 0.19$, skin friction is positive with a maximum value of $C_f = 0.007$ at $x/c = 0.12$. The remainder of the airfoil's surface, $0.19 \leq x/c < 1$, is characterized by a negative skin friction with values ranging reaching $C_f = -0.012$. Over most of the airfoil's surface, negative skin friction dominates implying that the airfoil is subjected to significant flow reversal. In a time-averaged sense, the airfoil sees fluid flowing from the trailing edge to the leading edge. As the drag force must oppose the flow direction and combined with flow reversal on the airfoil's surface, drag acts in the upstream direction producing negative drag (or thrust).

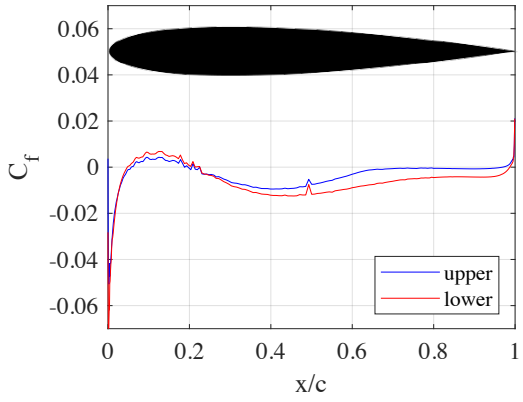

Figure 6.6: Time-averaged skin friction coefficient C_f for the NACA 0012 airfoil downstream of the cylinder's wake when $G/D = 3$ and $\alpha = 0°$.

To understand the underlying flow physics, the flow reversal leading to negative

drag must be associated with a flow structure from the cylinder-airfoil wake. Figure 6.7(a) displays a zoomed in view of the vorticity contours overlaid with the velocity vectors for an instantaneous snapshot of the flow from CFD (A. Grubb, private communication, July, 2020). A large counterclockwise vortex (red) shed from the upstream cylinder, collides with the airfoil. Due to the rotation of this flow structure and its interaction with the airfoil, the velocity vectors show a large flow angle at the airfoil's leading edge, which induces flow separation. A shear layer forms and rolls up into the clockwise LEV (blue) on the upper surface of the airfoil. Since the LEV vortex rotates in a clockwise direction, it induces flow to travel from the trailing edge to the leading edge along the upper surface of the airfoil. This clearly shows the LEV is responsible for the flow reversal in the wake-airfoil configuration. In contrast, fluid on the lower surface remains fully attached and flows from the leading edge to the trailing edge as it is unaffected by the LEV.

Figure 6.7(b) shows an instantaneous PIV flowfield to compare with the numerical solution. In this figure, the vorticity contours and velocity vectors are in excellent agreement with flow features described for figure 6.7(a), validating the CFD flowfield. The only difference that exists is the presence of turbulence highlighted by the small spatial variations in vorticity intensities across the background.

Figure 6.7(c) quantifies the skin friction coefficient from the instantaneous CFD flowfield in figure 6.7(a) and clearly illustrates that the reverse flow from the LEV is responsible for the negative skin friction. The large dip in C_f from $x/c =$ 0.19 to 0.62 on the upper surface coincides with the center of the LEV at a location of $x/c = 0.47$. As the magnitude of the negative skin friction coefficient is larger

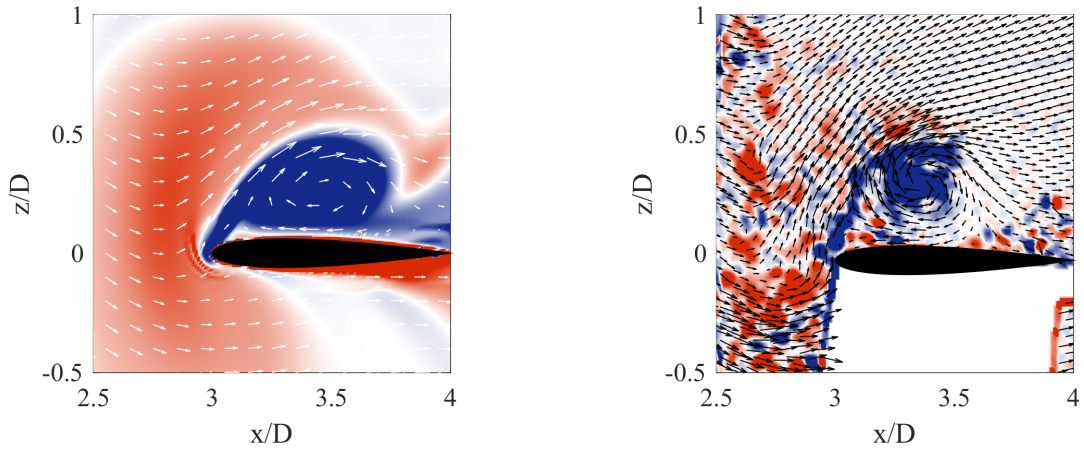

(a) CFD

(b) PIV

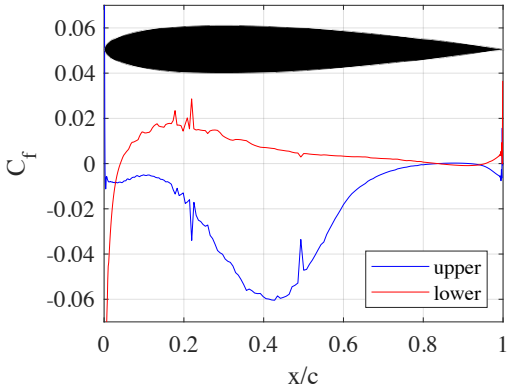

(c) Skin friction coefficient, C_f

Figure 6.7: Instantaneous skin friction coefficient C_f with corresponding flowfields from (a) CFD and (b) PIV when $D/c = 1.04$ and $G/D = 3$.

than the positive values, the airfoil experiences a net negative drag at this instant. The LEV structure formed from the wake-airfoil interaction is the source of negative drag as these results demonstrate.

Over the entire shedding cycle, the LEV produces enough reverse flow on the airfoil's surface to generate a net skin negative drag as the time-averaged values shows in figure 6.6. Although the LEV grows with increasing angle of attack as the vortex characterization shows (see figure 6.3), force measurements indicate positive

drag for $\alpha > 8°$. This change in sign of the drag force is expected as the pressure drag cannot be neglected for moderate to high angles of attack. Hence, there is a value of α where the pressure and skin friction drag have equal and opposite contributions leading to zero drag, as shown in figure 5.12(b).

6.3 Turbulence Scales

The previous sections showed the LEV plays a critical role in understanding the modification of airfoil force production in the cylinder-airfoil configuration. Yet, the cylinder wake is fully turbulent and contains a wide range of turbulence scales that were characterized in chapter 4. This section will investigate the influence of various turbulence length scales by separating flow scales to answer the following question: Which turbulence scales are responsible for the unsteady airfoil response in the wake-airfoil interaction?

6.3.1 Frequency Domain Filters

Frequency domain filters are used to separate turbulence scales in the acquired PIV flowfields. This method was selected due to its simple implementation and meaningful physical interpretation. Filtering in the spatial domain requires a convolution between the input and the filter functions. This operation can be simplified by taking advantage of the convolution thoerem stating that the convolution between two functions in the time domain is equivalent to the product in the frequency domain. The flowchart in figure 6.8 details the filtering operations with an

example.

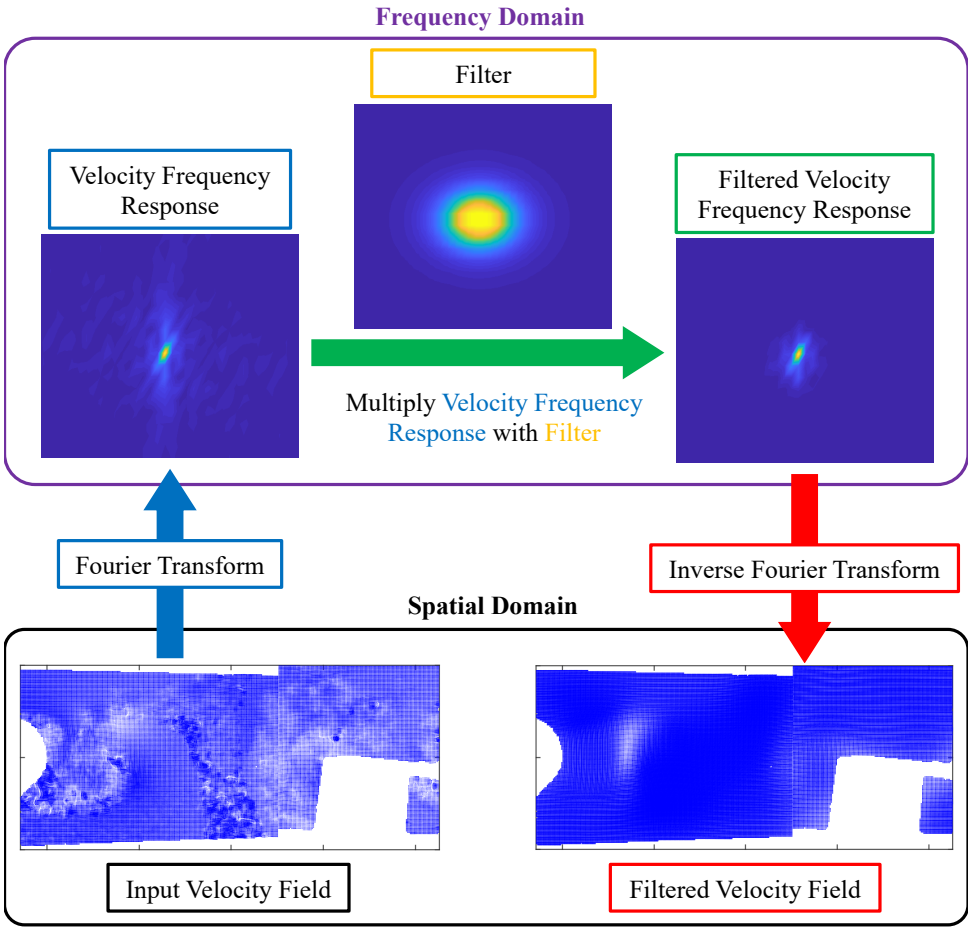

Figure 6.8: Flow decomposition using frequency domain filters.

First, the velocity field acquired by PIV (bottom left of figure 6.8) is transformed into the frequency domain with a Fourier transform. The resulting two-dimensional amplitude spectrum (top left of figure 6.8) displays a central peak along with many smaller contributions in several radial directions. A filtered response is achieved by multiplying the velocity field with a filter (top center of figure 6.8) in the frequency domain. The filtered frequency response (top right of figure 6.8) shows a similar spectrum as the pre-filtered response near the center, but the response is severely attenuated away from the center. Finally, the result is inverse Fourier

transformed back into the spatial domain to reveal the effect of the filter on the velocity field (bottom right of figure 6.8).

A low-pass filter was implemented for this example, and comparing the input velocity field with the filtered field shows the response has been smoothed. This indicates the removal of high frequency content related to small scale velocity fluctuations. The described filtering operations successfully separate the flow scales since the filtered flowfield only contains large velocity flow scales.

In the following analysis, the flow is to be separated into three groups of length scales: large, medium, and small. The desired flow scale decomposition is accomplished by applying low-pass, band-pass, and high-pass Butterworth filters. The transfers functions H for these three filters are given by the following equations [128, 129],

$$H_{LowPass}(i,j) = \frac{1}{1+[D(i,j)/D_0]^{2n}} \tag{6.5}$$

$$H_{BandPass}(i,j) = 1 - \frac{1}{1+[\frac{D(i,j)W}{D(i,j)^2-D_0^2}]^{2n}} \tag{6.6}$$

$$H_{HighPass}(i,j) = \frac{1}{1+[D_0/D(i,j)]^{2n}} \tag{6.7}$$

where $D(i,j)$ is the distance from the center of the filter, D_0 is the cutoff frequency, W is the band width, and n is the order of the filter. For each filter, the order was set to $n = 2$ throughout the following analysis. The wavenumber is defined as the spatial frequency with $k_0 = 1/\lambda$ with λ being the wavelength. The low-pass filter attenuates wavenumbers greater than the cutoff wavenumber k_l, while the the high-pass filter attenuates wavenumbers smaller than k_h. The band-pass filter attenuates

wavenumbers outside the band defined by the low and high cutoff wavenumbers, $k_l < k_0 < k_h$.

Table 6.1: Filter parameters for flow scale decomposition.

Filter type	Cutoff wavenumber 1/m	Normalized cuttoff wavenumber, $(k_0 c)^{-1}$
Low-pass	$k_l = 14.28$	1
High-pass	$k_h = 142.8$	0.1
Band-pass	$k_l = 15$	$(k_l c)^{-1} = 0.95$
	$k_h = 125$	$(k_h c)^{-1} = 0.11$

Table 6.1 summarizes the filter parameters used for the current analysis, while a sensitivity study in Appendix A determined appropriate cutoff wavenumbers. Separation of flow scales is related to the airfoil chord c, with large scales defined as larger than one chord, medium scales are on the order of the chord ($0.95 \leq c \leq 0.11$), and small scales are smaller than $0.1c$.

Applying this flow decomposition technique to the velocity spectrum shown in figure 6.9 illustrates the effectiveness of separating flow scales. The black curve represents the unfiltered spectrum, while the blue, green, and red curves define the low-pass, band-pass, and high-pass responses, respectively. For the low-pass filter, wavenumbers below the cutoff frequency k_l show excellent agreement with the original spectrum, indicating that only large flow structures are retained. Similarly, the band-pass filter extracts scales in the middle of the spectrum, while attenuated contributions from wavenumbers outside the defined $k_l < k_0 < k_h$ band. The high-pass filter clearly captures the remaining small scales from this decomposition. Figure 6.9 demonstrates the filtering technique is successful at separating the velocity spectrum based on flow length scales.

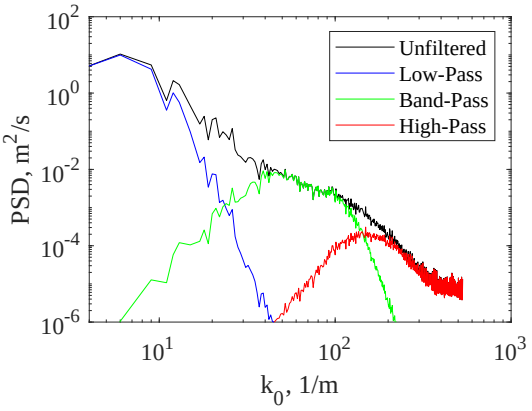

Figure 6.9: Scale based decomposition of PSD resulting from filter operations.

6.3.2 Separation of Flow Scales

Applying all filters to the PIV data produces a decomposition of the flowfield as shown in figure 6.10. Prior to the filtering operations, figure 6.10(a) displays the original vorticity field along with the corresponding velocity vectors. Key features of this flow illustrate the upwash from the cylinder wake upstream of the airfoil's leading edge, causing flow separation as the shear layer rolls up into the LEV. Velocity vectors show this vortex rotates in the clockwise direction, hence the blue vorticity contours. A small amount of counterclockwise vorticity, indicated by the red contour, appears offset from the vortex center at $x/D = 3.35$ and $z/D = 0.25$. Above the trailing edge of the airfoil near $x/D = 4$, alternating signs of vorticity reveal flow turbulence with smaller scales compared to the LEV. Since all of these flow features occur at different locations with varying size, this will help determine the efficacy of the flow decomposition process.

Figure 6.10(b) shows the reconstruction of the flowfield obtained from sum-

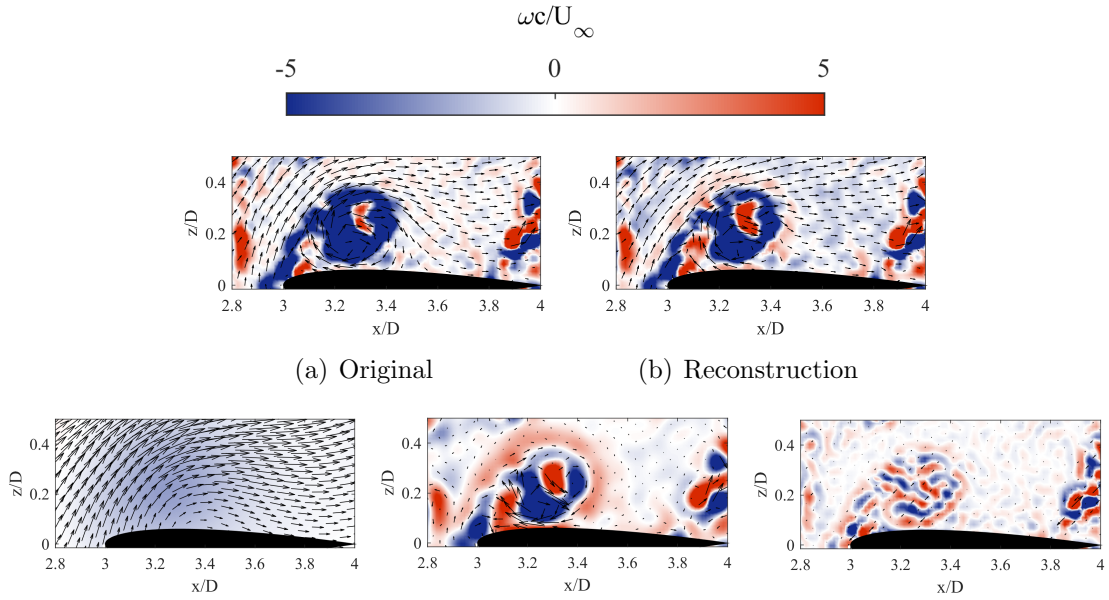

(a) Original (b) Reconstruction

(c) Low pass (d) Band pass (e) High pass

Figure 6.10: Comparison of vorticity contours and velocity vectors from flow scale separation.

ming the low-pass, band-pass, and high-pass decomposed flowfields. There is good agreement between the original and reconstructed flowfield as the velocity vectors, shear layer, LEV, and turbulent flow at the edge of the frame are all well represented. However, small differences are noticeable including an increase in the background vorticity, with counterclockwise vorticity (red) surrounding the LEV.

A closer look at each decomposed flowfield is illustrated in figures 6.10(c), 6.10(d), and 6.10(e). The low-pass field (figure 6.10(c)) shows the influence of flow scales larger than the airfoil's chord. Because the LEV is smaller than the airfoil's chord (see figure 6.10(a)), and its diameter was characterized as 40 % of the airfoil chord in figure 6.3(b), the LEV is removed in the low-pass filtered flow. The velocity field retains the upwash from the cylinder wake, while the intensity in vorticity

magnitude decreases significantly. In this flowfield, large flow scales only contribute to the background flow as no distinct key flow structures appear as a result of the low-pass filter.

The resulting flow decomposition from the band-pass filter (figure 6.10(d)) shows several key flow structures. Part of the shear layer at the leading edge is captured and the entire core structure of the LEV is present. Velocity vectors are significant within the LEV and diminish far away, demonstrating that the LEV is a medium flow scale as the band-pass filter retains this flow structure. The decrease in velocity away from the LEV causes a velocity gradient responsible for the red vorticity surrounding the LEV, which is clearly visible in this figure and in the reconstruction (see figure 6.10(b)). The decomposition from the band-pass filter reveals that flow scales comparable to the airfoil chord might be dominant due to the large intensity in vorticity.

Finally, the high-pass filter extracts the smallest flow scales from the flowfield in figure 6.10(e). This reveals the underlying LEV structure consist of many smaller flow scales and the turbulent flow over the trailing is also characterized by these small structures. The intensity of the vorticity for these small scales is clearly larger than the low-pass flow decomposition, but is qualitatively comparable to the band-pass result. In order to determine the contribution of each separated flow scale on the flowfield, a quantitative approach is needed.

The enstrophy parameter will be used to compare the contributions of each flow scale decomposition with respect to the original flowfield. For an incompressible

flow, enstrophy is defined as

$$E = \int_S \omega^2 \mathrm{d}S \tag{6.8}$$

which represents the flux of vorticity squared through a surface S. Calculating the enstrophy for each filtered flowfield during the LEV formation and shedding will quantify the contribution from each flow scale.

Figure 6.11 shows the evolution of the relative enstrophy E/E_0, where E_0 is the enstrophy from the unfiltered flow. In addition, the decomposed vorticity fields are illustrated for two distinct times. Flowfields on the left of figure 6.11 represent the LEV growth stage, while the vorticity contours on the right of the figure depict the flow after the LEV sheds and advects out of the field of view. During the entire process, the relative enstrophy E/E_0 for the band-pass filtered flow field is consistently the largest contribution with values ranging from $E/E_0 = 0.33$ to 0.53. Large scales from the low-pass filtered flowfield do not contribute significantly as values are generally less than $E/E_0 = 0.1$. This suggests that large flow scales do not directly contribute to the unsteady airloads on the airfoil. Small scales from the high-pass filter vary considerably as values range from $E/E_0 = 0.11$ to 0.33. This creates two distinct regions: (1) a region where small scales do not contribute significantly and medium scales dominate ($0.4 \leq t^* \leq 2.5$), and (2) a region where medium and small scale are comparable ($2.5 < t^* \leq 5$).

In this first region, the LEV is the dominant flow structure as shown by the vorticity contours on the left of figure 6.11. Thus scales ranging from $0.11c$ to $0.95c$ are primarily affecting the airfoil during the presence of the LEV. In contrast, as

the LEV advects and the turbulent wake from the cylinder interacts with the airfoil, scales smaller $0.1c$ affect the airfoil approximately as much as the medium scales. Vorticity fields on the right of figure 6.11 show this. Thus, turbulence scales with sizes comparable to the airfoil chord play a critical role in the wake-airfoil interaction, but smaller scales are non-negligible in the absence of large coherent structures such as the LEV.

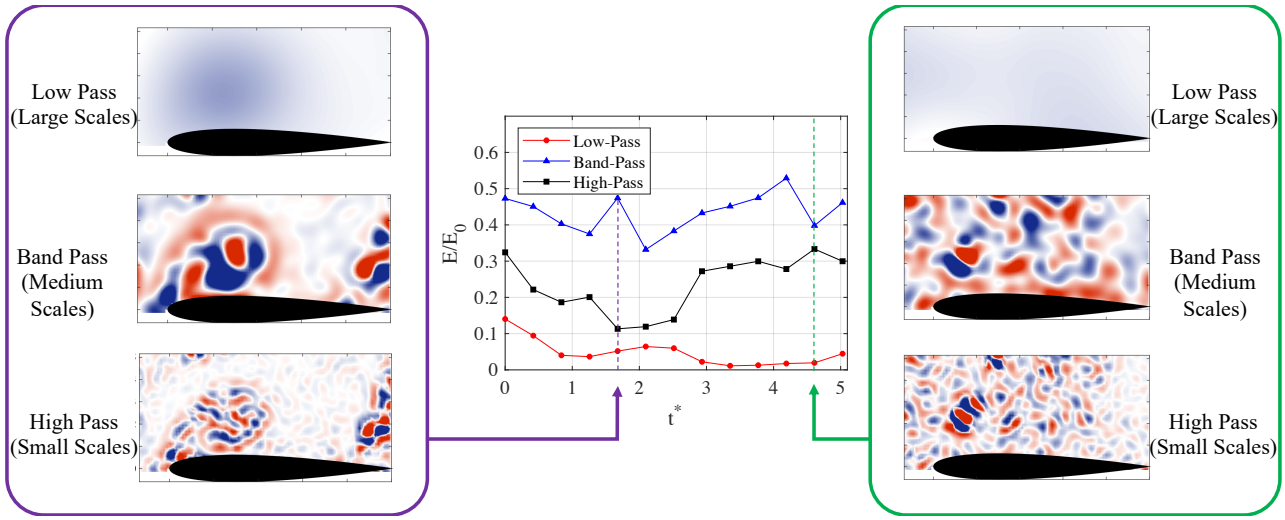

Figure 6.11: Relative enstrophy E/E_0 for each decomposition level with corresponding vorticity contours.

6.4 Predicting Cylinder-Airfoil Airloads Via Analytical Models

In the previous sections of this chapter, the flow physics of the wake-airfoil interaction demonstrated that the LEV formed plays a critical role in modifying airfoil performance. The ability to predict these changes in the unsteady airfoil behavior accurately and rapidly is essential for many engineering applications. To evaluate any shortcomings of existing low order models, this section will compare

three analytical methods with time-resolved force measurements from CFD. These three models include Theodorsen's [73], Sears's [25,26], and Atassi's [27,28] theories. For this comparative study, the cylinder-airfoil gap distance is set to $G/D = 3$ with a cylinder diameter size of $D/c = 1.04$ and the airfoil angle of attack is $\alpha = 0°$.

6.4.1 Overview of Models: Theodorsen, Sears, and Atassi

A brief summary of each model was initially presented in chapter 2. Only the main concepts and assumptions used by each model are recalled here. Theodorsen's theory describes a solution for a harmonically oscillating airfoil in a steady, inviscid and incompressible flow [73]. Although the airfoil remains static in the cylinder-airfoil configuration, the cylinder wake provides a harmonic variation in the flow angle of attack (see figure 6.2) which is not too dissimilar from the original model. The corresponding lift response from Theodorsen's theory [74] is given by

$$C_l = \pi \frac{c^2}{4} \left(\frac{\dot{\alpha}}{U_\infty} - \frac{a\ddot{\alpha}}{U_\infty^2} \right) + 2\pi C(k) \left(\alpha + (\frac{1}{2} - a) \frac{\dot{\alpha} c}{2U_\infty} \right) \tag{6.9}$$

where $\dot{\alpha}$ is the angular velocity, $\ddot{\alpha}$ is the angular acceleration, k is the reduced frequency, and $C(k)$ is Theordorsen's function. Equation 6.9 assumes a thin airfoil, small perturbations, and attached flow.

For a better model of the oscillating flow created by the cylinder wake, Sears's theory models a static airfoil encountering a harmonically oscillating transverse gust [25, 26]. This oscillating gust uniformly translates with the freestream U_∞, creating an alternating distribution of upwash and downwash akin to a cylinder wake. Sears's

result [74] is expressed as

$$C_l = 2\pi \left(\frac{v_0}{U_\infty} \right) S(k_g) e^{i2\pi U_\infty t/\lambda_g} \tag{6.10}$$

where v_0 is the transverse gust amplitude, λ_g is the gust wavelength, and $S(k_g)$ is the Sears function. Equation 6.10 is valid for a thin airfoil subjected to small gust perturbations ($v_0 << U_\infty$) and attached flow.

Atassi's model is an extension of Sears's as it includes a streamwise gust component and non-linear distortion effects due to airfoil angle of attack, camber, and thickness [27, 28]. These non-linear contributions make this a second order model and the unsteady airfoil response is given by

$$C_l = 2\pi\beta A(k_1, k_2) e^{-ik_1 t} \tag{6.11}$$

where k_1 is the transverse gust amplitude, k_2 is the streamwise gust amplitude, β is the gust strength, and $A(k_1, k_2)$ is Atassi's function [28]. Compared to Sears's model, notable differences include two gust reduced frequencies, a coupling of the streamwise and transverse gust, and the gust strength β is a consequence of the continuity equation instead of depending on the gust angle [77, 78]. Atassi's model does not include any additional assumptions compared to those noted for Sears's theory.

6.4.2 Unsteady Aerodynamic Model Response

To compare the response of the analytical models, the following parameters needed to be estimated: the time-varying flow angle, streamwise and transverse velocity amplitudes, and reduced frequency of the gust. Using the CFD flowfield provided by collaborators at Georgia Tech (A. Grubb, private communication, July, 2020), these parameters were determined a quarter-chord upstream of the airfoil's leading edge in a similar manner as the PIV data used in figure 6.2. The velocity amplitudes were simply extracted from the CFD data, while the reduced frequency was calculated from an FFT of the instantaneous transverse velocity signal.

Unsteady airfoil lift coefficients for one period of oscillation from all three models are compared to the C_l obtained from CFD in figure 6.12(a). The unsteady lift response from CFD oscillates from -1.5 to 1.4 with the minimum occurring at $t/T = 0.05$ and the maximum at $t/T = 0.53$. Every model produces a similar response with each output having the same shape; however, significant discrepancies exist compared to the baseline force response.

Theodorsen's theory exhibits an overshoot with a maximum amplitude of $C_l = 6.0$ at $t/T = 0.42$, and this result is out of phase since the CFD peak value appears at $t/T = 0.52$. Thus this model does not perform well due to the overshoot and lag of the predicted response. The Sears and Atassi models have a lower lift amplitude, but both models continue to overshoot the CFD reference case with $C_l = 3.8$. Although the magnitude of the response is inaccurate, the phase of the signal is synchronized with the CFD lift response. This suggests that modeling the cylinder

wake with a harmonic gust provides some physical semblance as the phase response matches.

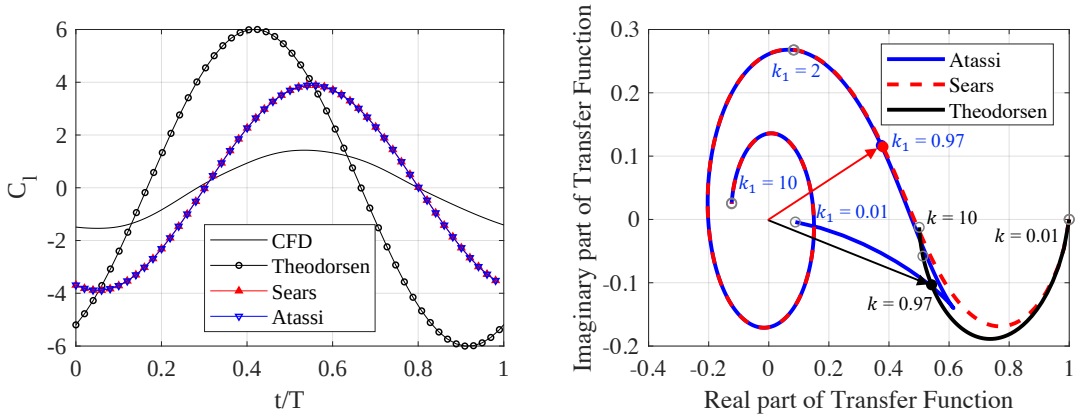

(a) Lift coefficient response

(b) Transfer functions

Figure 6.12: Comparison of model response and transfer functions.

It is unsurprising that Theodorsen's theory fails to capture the unsteady behavior of the cylinder-airfoil response because airfoil kinematics of an oscillating airfoil are not equivalent to an oscillating inflow. In fact, the oscillating airfoil will include an inertial term called *added mass* which corresponds to the force required to displace the surrounding fluid. However, it is unexpected to notice an identical response between Sears and Atassi, as the latter takes into account the streamwise gust component and airfoil thickness. What physical mechanism could explain the similarity between the Sears and Atassi models for the tested flow configuration? The phase-averaged inflow velocity variations in figure 6.2(a) provides some insight. The maximum amplitude of the streamwise fluctuations is $0.15U_\infty$, while the ampltiude of transverse fluctuations reaches 0.66 of the freestream velocity. As the streamwise fluctuations are significantly smaller than those in the transverse direction, they can be neglected. Therefore, Atassi's model reduces to Sears' theory when

streamwise gust components are small and the aerodynamic response between both models becomes identical.

Figure 6.12(b) plots the real and imaginary parts of the transfer function for all three models. The filled colored circular markers indicate the value of reduced frequencies ($k_1 = 0.97$) for the given baseline configuration, while the gray markers show the evolution of the transfer function response for increasing k. At very low reduced frequencies ($k_1 < 0.05$), the response from Theodorsen and Sears are identical with amplitude reduction less than 10 % and a small phase lag. Atassi's model is considerably different at these low k_1 values as the response is greatly attenuated with an amplitude reduction of 60 %. Increasing the reduced frequency shows the Atassi and Sears models converge and begin to spiral about the origin.

Focusing on the reduced frequency used for the comparison (colored markers), the amplitude response of each model is visualized by an arrow starting from the origin. This clearly shows the amplitude from Theodorsen's theory is larger than the two other models, thus explaining why the overshoot is substantial in figure 6.12(a). For Sears and Atassi's models, the blue and red circular markers are indistinguishable and leads to an identical amplitude and phase response as seen in figure 6.12(a).

Results from this section show that existing low order models are inadequate at predicting unsteady airfoil force production when downstream of a cylinder wake. These models are only accurate if the assumptions used when deriving them are satisfied. However, the cylinder-airfoil configuration exhibits large perturbations created by the cylinder wake and the flow is massively separated with many vortex

structures populating the wake. These two features invalidate the assumptions of small disturbance and attached flow. To improve the current models, future work can integrate the flow physics presented in this chapter to develop accurate models to improve force prediction capabilities for wake-airfoil interactions.

6.5 Chapter Summary

This chapter investigated the flow physics of wake-airfoil interactions to answer several questions that were raised in response to results presented in previous chapters. An analysis based on experimental and numerical results provides an explanation for changes in airfoil performance such as lift augmentation, stall delay, and negative drag. A flow decomposition of PIV flowfields assessed the impact of different turbulence scales on the flow around the airfoil, while a comparison of existing low order models gauged the accuracy of force predictions. Conclusions from this chapter are summarized below.

1. *The LEV drives airfoil performance in wake-airfoil interactions.* This flow structure provides a strong source of vortex lift and this effect grows with increasing angle of attack α. As a result, lift is enhanced while airfoil stall is delayed. In addition, this LEV produces enough flow reversal on the surface of the airfoil to create negative skin friction and this is the source of negative drag for low angles of attack ($\alpha < 8°$). Without the formation of the LEV, modifications for airfoil performance would be minimal.

2. *Turbulence scales on the order of the airfoil chord dominate.* Flow scales

larger than the airfoil do not play a dominant role in the unsteady airfoil behavior as they mostly contribute to the average flow. In contrast, flow scales similar in size to the airfoil chord are dominant and characterize the LEV structure. Since the LEV is responsible for modifying the airfoil performance, these turbulence scales play a critical role in modifying airfoil force production.

3. *Existing force prediction methods are inaccurate.* A comparison of three unsteady aerodynamic models show the cylinder-airfoil flow environment is not easily modeled. The cylinder wake creates transverse large perturbations that contradicts the assumption of small flow disturbance employed by every model. In addition, existing models fail to capture key flow features of the wake-airfoil interaction as flow separation and the formation of the LEV are not taken into account. These discrepancies amount to inaccurate force predictions.

Chapter 7: Conclusions

This thesis represents a combination of two-dimensional wind tunnel tests and CFD simulations to investigate the effect of wake-airfoil interactions on airfoil performance. The ultimate goal is to understand how airfoil force production evolves in a turbulent periodic flow created in the wake of a cylinder, and identify key flow structures responsible for altering airfoil performance. Varying four geometric parameters of the cylinder-airfoil configuration advances the fundamental knowledge of a wing operating in wake turbulence. The four cylinder-airfoil parameters examined in this work include the gap (G/D) and offset (z/D) distances between the cylinder and airfoil, the cylinder diameter normalized by the airfoil chord (D/c), and the cylinder cross-sectional geometry. The following section provides a summary of the research presented in previous chapters, along with key observations and conclusions regarding the interaction of a static NACA 0012 airfoil with the wake created by an upstream cylinder.

7.1 Summary of Research and Conclusions

The first part of this thesis described the flow characterization of a NACA 0012 airfoil mounted downstream of a cylinder for different gap distances ($G/D =$

$\{2, 3, 9.6\}$) and two angles of attack ($\alpha = 0°$ and $20°$). Wake flow characteristics were obtained using time-averaged particle image velocimetry (PIV) along with constant temperature anemometer (CTA) measurements. From these data, four wake properties were identified in the region between the cylinder and airfoil: (1) low momentum fluid, (2) high turbulence intensities, (3) wide range of turbulence scales, and (4) flow oscillations at the cylinder vortex shedding frequency. The first characteristic revealed the cylinder wake decreases the streamwise velocity upstream of the airfoil up to 56 % of the freestream value at $G/D = 3$. The second characteristic increases both streamwise and transverse velocity fluctuations, upstream and over the airfoil, to more than 55 % of the freestream value as a result of cylinder-airfoil interactions. The remaining two flow characteristics were a consequence of the cylinder wake producing a wide range of turbulence length scales, varying from 1 to 1×10^{-4} of an airfoil chord, while the flow upstream of the airfoil fluctuated at the cylinder vortex shedding frequency. Results from this flow characterization revealed that the inflow to the airfoil is highly unsteady while interacting with a spectrum of flow structure sizes, and effectively operates at a lower freestream velocity. Since the inflow to the airfoil dictates force production, these cylinder-airfoil wake characteristics lead to significant modifications in airfoil performance compared to an isolated NACA 0012.

The second part of this thesis quantified the modifications in airfoil force production and unsteady behavior via a parametric study. Cylinder-airfoil parameters were varied to form an extensive parameter space as the gap and offset distances varied from $G/D = \{2, 3, 5, 7, 10, 15\}$ and $z/D = \{0, \pm 0.25, \pm 0.5, \pm 0.75\}$, respectively.

Different cylinder geometry were also tested by increasing the cylinder-diameter-to-airfoil-chord ratio $D/c = \{0.36, 0.69, 1.04\}$ and changing the cross-sectional geometry from circular to square. Time-averaged lift, drag, and pitching moment coefficients were measured with a custom force balance while the amplitude and frequency of fluctuating airloads evaluated the airfoil unsteadiness.

Results from force measurements showed that every tested parameter influenced airfoil performance, but the strongest changes were associated with the relative positioning of the airfoil with respect to the cylinder wake: G/D and z/D. Close proximity to the cylinder wake at $G/D = 3$ led to significant lift augmentation as the maximum lift coefficient increased from $C_l = 0.81$ to 1.74, drag reduction caused C_d to become negative at low angles of attack ($\alpha < 8°$), and the airfoil stall was delayed to $\alpha = 33°$ compared to $\alpha = 9°$ for an isolated NACA 0012. Increasing the gap distance demonstrated that these altered performances diminish due to a weakening of the interactions between the cylinder wake and airfoil while performance asymptotes to the isolated airfoil case. Modifications in lift, drag, and stall angle also depended on the offset distance when the angle of attack was large ($\alpha > 10°$). Negative offset distances ($z/D < 0$) produced an increase in airfoil performance, while positive z/D resulted in the opposite effect. Smoke flow visualization revealed that for negative offset distances, the airfoil was located at the edge of the cylinder wake, whereas at $z/D = 0.25$ the airfoil was fully immersed in the wake. This caused different flow interactions with the cylinder wake and airfoil, resulting in different force production.

Similar to the airfoil performance results, all cylinder-airfoil parameters af-

fected the unsteady airfoil behavior. The frequency response was found to approach and match the cylinder vortex shedding frequency at low to moderate angles of attack ($\alpha \leq 20°$). This proved that the interactions between the wake and airfoil correspond to the cylinder aerodynamically exciting the airfoil and dictating the fluctuations of these airloads. This forcing was improved as the gap distance G/D and cylinder diameter D increased. Likewise, the amplitude of the unsteady airfoil response was predominantly correlated with the same parameters. A larger gap distance promoted the wake to weaken and decreased the amplitude of fluctuations, whereas increasing the cylinder diameter produced bigger vortices in the wake and resulted in a substantial gain in the airfoil's amplitude of fluctuating forces.

The final part of this thesis provided a fundamental understanding of the underlying flow physics of wake airfoil interactions by identifying key flow structures and correlating them with the modified airfoil force production. Phase-averaged flowfields were obtained from PIV measurements for a gap distance of $G/D = 3$ with a cylinder diameter of $D/c = 1.04$ while the airfoil's angle of attack varied from $\alpha = \{0°, 10°, 20°\}$. As the cylinder wake produced periodic transverse velocity fluctuations, corresponding to 66 % of the freestream value, this created a large effective angle of attack for the airfoil and resulted in the formation of a leading edge vortex (LEV). The implications of this LEV on airfoil force production are twofold. First, due to the periodic nature of the cylinder wake, LEVs formed on the upper and lower surfaces of the airfoil at zero angle of attack, resulting in zero net lift. As the angle of attack increased, the LEV only formed on the suction side of the airfoil creating flow asymmetry which contributed to a net lift at non-zero angles

of attack and generated lift augmentation while also delaying stall. Second, CFD results showed that as the LEV formed and advected over the airfoil, it induced flow reversal along the surface and resulted in a negative skin friction coefficient. Since skin friction drag dominates for a streamlined body at low angles of attack, such as the NACA 0012 airfoil, the negative skin friction significantly reduces the overall airfoil drag as this becomes the source for $C_d < 0$ when $\alpha < 8°$. These results demonstrated that the LEV plays a critical role in the airfoil force production during cylinder-airfoil interactions and elucidates the flow physics of modified airfoil performance as the NACA 0012 encounters a periodic turbulent wake.

In addition, a flow decomposition analysis was also performed to determine the influence of different turbulence length scales that exist in the cylinder's wake. Using frequency domain filters, the flowfield around the airfoil was separated into three different size categories including scales larger than the airfoil's chord c, scales ranging from 11 % to 95 % of the chord, and scales smaller than 10 % of c. The decomposition identified scales similar to the airfoil chord that contribute the most to modifying the unsteady airfoil behavior. Scales larger than the airfoil are thought of as quasi-steady, while the scales smaller than the airfoil act as aerodynamic turbulence and are minor compared to the influence of the LEV.

The key conclusions presented in this thesis clearly demonstrate that the NACA 0012 is subjected to an unsteady, turbulent inflow which significantly alters its aerodynamic performance compared to an isolated airfoil. A leading edge vortex is identified as the resulting flow structure from the interaction of an airfoil downstream of a cylinder's wake, and this vortex is responsible for lift augmentation

and negative drag while also providing an unsteady aerodynamic behavior.

7.2 Original Contributions

The current thesis makes several important original contributions to the fundamental understanding of how airfoil performance alters during a wake encounter and will help inform future studies concerning wake-airfoil interactions.

1. A comprehensive investigation of the time-averaged and unsteady aerodynamic behavior of airfoil performance downstream of a cylinder's turbulent wake was performed for four cylinder-airfoil parameters using force and flowfield measurements. These parameters included the cylinder-airfoil gap and offset distances, the cylinder diameter, and the cylinder cross-sectional geometry.

2. The fundamental understanding of the flow physics in the cylinder-airfoil interaction was advanced by identifying the leading edge vortex as the key flow structure responsible for altering airfoil performance. This leading edge vortex augmented lift and delayed stall by providing vortex lift at large angles of attack. At the same time, this vortex structure induced flow reversal along the airfoil's surface, producing negative drag during the cylinder-airfoil interaction.

3. A collection of extensive experimental results formed a database for the cylinder-airfoil configuration including time-averaged lift, drag, and pitching moment coefficients for a NACA 0012. This database is suitable for future studies needing to validate low order models or CFD simulations.

7.3 Suggestions for Future Work

The present work described the modifications in airfoil performance of a NACA 0012 downstream of a cylinder and also provided a fundamental understanding of flow physics during wake-airfoil impingement. While four parameters were tested for the current cylinder-airfoil configuration, many different permutations exist to inspire future investigations of wake-airfoil interactions. The remainder of this section offers suggestions to expand the current work and continue to unravel the complex flow physics associated with more sophisticated cylinder-airfoil configurations.

1. The experimental and numerical flowfield measurements described in chapter 6 were limited to a single cylinder-airfoil configuration with a gap distance of $G/D = 3$, zero offset distance $z/D = 0$, a cylinder-diameter-to-airfoil-chord ratio of $D/c = 1.04$, and circular cross-sectional geometry for the cylinder. Including variations in both the gap and offset distances would allow for the characterization of the LEV as the airfoil experiences different inflow conditions. At a larger gap distance, the transverse velocity fluctuations are expected to decrease as the cylinder wake weakens, reducing the effective angle of attack. This should affect the formation and growth of the LEV, yet results in chapter 5 show lift augmentation and drag reduction remain non-negligible at a gap distance of $G/D = 10$. An extended vortex characterization would also quantify the effect on the LEV's strength as the airfoil is fully immersed in the cylinder wake at $z/D = 0.25$ compared to interacting with the edge of

the wake at $z/D = -0.75$.

2. A better correlation of wake flow structures with airfoil force production can be achieved by simultaneously measuring time-resolved forces and PIV flowfields. Using an instrumented wing, surface pressure measurements synchronized with PIV would allow for a direct relationship between flow structures (e.g. LEV) and lift enhancement or negative drag. This would expand the understanding of the flow physics presented in this work.

3. Drag around an airfoil is obtained from a pressure distribution and skin friction, although the pressure term was not included in the results provided by the numerical study. The interaction between the cylinder and airfoil led to a reduction in the airfoil's drag coefficient while a negative skin friction drag was measured, suggesting reversed flow along the airfoil's surface is the cause. To confirm that flow reversal is the dominant source of drag reduction in the cylinder-airfoil configuration, the contribution of both pressure and skin friction drag should be quantified.

4. Introduce an array of cylinders with different diameters to create a multiscale turbulence wake upstream of the airfoil. In the current work, the turbulent inflow to the airfoil was characterized by one frequency and this dictated the airfoil's frequency response. Subjecting the airfoil to a wake with multiple characteristic frequencies would inform how the airfoil frequency response changes in complex wake-airfoil interactions.

5. In many engineering applications involving wake-airfoil interactions, the airfoil does not remain static. Investigating a dynamic cylinder-airfoil configuration would reveal different airfoil force production trends, causing the cylinder wake to modify and create a new inflow for the downstream airfoil. A recent study by Jarman et al. [96] has already numerically investigated the cylinder-airfoil configuration for a dynamically decreasing gap distance. Results indicate that the airfoil's frequency response increases up to 73 % of the cylinder vortex shedding frequency [96]. Including changes to offset distance and adding unsteady airfoil kinematics would extend the fundamental understanding of wake-airfoil interactions to existing engineering applications.

Appendix A: Sensitivity Study of Cutoff Wavenumbers for Flow Decomposition

To determine the appropriate cutoff wavenumbers for the flow decomposition, a sensitivity study was performed. Figure A.1 shows the resulting vorticity field after applying low-pass (left column), band-pass (middle column), and high-pass (right column) filters for different cutoff wavenumbers.

In the first row, the leading edge vortex (LEV) appears as a smooth structure in both the low-pass (figure A.1(a)) and band-pass cases (figure A.1(b)). The core of the vortex is well identified from both filters, with differences occurring mostly in the farfield. The high-pass result (figure A.1(c)) is very similar to the original flowfield in figure 6.10(a). These cutoff wavenumbers do not provide a good separation of scales since the LEV is similarly detected from the low and band-pass filters.

For the second set of cutoff wavenumbers (figures A.1(d), A.1(e), A.1(f)), each filtered vorticity field has different scales. The low-pass filter (figure A.1(d)) no longer shows a distinct LEV core, while the band and high-pass (figures A.1(e) and A.1(f)) results highlight different scales associated with the LEV. The high-pass field retains similar flow scales from the high-pass filter with a larger cutoff wavenumber.

Decreasing and increasing the lower and higher cutoff wavenumbers, respec-

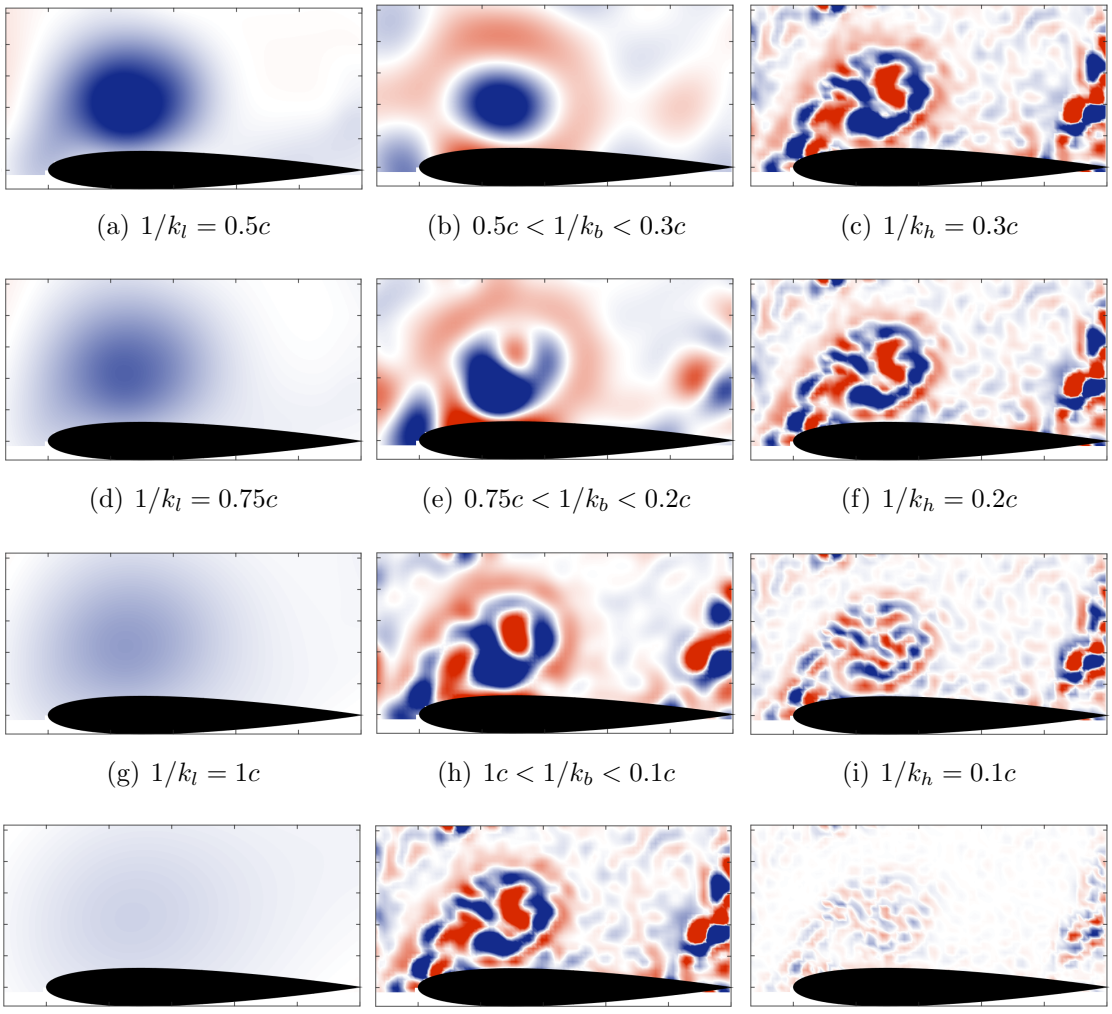

(a) $1/k_l = 0.5c$ (b) $0.5c < 1/k_b < 0.3c$ (c) $1/k_h = 0.3c$

(d) $1/k_l = 0.75c$ (e) $0.75c < 1/k_b < 0.2c$ (f) $1/k_h = 0.2c$

(g) $1/k_l = 1c$ (h) $1c < 1/k_b < 0.1c$ (i) $1/k_h = 0.1c$

(j) $1/k_l = 1.5c$ (k) $1.5c < 1/k_b < 0.05c$ (l) $1/k_h = 0.05c$

Figure A.1: Resulting vorticity fields from low-pass (left column), band-pass (middle column), and high-pass (right column) filtering for various cutoff wavenumbers.

tively, gives the desired separation of flow scales. The low-pass field (figure A.1(g)) provides the large scale contribution of the LEV, which mostly affects the background. The band-pass (figure A.1(h)) clearly captures the main features of the LEV, while the high-pass field (figure A.1(i)) shows the small turbulence scales hidden in the LEV structure.

The final set of cutoff wavenumbers does not provide any meaningful separation

of flow scales, since the low and high cutoff wavenumbers fail to retain sufficient flow scales (figures A.1(j) and A.1(l)). The band-pass filter captures most of the flow features (figure A.1(k)).

The appropriate selection of the cutoff wavenumbers is subjective and will vary for each analysis. Cutoff wavenumbers from the third row (figures A.1(g), A.1(h), A.1(i)) provide a clear separation of large, medium, and small scales. Large scales are considered bigger than the airfoil chord and small scales are defined as less than 10 % of the airfoil chord. This separates the flow into the background flow scales, scales close to the airfoil chord such as the LEV core diameter, and small-scale turbulence present in the cylinder-airfoil interaction.

Bibliography

[1] Albert E. von Doenhoff and Frank T. Abbott. The Langley two-dimensional low-turbulence pressure tunnel. Technical Report 1283, NACA, Washington D.C., 1947.

[2] Ira H. Abbott and Albert E. von Doenhoff. *Theory of wing sections including a summary of airfoil data*. Dover, 1959.

[3] Jon A Hoffmann. Effects of freestream turbulence on the performance characteristics of an airfoil. *AIAA Journal*, 29(9):1353–1354, 1991.

[4] David Galway, J Etele, and Giovanni Fusina. Development and implementation of an urban wind field database for aircraft flight simulation. *Journal of Wind Engineering and Industrial Aerodynamics*, 103(4):73–85, 2012.

[5] Vladimir V Golubev and Miguel R Visbal. Modeling MAV response in gusty urban environment. *International Journal of Micro Air Vehicles*, 4(1):79–92, 2012.

[6] Daniel F Scharpf and Thomas J. Mueller. Experimental study of a low Reynolds number tandem airfoil configuration. *Journal of Aircraft*, 29(2):231–236, 1992.

[7] Thierry M Faure, Laurent Hétru, and Olivier Montagnier. Aerodynamic features of a two-airfoil arrangement. *Experiments in Fluids*, 58(10):146, 2017.

[8] William B Blake and David R Gingras. Comparison of predicted and measured formation flight interference effects. *Journal of Aircraft*, 41(2):201–207, 2004.

[9] S Andrew Ning, Tristan C Flanzer, and Ilan M Kroo. Aerodynamic performance of extended formation flight. *Journal of Aircraft*, 48(3):855–865, 2011.

[10] S Shukla, S S Sinha, and S N Singh. Ship-helo coupled airwake aerodynamics: A comprehensive review. *Progress in Aerospace Sciences*, 106:71–107, 2019.

[11] Mostafa Rahimpour and Peter Oshkai. Experimental investigation of airflow over the helicopter platform of a polar icebreaker. *Ocean Engineering*, 121:98–111, 2016.

[12] James S Forrest and Ieuan Owen. An investigation of ship airwakes using Detached-Eddy Simulation. *Computers and Fluids*, 39(4):656–673, 2010.

[13] Gregory M. Dooley, Pablo M. Carrica, J. Ezequiel Martin, Austin F. Krebill, and James H.J. Buchholz. Effects of waves, motions and atmospheric turbulence on ship airwakes. In *AIAA Scitech 2019 Forum*, San Diego, California, 2019.

[14] Esteban Ferrer and Richard H.J. Willden. Blade-wake interactions in cross-flow turbines. *International Journal of Marine Energy*, 11(9):71–83, 2015.

[15] Chee Tung, Yung H. Yu, and Scott L. Low. Aerodynamic aspects of blade-vortex interaction (BVI). In *Fluid Dynamics Conference 27th*, New Orleans, 1996.

[16] J. S. Marshall and J. R. Grant. Penetration of a blade into a vortex core: Vorticity response and unsteady blade forces. *Journal of Fluid Mechanics*, 306:83–109, 1996.

[17] Fernando Porté-Agel, Majid Bastankhah, and Sina Shamsoddin. Wind-Turbine and wind-farm flows: A review. *Boundary-Layer Meteorology*, 174(1):1–59, 2020.

[18] A. Crespo, J. Hernández, and S. Frandsen. Survey of modelling methods for wind turbine wakes and wind farms. *Wind Energy*, 2(1):1–24, 1999.

[19] R. J. Barthelmie, K. Hansen, S. T. Frandsen, O. Rathmann, J. G. Schepers, W. Schlez, J. Phillips, K. Rados, A. Zervos, E. S. Politis, and P. K. Chaviaropoulos. Modelling and measuring flow and wind turbine wakes in large wind farms offshore. *Wind Energy*, 12(5):431–444, 2009.

[20] Pakpong Chirarattananon, Yufeng Chen, E. Farrell Helbling, Kevin Y. Ma, Richard Cheng, and Robert J. Wood. Dynamics and flight control of a flapping-wing robotic insect in the presence of wind gusts. *Interface Focus*, 7(1):1–14, 2017.

[21] Tri D Ngo and Cornel Sultan. Model predictive control for helicopter shipboard operations in the ship airwakes. *Journal of Guidance, Control, and Dynamics*, 39(3):574–589, 2016.

[22] D Casalino, F Diozzi, R Sannino, and A Paonessa. Aircraft noise reduction technologies: A bibliographic review. *Aerospace Science and Technology*, 12(1):1–17, 2008.

[23] Nigel Peake and Anthony B Parry. Modern challenges facing turbomachinery aeroacoustics. *Annual Review of Fluid Mechanics*, 44:227–248, 2011.

[24] H. G. Küssner. Zusammenfassender Bericht über den Instationären Auftrieb von Flügeln. *Luftfahrtforschung*, 13(12):410–424, 1935.

[25] T. von Karman and W. R. Sears. Airfoil theory for non-uniform motion. *Journal of the Aeronautical Sciences*, 5(10):379–390, 1938.

[26] William R. Sears. Some aspects of non-stationary airfoil theory and its practical application. *Journal of the Aeronautical Sciences*, 8(3):104–108, 1941.

[27] M. E. Goldstein and H. Atassi. A complete second-order theory for the unsteady flow about an airfoil due to a periodic gust. *Journal of Fluid Mechanics*, 74(4):741–765, 1976.

[28] H. M. Atassi. The Sears problem for a lifting airfoil revisited - new results. *Journal of Fluid Mechanics*, 141(4):109–122, 1984.

[29] J. Val Healey. Simulating the helicopter-ship interface as an alternative to current methods of determining the safe operating envelopes. Technical Report NPS 67-86-003, Naval Postgraduate School, Monterey, California, 1986.

[30] Fangfang Wang, Ang Gao, Shiqiang Wu, Senlin Zhu, Jiangyu Dai, and Qian Liao. Experimental investigation of coherent vortex structures in a backward-facing step flow. *Water*, 11(12), 2019.

[31] J F Derakhshandeh and Md Mahbub Alam. A review of bluff body wakes. *Ocean Engineering*, 182:475–488, 2019.

[32] C. H.K. Williamson. Vortex dynamics in the cylinder wake. *Annual Review of Fluid Mechanics*, 28:477–539, 1996.

[33] H. J. Niemann and N. Hölscher. A review of recent experiments on the flow past circular cylinders. *Journal of Wind Engineering and Industrial Aerodynamics*, 33(1-2):197–209, 1990.

[34] Anatol Roshko. On the development of turbulent wakes from vortex streets. Technical Report 2913, NACA, Washington D.C., 1953.

[35] E. Achenbach and E. Heinecke. On vortex shedding from smooth and rough cylinders in the range of Reynolds numbers 6x10ˆ3 to 5x10ˆ6. *Journal of Fluid Mechanics*, 109(12):239–251, 1981.

[36] Uwe Fey, Michael König, and Helmut Eckelmann. A new Strouhal-Reynolds-number relationship for the circular cylinder in the range 47<Re<2x10ˆ5. *Physics of Fluids*, 10(7):1547–1549, 1998.

[37] Brian Cantwell and Donald Coles. An experimental study of entrainment and transport in the turbulent near wake of a circular cylinder. *Journal of Fluid Mechanics*, 136:321–374, 1983.

[38] J. C. Lin, J. Towfighi, and D. Rockwell. Instantaneous Structure of the Near Wake of a Circular Cylinder. *Journals of Fluids and Structures*, 9:409–418, 1995.

[39] C. Chyu and D. Rockwell. Evolution of patterns of streamwise vorticity in the turbulent near wake of a circular cylinder. *Journal of Fluid Mechanics*, 320:117–137, 1996.

[40] L. Ong and J. Wallace. The velocity field of the turbulent very near wake of a circular cylinder. *Experiments in Fluids*, 20(6):441–453, 1996.

[41] Sridhar Ravi, Simon Watkins, Jon Watmuff, Kevin Massey, Phred Petersen, and Matthew Marino. Influence of large-scale freestream turbulence on the performance of a thin airfoil. *AIAA Journal*, 50(11):2448–2459, 2012.

[42] K E Swalwell, J Sheridan, and W H Melbourne. The effect of turbulence intensity on stall of the NACA 0021 aerofoil. In *14th Australasian Fluid Mechanics Conference*, pages 941–944, Adelaide, Australia, 2001.

[43] P. E. Roach. The generation of nearly isotropic turbulence by means of grids. *International Journal of Heat and Fluid Flow*, 8(2):82–92, 1987.

[44] Nicholas J Kay, Peter J Richards, and Rajnish N Sharma. Influence of turbulence on cambered and symmetrical airfoils at low Reynolds numbers. *AIAA Journal*, 58(5):1913–1925, 2020.

[45] Ph Devinant, T Laverne, and J Hureau. Experimental study of wind-turbine airfoil aerodynamics in high turbulence. *Journal of Wind Engineering and Industrial Aerodynamics*, 90(6):689–707, 2002.

[46] X. Amandolèse and E. Széchényi. Experimental study of the effect of turbulence on a section model blade oscillating in stall. *Wind Energy*, 7(4):267–282, 2004.

[47] Donald Rockwell. Vortex-body interactions. *Annual Review of Fluid Mechanics*, 30(1):199–229, 1998.

[48] D J Lee and C. A. Smith. Effect of vortex core distortion on blade-vortex interaction. *AIAA Journal*, 29(9):1355–1362, 1991.

[49] Di Peng and James W Gregory. Asymmetric distributions in pressure/load fluctuation levels during blade-vortex interactions. *Journal of Fluids and Structures*, 68:58–71, 2017.

[50] M. C. Wilder and D P Telionis. Parallel blade-vortex interaction. *Journal of Fluids and Structures*, 12(7):801–838, 1998.

[51] Caleb J Barnes and Miguel R Visbal. Clockwise vortical-gust/airfoil interactions at a transitional reynolds number. *AIAA Journal*, 56(10):3863–3874, 2018.

[52] M. B. Horner, E Saliveros, A Kokkalis, and R A.Mc D. Galbraith. Results from a set of low speed blade-vortex interaction experiments. *Experiments in Fluids:*, 14(5):341–352, 1993.

[53] J. Swirydczuk, M. C. Wilder, and D. P. Telionis. The interaction of coherent vortices with short flat plates. *Journal of Fluids Engineering*, 115(4):590–596, 1993.

[54] Caleb J Barnes and Miguel R Visbal. Counterclockwise vortical-gust/airfoil interactions at a transitional reynolds number. *AIAA Journal*, 56(7):2540–2552, 2018.

[55] Samir Ziada and Donald Rockwell. Vortex-leading-edge interaction. *Journal of Fluid Mechanics*, 118(5):79–107, 1982.

[56] Ismet Gursul and Donald Rockwell. Vortex street impinging upon an elliptical leading edge. *Journal of Fluid Mechanics*, 211(211):211–242, 1990.

[57] Ruhi Kaykayoglu and Donald Rockwell. Vortices incident upon a leading edge: Instantaneous pressure fields. *Journal of Fluid Mechanics*, 156:439–461, 1985.

[58] M. M. Zdravkovich. Review of flow interference between two circular cylinders in various arrangements. *Journal of Fluids Engineering, Transactions of the ASME*, 99(4):618–633, 1977.

[59] M. M. Zdravkovich. The effects of interference between circular cylinders in cross flow. *Journal of Fluids and Structures*, 1(2):239–261, 1987.

[60] C. H.K. Williamson. Evolution of a single wake behind a pair of bluff bodies. *Journal of Fluid Mechanics*, 159(10):1–18, 1985.

[61] A. Okajima. Aerodynamic characteristics of stationary tandem cylinders at high Reynolds numbers. *Bulletin of the Research Institute of Applied Mechanics*, 46:111–127, 1977.

[62] Tamotsu Igarashi. Characteristics of the Flow around Two Circular Cylinders Arranged in Tandem : 1st Report. *Bulletin of JSME*, 24(188):323–331, 1981.

[63] Marc C Jacob, Jérôme Boudet, Damiano Casalino, and Marc Michard. A rod-airfoil experiment as a benchmark for broadband noise modeling. *Theoretical and Computational Fluid Dynamics*, 19(3):171–196, 2005.

[64] Jérôme Boudet, Nathalie Grosjean, and Marc C Jacob. Wake-Airfoil interaction as broadband noise source: A Large-Eddy Simulation study. *International Journal of Aeroacoustics*, 4(1-2):93–115, 2005.

[65] Mizue Munekata, Kaoru Kawahara, Takamasa Udo, Hiroyuki Yoshikawa, and Hideki Ohba. An experimental study on aerodynamic sound generated from wake interference of circular cylinder and airfoil vane in tandem. *Journal of Thermal Science*, 15(4):342–348, 2006.

[66] Mizue Munekata, Ryuta Koshiishi, Hiroyuki Yoshikawa, and Hideki Ohba. An experimental study on aerodynamic sound generated from wake interaction of circular cylinder and airfoil with attack angle in tandem. *Journal of Thermal Science*, 17(3):212–217, 2008.

[67] Yi Jiang, Mei Liang Mao, Xiao Gang Deng, and Hua Yong Liu. Numerical investigation on body-wake flow interaction over rod-airfoil configuration. *Journal of Fluid Mechanics*, 779(9):1–35, 2015.

[68] W. D. Michelsen and T. J. Mueller. Low reynolds number airfoil performance subjected to wake interference from an upstream airfoil. In *5th Applied Aerodynamics Conference*, pages 196–206, 1987.

[69] Jerry M Chen and Chih Chung Choa. Freestream disturbance effects on an airfoil pitching at constant rate. *Journal of Aircraft*, 36(3):507–514, 1999.

[70] Z. Zhang, Z. Wang, and I. Gursul. Lift enhancement of a stationary wing in a wake. *AIAA Journal*, 58(11):4613–4619, 2020.

[71] Vibhav Durgesh, Rodrigo Padilla, Elifalet Garcia, and Hamid Johari. Impact of coherent structures on aerodynamic performance at low Reynolds numbers. In *AIAA Scitech 2019 Forum*, San Diego, 2019.

[72] Q. Liao, G. J. Dong, and X. Y. Lu. Vortex formation and force characteristics of a foil in the wake of a circular cylinder. *Journal of Fluids and Structures*, 19(4):491–510, 2004.

[73] Theodore Theodorsen. General theory of aerodynamic instability and the mechanism of flutter. Technical Report 496, NACA, 1935.

[74] J. G. Leishman. *Principles of Helicopter Aerodynamics*. Cambridge University Press, second edition, 2006.

[75] Ulrike Cordes, G. Kampers, T. Meiner, C. Tropea, J. Peinke, and M. Hölling. Note on the limitations of the Theodorsen and Sears functions. *Journal of Fluid Mechanics*, 811:1–11, 2017.

[76] Yeon Sik Baik, Luis P. Bernal, Kenneth Granlund, and Michael V. Ol. Unsteady force generation and vortex dynamics of pitching and plunging aerofoils. *Journal of Fluid Mechanics*, 709:37–68, 2012.

[77] Anna M Young and Amanda S M Smyth. Gust-Airfoil coupling with a loaded airfoil. *AIAA Journal*, 59(3):773–785, 2020.

[78] Nathaniel J. Wei, Johannes Kissing, Tom T.B. Wester, Sebastian Wegt, Klaus Schiffmann, Suad Jakirlic, Michael Hölling, Joachim Peinke, and Cameron Tropea. Insights into the periodic gust response of airfoils. *Journal of Fluid Mechanics*, 876:237–263, 2019.

[79] Jonathan N Lefebvre and Anya R Jones. Experimental investigation of airfoil performance in the wake of a circular cylinder. *AIAA Journal*, 57(7):2808–2818, 2019.

[80] William Sutherland. The viscosity of gases and molecular force. *Philosophical Magazine Series 5*, 36(223):507–531, 1893.

[81] Ian Farrance and Robert Frenkel. Uncertainty of measurement: A review of the rules for calculating uncertainty components through functional relationships. *The Clinical Biochemist Reviews*, 33(2):49–75, 2012.

[82] A. K.M.F. Hussain and W. C. Reynolds. The mechanics of an organized wave in turbulent shear flow. *Journal of Fluid Mechanics*, 41(2):241–258, 1970.

[83] Lawrence Sirovich. Turbulence and the dynamics of coherent structures part I: Coherent structures. *Quarterly of Applied Mathematics*, 45(3):561–571, 1987.

[84] Kunihiko Taira, Steven L. Brunton, Scott T.M. Dawson, Clarence W. Rowley, Tim Colonius, Beverley J. McKeon, Oliver T. Schmidt, Stanislav Gordeyev, Vassilios Theofilis, and Lawrence S. Ukeiley. Modal analysis of fluid flows: An overview. *AIAA Journal*, 55(12):4013–4041, 2017.

[85] B. W. Van Oudheusden, F. Scarano, N. P. Van Hinsberg, and D. W. Watt. Phase-resolved characterization of vortex shedding in the near wake of a square-section cylinder at incidence. *Experiments in Fluids*, 39(1):86–98, 2005.

[86] J. C.R. Hunt, A. A. Wray, and P. Moin. Eddies, streams, and convergence zones in turbulent flows. In *Center for Turbulence Research*, pages 193–208, 1988.

[87] M. S. Chong, A. E. Perry, and B. J. Cantwell. A general classification of three-dimensional flow fields. *Physics of Fluids A*, 2(5):765–777, 1990.

[88] Jinhee Jeong and Fazle Hussain. On the identification of a vortex. *Journal of Fluid Mechanics*, 285:69–94, 1995.

[89] Laurent Graftieaux, Marc Michard, and Nathalie Grosjean. Combining PIV, POD and vortex identification algorithms for the study of unsteady turbulent swirling flows. *Measurement Science and Technology*, 12:1422–1429, 2001.

[90] Brenden P Epps. Review of vortex identification methods. In *AIAA SciTech Forum*, Grapevine, Texas, 2017.

[91] Fabrizio De Gregorio and Antonio Visingardi. Vortex detection criteria assessment for PIV data in rotorcraft applications. *Experiments in Fluids*, 61(8):1–22, 2020.

[92] C. Truesdell. Two measures of vorticity. *Journal of Rational Mechanics and Analysis*, 2:173–217, 1953.

[93] Lisa Schielicke, Peter Névir, and Uwe Ulbrich. Kinematic vorticity number - A tool for estimating vortex sizes and circulations. *Tellus, Series A: Dynamic Meteorology and Oceanography*, 68:1–20, 2016.

[94] Finn E. Jorgensen. *How to measure turbulence with hot-wire anemometers - a practical guide.* Dantec Dynamics, Skovlunde, Denmark, 2002.

[95] S. Yavuzkurt. A guide to uncertainty analysis of hot-wire data. *Journal of Fluids Engineering, Transactions of the ASME*, 106(2):181–186, 1984.

[96] Lucas M Jarman, Marilyn J Smith, Jonathan N Lefebvre, and Anya R Jones. Dynamics of an airfoil moving through the wake of a circular cylinder. In *AIAA Scitech 2019 Forum*, 2019.

[97] Yu Zhou and Md Mahbub Alam. Wake of two interacting circular cylinders: A review. *International Journal of Heat and Fluid Flow*, 62(12):510–537, 2016.

[98] Hendrik Tennekes and John L Lumley. *A First Course in Turbulence.* MIT Press, 1972.

[99] Stephen B Pope. *Turbulent Flows.* Cambridge University Press, 1st edition, 2000.

[100] P. L. O'Neill, D Nicolaides, D. R. Honnery, and J. Soria. Autocorrelation functions and the determination of integral length with reference to experimental and numerical data. In *15th Australasian Fluid Mechanics Conference*, volume 1, pages 1–4, 2004.

[101] Guichao Wang, Fan Yang, Ke Wu, Yongfeng Ma, Cheng Peng, Tianshu Liu, and Lian Ping Wang. Estimation of the dissipation rate of turbulent kinetic energy: A review. *Chemical Engineering Science*, 229(1):1–17, 2021.

[102] M. Piper and Julie K. Lundquist. Surface layer turbulence measurements during a frontal passage. *Journal of the Atmospheric Sciences*, 61(14):1768–1780, 2004.

[103] Emmanuel O. Akinlabi, Marta Wacławczyk, Juan Pedro Mellado, and Szymon P. Malinowski. Estimating turbulence kinetic energy dissipation rates in the numerically simulated stratocumulus cloud-top mixing layer: Evaluation

of different methods. *Journal of the Atmospheric Sciences*, 76(5):1471–1488, may 2019.

[104] A. N. Kolmogorov. Dissipation of energy in the locally isotropic turbulence. *Proceedings of the Royal Society of London. Series A: Mathematical and Physical Sciences*, 434(1890):15–17, 1991.

[105] A. N. Kolmogorov. The local structure of turbulence in incompressible viscous fluid for very large Reynolds numbers. *Proceedings of the Royal Society of London. Series A: Mathematical and Physical Sciences*, 434(1890):9–13, 1991.

[106] Domenico Ferraro, Sergio Servidio, Vincenzo Carbone, Subhasish Dey, and Roberto Gaudio. Turbulence laws in natural bed flows. *Journal of Fluid Mechanics*, 798(07):540–571, 2016.

[107] Andrew H Lind, Jonathan N Lefebvre, and Anya R Jones. Time-averaged aerodynamics of sharp and blunt trailing-edge static airfoils in reverse flow. *AIAA Journal*, 52(12):2751–2764, 2014.

[108] A Fage and F C Johansen. On the flow of air behind an inclined flat plate of infinite span. *Proceedings of the Royal Society of London. Series A*, 116(773):170–197, 1927.

[109] Rong F Huang and Chih L Lin. Vortex shedding and shear-layer instability of wing at low-Reynolds numbers. *AIAA Journal*, 33(8):1398–1403, 1995.

[110] Jerry M Chen and Yuan Cheng Fang. Strouhal numbers of inclined flat plates. *Journal of Wind Engineering and Industrial Aerodynamics*, 61(2-3):99–112, 1996.

[111] Andrew H Lind and Anya R Jones. Vortex shedding from airfoils in reverse flow. *AIAA Journal*, 53(9):2621–2633, 2015.

[112] Longjun Wang, M. Mahbub Alam, and Yu Zhou. Two tandem cylinders of different diameters in cross-flow: Effect of an upstream cylinder on wake dynamics. *Journal of Fluid Mechanics*, 836(2):5–42, 2018.

[113] Z Zhang, Z Wang, and I Gursul. Delay of stall for a stationary wing placed in a wake. In *AIAA Scitech 2021 Forum*, Virtual Event, 2021.

[114] Tamotsu Igarashi. Characteristics of the flow around a square prism. *Bulletin of the JSME*, 27(231):1858–1865, 1984.

[115] C Norberg. Flow around rectangular cylinders: Pressure forces and wake frequencies. *Journal of Wind Engineering and Industrial Aerodynamics*, 49(1-3):187–196, 1993.

[116] S Dutta, K Muralidhar, and P K Panigrahi. Influence of the orientation of a square cylinder on the wake properties. *Experiments in Fluids*, 34(1):16–23, 2003.

[117] R F Huang, B H Lin, and S C Yen. Time-averaged topological flow patterns and their influence on vortex shedding of a square cylinder in crossflow at incidence. *Journal of Fluids and Structures*, 26(3):406–429, 2010.

[118] Jeff D. Eldredge and Anya R. Jones. Leading-edge vortices: Mechanics and modeling. *Annual Review of Fluid Mechanics*, 51:75–104, 2019.

[119] Miguel R Visbal. Dynamic stall of a constant-rate pitching airfoil. *Journal of Aircraft*, 27(5):400–407, 1990.

[120] B. J. Pruski and R. D.W. Bowersox. Leading-edge flow structure of a dynamically pitching NACA 0012 airfoil. *AIAA Journal*, 51(5):1042–1053, 2013.

[121] C W Pitt Ford and H Babinsky. Lift and the leading-edge vortex. *Journal of Fluid Mechanics*, 720:280–313, 2013.

[122] Field Manar, Peter Mancini, David Mayo, and Anya R Jones. Comparison of rotating and translating wings: Force production and vortex characteristics. *AIAA Journal*, 54(2):519–530, 2016.

[123] R. Gopalkrishnan, M. S Triantafyllou, G S Triantafyllou, and D. Barrett. Active vorticity control in a shear flow using a flapping foil. *Journal of Fluid Mechanics*, 274:1–21, 1994.

[124] Knut Streitlien, George S Triantafyllou, and Michael S Triantafyllou. Efficient foil propulsion through vortex control. *AIAA Journal*, 34(11):2315–2319, 1996.

[125] James C. Liao, David N. Beal, George V. Lauder, and Michael S. Triantafyllou. The Kármán gait: Novel body kinematics of rainbow trout swimming in a vortex street. *Journal of Experimental Biology*, 206(6):1059–1073, 2003.

[126] Manoochehr M Koochesfahani. Vortical patterns in the wake of an oscillating airfoil. *AIAA Journal*, 27(9):1200–1205, 1989.

[127] M. S. Triantafyllou, G. S. Triantafyllou, and R. Gopalkrishnan. Wake mechanics for thrust generation in oscillating foils. *Physics of Fluids A*, 3(12):2835–2837, 1991.

[128] Jo Roberts and Thomas D Roberts. Use of the Butterworth low-pass filter for oceangraphic data. *Journal of Geophysical Research*, 83:5510–5514, 1978.

[129] Ayush Dogra and Parvinder Bhalla. Image sharpening by Gaussian and Butterworth high pass filter. *Biomedical and Pharmacology Journal*, 7(2):707–713, 2014.